EXPERIMENTAL AND THEORETICAL BIOMECHANICAL ANALYSES OF THE SECOND STAGE OF LABOR

by

Dejun Jing

A dissertation submitted in partial fulfillment
of the requirements for the degree of
Doctor of Philosophy
(Mechanical Engineering)
in The University of Michigan
2010

Doctoral Committee:

Professor James A. Ashton-Miller, Co-Chair
Professor John O.L. DeLancey, Co-Chair
Professor Alan Wineman
Professor Gregory M. Hulbert

To my family

ACKNOWLEDGEMENTS

I would like to express my earnest gratitude to both of my advisors, Professor James A. Ashton-Miller and Professor John O. L. DeLancey. Their guidance, assistance, patience, and encouragement have been of enormous importance to my research and the completion of the dissertation. I would also like to thank my other committee members, Professor Alan S. Wineman and Professor Gregory M. Hulbert, for their helpful advices and comments.

I am indebted to the Biomechanics Research Lab. It has been a great pleasure pursuing my PhD in this lab. I sincerely appreciate my research colleagues, Kelly, Jinyong, Jiajia, Youkon, Luyun, and Kuocheng, for their help, discussion, and all the good times we have had in the office. I especially thank Janet Kemp, the retired senior technician in BRL, for her helps in our daily lab activities. I also want to thank the doctors, fellows and staffs of the Pelvic Floor Research Group. Their invaluable knowledge, opinions and suggestions guided me, a mechanical engineering student, into the world of obstetrics and gynaecology.

I want to express my deepest thanks to my parents and sister for all the love and support they have given me. Finally, I would like to dedicate this thesis to my wife, Dongmei, and my little boy, Zongzong, who are my motivations for completing this PhD study and pursuing future career.

TABLE OF CONTENTS

LIST OF FIGURES

Figure

LIST OF TABLES

Table

LIST OF APPENDICES

Appendix

CHAPTER I

Introduction

1.1 Background

1.1.1 The stages of human labor before baby birth

Based on whether the woman has begun volitional pushing, the labor process before the birth of baby is often divided into two stages.

The first stage of labor

This stage begins with the onset of uterine contractions that cause progressive dilation of the cervix, and ends when the cervix is fully dilated and the baby is ready to be pushed out. This stage, lasting from 10 to 20 hours varying with different women, can be further divided into three periods: *early labor*, *active labor*, and *transition*.

During early labor, the cervix gradually effaces (thins out) and dilates (opens) up to $3 \sim 4$ cm. The uterine contractions, starting with about 10 minutes apart and lasting about 30 seconds, gradually become longer, stronger, and closer, and eventually become 5 minutes apart lasting 40 to 60 seconds.

The active labor is characterized by accelerated uterine contractions, reaching $3 \sim 5$ minutes apart and lasting about 60 seconds. The cervix also dilates more rapidly and reaches up to $4 \sim 8$ cm.

Transition is the last and most intensive part of the first stage of labor, in which the cervix dilates from 8 to a full 10 cm. The uterine contractions are usually very strong and frequent, coming every 3 minutes and lasting 1 minute. By the time the cervix is fully dilated and transition is over, the baby has usually descended somewhat into the pelvis.

The second stage of labor

This stage is also referred to as the 'pushing' stage, which begins when the cervix is fully dilated and ends with the birth of the baby. The average length of this stage for a nulliparous woman ranges from $1 \sim 2$ hours and shorter for subsequent births. During this period, the uterine contractions become relatively regular, coming approximately every $3 \sim 5$ minutes and lasting around $60 \sim 90$ seconds. To facilitate delivery, the obstetrical professionals guide the women to 'bear down' (or 'push'), i.e., volitionally contract her diaphragm and abdominal wall muscles during each uterine contraction. This combined effort exerts pressure on the fetus to gradually move down through the birth canal. This thesis study investigated the biomechanics of the second stage of labor, and the first stage of labor is not in the study objectives.

1.1.2 Anatomy of the female pelvic floor

All the muscles, the connective tissues, and the organs that fill the opening at the bottom of bony pelvis are collectively called the pelvic floor. The pelvic floor muscles, comprised of the levator ani, form a 'U-shaped' curved diaphragm surrounding the levator hiatus, and span rear two-thirds of the pelvic cavity. They serve to maintain closure of the urogenital hiatus and provide support for the urethra and pelvic organs (for example, *Lawson* 1974, *DeLancey* 1986, 1988, 1989, 1994, *Strohbehn et al.* 1996, *Ashton-Miller et al.* 2001). The levator ani muscle consists of pubovisceral complex (pubovaginal-puboperineal-puboanalis portions), puborectalis and iliococcygeus

(*Margulies et al.*, 2006) (Figure 1.1 and Figure 1.2).

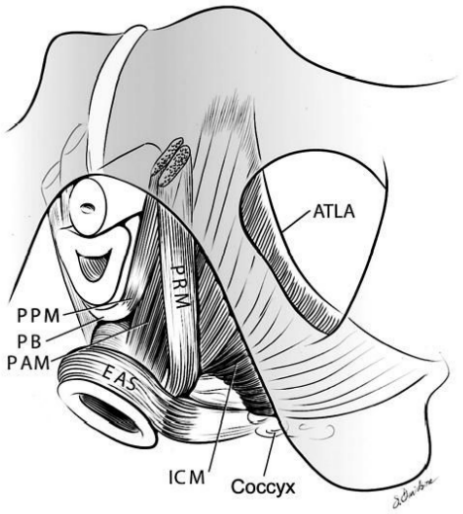

Figure 1.1: Schematic view of the levator ani muscles from below, after the vulvar structures and perineal membrane have been removed, that shows the arcus tendineus levator ani (ATLA); the external anal sphincter (EAS); the puboanal muscle (PAM); the perineal body (PB) uniting the two ends of the puboperineal muscle (PPM); the iliococcygeal muscle (ICM); and the puborectal muscle (PRM). Note that the urethra and vagina have been transected just above the hymenal ring. Copyright © DeLancey 2003.

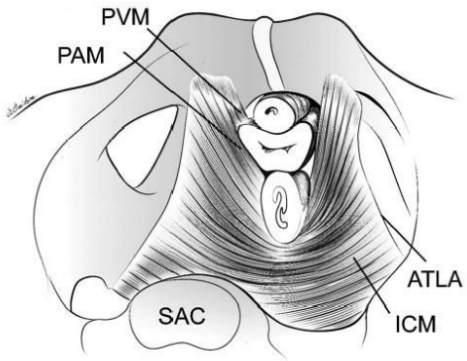

Figure 1.2: Schematic view of the levator ani muscles from above, looking over the sacral promontory (SAC), showing the pubovaginal muscle (PVM), sometimes called the pubococcygeal muscle. The urethra, the vagina, and the rectum have been transected just above the pelvic floor. PAM denotes the puboanal muscle. (The internal obturator muscles have been removed to clarify levator muscle origins.) Copyright © DeLancey 2003.

At the rear of the pelvic floor, the iliococcygeus forms a relatively flat, horizontal shelf spanning the potential gap from one pelvic sidewall to the other near the sacrum. The pubovisceral muscles originate from the pubic bone on either side of the symphysis and insert on to the walls of the pelvic organs and the perineal body. They are fatigue-resistant (type 1) muscles and help to close the urogenital hiatus, i.e., the opening in the levator ani through which the urethra and vagina pass. The puborectal muscle originates laterally to the pubovisceral muscles, forms a U-shaped sling around and behind the rectum, and inserts on to the external anal sphincter.

1.1.3 Female pelvic floor dysfunction

The common female pelvic floor dysfunctions, including urinary incontinence, fecal incontinence and pelvic organ prolapse, are believed to be highly associated with having given vaginal birth. For example, parity is the single most important risk factor for developing stress urinary incontinence (*Foldspang et al.*, 1992) and pelvic floor prolapse (*Mant et al.*, 1997). Recent imaging investigations have demonstrated that levator ani muscle damage can occur during vaginal birth (*Tunn et al.* 1999, *Hoyte et al.* 2001, *DeLancey et al.* 2003, *Dietz and Lanzarone* 2005, and *Ashton-Miller and Delancey* 2009), with sequelae including stress urinary incontinence (*Kearney et al.*, 2006) and pelvic organ prolapse (*Hoyte et al.*, 2004).

The need for treating pelvic floor dysfunction increases inexorably with advancing age (*Gainey* 1943, *Foldspang et al.* 1992, *Ryhammer et al.* 1995, *Mant et al.* 1997). With the burgeoning elderly population, this means more and more women are being affected by birth-induced injuries. Approximately 11% of American women eventually require surgery for pelvic floor dysfuncion (*Olsen et al.*, 1997), and this health problem adversely affects a woman's opportunities in employment, enjoyment and health-promoting exercises. Since some birth-induced injuries are not recoverable, the functional restoration of pelvic floor from later surgery or rehabilitation is

far from satisfactory (*Kahn and Stanton*, 1997). Therefore, the most natural and effective way to avoid or decrease pelvic floor dysfunction is to prevent the problem occuring during parturition. What, however, are the appropriate prevention strategies?

To answer this question, it is necessary to better understand the biomechanics of pelvic floor muscles during the second stage of labor. Being a physiologically intricate and structurally complex region, the pelvic floor is subjected to remarkable biomechanical changes during the second stage of labor. When the fetal head moves progressively through the pelvic canal, it inevitably induces substantial stretch in the pelvic floor muscles. One 3-D geometric model showed that the medial pubococcygeus muscles undergo a stretch ratio of 3.26 during vaginal birth (*Lien et al.*, 2004). It is not surprising, therefore, that such excessive stretch can damage the pelvic floor muscles. Each portion of levator ani muscle serves a specific mechanical function, so its injury will result in specific types of pelvic floor dysfunction. Therefore, understanding the biomechanics of pelvic floor muscles is one of the keys to unveiling the mechanisms underlying pelvic floor dysfunctions induced by vaginal birth.

1.2 Literature review of biomechanical studies of the pelvic floor and the second stage of labor

1.2.1 Experimental studies

One of the key aspects of understanding the biomechanics of pelvic floor is the mechanical properties of levator ani muscles, since, from the viewpoint of biomechanics, the mechanical properties determine how these muscles deform when contacting with and being stretched by the fetus. Specifically, the time-dependent nonlinear mechanical behavior of the muscles under finite deformation is of the most importance since the second stage of labor during vaginal delivery is a continuous and dynamic

process. Quantitative description of the mechanical properties, i.e., constitutive law, of the levator ani muscles is also a prerequisite for computer modeling of pelvic floor structures and functions. However, despite the importance, there are still no publicly published data of the mechanical properties of the levator ani muscles. As an effort to fill this gap, one aim of this thesis research is to experimentally measure the visco-hyperelastic properties of levator ani muscles and form appropriate constitutive law suitable for computer modeling.

Most soft tissues have complex mechanical behaviors, often exhibiting nonlinear elasticity, finite strain, time-dependency, and anisotropy (*Fung*, 1993). So, reliable constitutive equations derived from rigorous experiments are vital for computer modeling of the pelvic floor structure. There are some reports about measuring stiffness of pelvic floor tissues, such as stiffness of ovine cervix (*Owiny et al.*, 1991), rat cervix (*Watanabe* 1988, *Buhimschi et al.* 2004b), rat vagina-supportive complex (*Moalli et al.*, 2005), and human cervical tissue (*Conrad and Ueland* 1976 & 1979). In all of these studies, the tissue stiffness was calculated from the experimentally recorded strain-stress curves, either being the slope of the linear region or the average of slopes over the whole strain region. Obviously stiffness data derived in these ways gives only approximate strain-stress relations of the tissues, and the underlying constitutive law is assumed to be either linear elasticity or the so-called 'hypoelasticity'. Indeed, these kind of constitutive laws are of no use for finite element modeling of soft tissues, since *hyperelasticity* is the only accurate and effective approach for modeling finite deformation of rubber-like and polymer materials, including soft tissues (*Rivlin and Saunders* 1952, *Fung* 1993). The key point of using the theory of hyperelasticity is to find appropriate forms of pseudo-strain energy functions for pelvic floor tissues. There exist a number of strain energy functions which have been shown to be applicable to soft tissues; however, the dilemma for modeling pelvic floor muscles is that there are still no rigorous experimental test data for fitting the parameters in these functions.

During vaginal delivery, the pelvic floor muscles undergo three-dimensional large deformations, and likely behave anisotropically due to the embedded muscle fibers. This complexity of mechanical behavior precludes the use of uniaxial test data for forming constitutive laws. Unfortunately, to our knowledge, there are still no published biaxial data about pelvic floor muscles. Therefore, it is not surprising that published pelvic floor models have 'borrowed' material properties from other soft tissues (combined with their own 'arbitrary' adjustments), such as cardiac tissue (*d'Aulignac et al.* 2005, *Martins et al.* 2007, *Parente et al.* 2008, 2009a & 2009b, and *Calvo et al.* 2009), tongue and facial muscles (*Lee et al.*, 2005), and skeletal muscles (*Li et al.*, 2008). In this dissertation, a biaxial tension testing system was developed (Appendix A), and was utilized to measure the biaxial visco-hyperelastic properties of pelvic floor muscles. The data obtained were used to fit strain energy functions suitable for finite element modeling.

When studying the biomechanics of the pelvic floor muscles involved in vaginal birth, it is important to quantify the effects of pregnancy on the mechanical properties of these muscles. In humans, the pelvic floor muscles are known to undergo a softening process during pregnancy so that they can attempt to accommodate stretch ratios of up to 3.26 without injury at vaginal delivery (*Lien et al.*, 2004). Pregnancy is known to reduce stiffness, yield point and breaking point of rat cervix (*Watanabe* 1988, *Buhimschi et al.* 2004b). The stretch modulus of ovine cervix has been shown to decrease gradually but progressively with advancing pregnancy (*Owiny et al.*, 1991). A recent study showed that softening of mice cervix during pregnancy is a unique phase of the tissue remodeling process characterized by increased collagen solubility, maintenance of tissue strength, and upregulation of genes involved in mucosal protection (*Read et al.*, 2007). A few human data have also been reported, including the reduction of stretch modulus of human cervical tissue related with spontaneous labor (*Conrad and Ueland*, 1976). A recent study on human cervix showed that cervical

stiffness decreases by 20% during gestation (*Bauer et al.*, 2009). A common limitation of these studies is that they only focused on tissue stretchability or stiffness, ignoring the time-dependent stress relaxation, which should also play an important role in how much stress develops in pelvic floor muscles. To our knowledge, there is no estimate of how much tissue relaxation changes due to pregnancy. In this thesis research, both the elastic and viscous properties are taken into consideration when studying the effects of pregnancy.

1.2.2 Computer models

In the past five years, several computer models of the female pelvic floor function have been published; most have used finite element methods. A pioneering model is by *Lien et al.* (2004) which, although a pure 3-D geometric model, was the first one to show how much levator ani muscles are stretched during vaginal birth. Since then, a series of finite element models based on the continuum approach have been published. These include models for pelvic floor muscles (*d'Aulignac et al.* 2005, *Lee et al.* 2005 & 2009, *Martins et al.* 2007, *Li et al.* 2008, and *Parente et al.* 2008, 2009a & 2009b), both pelvic floor and the anal canal (*Noakes et al.* 2006, 2008a & 2008b), pubic symphysis (*Li et al.* 2006 & 2007) and the vagina (*Chen et al.* 2009 and *Calvo et al.* 2009).

The physiological and structural complexity of the human pelvic floor during birth pose three challenges to finite element modeling:

1. Construct an anatomically realistic geometriccal model

2. Select appropriate constitutive equations for pelvic floor muscles

3. Simulate dynamic maternal-fetal interaction

The following literature review about finite element modeling of human pelvic floor focuses on these three topics.

1.2.2.1 Geometrical models of the pelvic floor structure

The first step of building a finite element model for human pelvic floor is to construct a geometrical model which can reproduce the realistic anatomy of the pelvic floor muscles. Using MRI scans and 3D-palpator measurements, Janda constructed a 3-D morphological data set of the pelvic floor based on a embalmed 72-year-old female cadaver specimen (*Janda et al.*, 2003), and his data (available online) were employed by some pelvic floor models (*d'Aulignac et al.* 2005, *Martins et al.* 2007, and *Parente et al.* 2008, 2009a & 2009b). The drawback of these data is that they were derived from cadaver and exhibit distorted spatial relations due to the complete lack of muscle tone. Other finite element models derived their geometrical models from in vivo magnetic resonance (MRI) scans. For example, a 3-D geometrical model, including the levator ani muscles, surrounding pelvic bones, organs, and the connective tissue origins and insertions, was rendered by lofting a series of axial MRI section images, at 5-mm intervals, from a 34-year-old living woman (*Lien et al.* 2004 and *Chen et al.* 2009). Nokes created 3-D finite element meshes based on cryosection photographs from cadavers and MRI scans from a 32-year female volunteer (*Noakes et al.* 2006, 2008a & 2008b). Lee statistically extracted 3-d geometry of levator ani from MR scans of 15 nulliparous females (*Lee et al.* 2005 & 2009). In addition to MRI images, CT scan data have also been used to build the geometry of the pelvic structures (*Li et al.* 2006 & 2007).

1.2.2.2 Constitutive modeling of the pelvic floor muscles

Constitutive equations describe how a material responds to applied loads, which in turn depends on the internal composition of the material. For soft tissues, the modeling focuses on the dependence of stress on kinematic variables such as deformation gradient and rate of deformation. Although soft tissues, classified as mixture-composites, may exhibit inelastic behaviours, under certain conditions of interest it is

sufficient to model their behaviour within the context of the theory of finite elasticity (*Humphrey*, 2003).

The typical mechanical behaviours of levator ani during vaginal birth include finite strain, nonlinear elasticity, anisotropy, and time-dependency. The chosen constitutive equations for modeling levator ani should be able to capture these characteristics.

Nonlinear elasticity under finite strain

The theory of hyperelasticity has been successfully applied to model nonlinear elasticity under finite strain. The essence of this theoretical framework is that there exists a Helmholtz free-energy function, W, called the pseudostrain enery function, from which the stress can be derived. For example

$$\mathbf{S} = \frac{\partial W}{\partial \mathbf{E}} \tag{1.1}$$

where $\mathbf{S}$ is the second Piola-Kirchhoff stress tensor, $\mathbf{E} = (\mathbf{F}^T \cdot \mathbf{F} - \mathbf{I})/2$ is the Lagrange-Green strain tensor, and $\mathbf{F}$ is the deformation gradient. Generally the soft tissues are treated as incompressible due to high volume fraction of water inside tissues, then the corresponding 'modified' constitutive equation is

$$\mathbf{S} = \frac{\partial \tilde{W}}{\partial \mathbf{E}} - p\mathbf{C}^{-1} \tag{1.2}$$

where p is a Lagrange multiplier enforcing the constraint of incompressibility ($\det \mathbf{F} = 1$), and $\mathbf{C} = \mathbf{F}^T \cdot \mathbf{F}$ is the right Cauchy-Green tensor. The core of constitutive modeling is to choose suitable forms of function W (or $\tilde{W}$) that can reasonably well fit the observed material behaviours.

Fung postulated following form of strain energy function (*Fung* 1967, 1973, 1983,

1990 & 1993)

$$W = \frac{C}{2}\left(e^{Q} - 1\right) \tag{1.3}$$

$$Q = a_{ijkl}E_{ij}E_{kl} \qquad i,j,k,l = 1,2,3 \tag{1.4}$$

where a_{ijkl} are material parameters and repeated indices imply summation per the Einstein convention. Material symmetry can reduce the possible number of parameters in a_{ijkl} from $3^4 = 81$ to very few, for example, just 2 parameters for the isotropic materials. This 'Fung-type' approach was very popular when people first began to model soft tissues and it is still widely used today.

Another common way of characterizing isotropic incompressible hyperelastic material is to express the strain energy function in terms of strain invariants

$$W = W(I_1, I_2) \tag{1.5}$$

where $I_1 = tr\mathbf{C}$ and $I_2 = \frac{1}{2}\left[(tr\mathbf{C})^2 - tr\mathbf{C}^2\right]$ are the invariants of the right Cauchy-Green tensor $\mathbf{C}$ (here, $I_3 = \det \mathbf{C} = 1$ due to incompressibility). The most widely used invariant-based constitutive models for soft tissues are the *Mooney-Rivlin* model

$$W = C_{10}(I_1 - 3) + C_{01}(I_2 - 3) \tag{1.6}$$

and the *neo-Hookean* model

$$W = C_{10}(I_1 - 3) \tag{1.7}$$

Involving just one or two material parameters, these models are simple and reliable for both experimental data fitting and finite element implementation, and were used in some pelvic floor models (*Li et al.* 2008, *Noakes et al.* 2008b, and *Calvo et al.* 2009). However, since these two models use only linear functions of the invariants, they can

not reproduce the 'upturn' at higher strain levels in the strain-stress curve. For this reason, the Mooney-Rivlin model is sometimes extended to incorporate higher-order of invariants, and some pelvic floor model employed this kind of 'modifications' (*Li et al.* 2006 & 2007, and *Lee et al.* 2005 & 2009). The problem of the higher-order-invariant models is that they are sometimes not stable in finite element implementation.

It is worth to mention that a few pelvic floor models combined strain invariants into the exponential Fung-type strain energy function; examples are the models of *d'Aulignac et al.* 2005, *Martins et al.* 2007, and *Parente et al.* 2008, 2009a & 2009b.

Muscle fiber-induced anisotropy

Like other soft tissues, the pelvic floor muscles are mechanically anisotropic, i.e., their responses to applied loads depend on the orientation of the material. This directionally dependent behaviour is due to the presence of the fibers in the tissues. Among existing pelvic floor models, some authors have taken into consideration the muscle anisotropy (*Li et al.* 2006 & 2007, *d'Aulignac et al.* 2005, *Martins et al.* 2007, *Parente et al.* 2008, 2009a & 2009b, and *Calvo et al.* 2009), but most others were still based on the assumption of isotropy (*Lee et al.* 2005 & 2009, *Noakes et al.* 2006, 2008a & 2008b, and *Li et al.* 2008).

The simplest and most effective model for modeling anisotropic planar soft tissues, like the levator ani, is a *transversely isotropic representation*, which means that the material has a single axis (fiber orientation) of symmetry, and when rotated about this axis its response remains the same. Generally, there are two approaches, *phenomenological* vs. *microstructural*, to incorporate anisotropy into the hyperelastic strain energy functions.

In the phenomenological approach, the strain energy function takes the 'Fung-type' form (formula 1.3 on the preceding page), expressed directly in terms of the strain components of different directions. The material parameters are obtained by

directly fitting phenomenologically-observed experimental data, not involving preferred directions in the microstructure. One commonly chosen form of function Q (formula 1.4 on page 11) for transversely-isotropic tissue is

$$Q = \exp(a_1 E_{11}^2 + a_2 E_{22}^2 + 2a_3 E_{11} E_{22}) \tag{1.8}$$

where c, a_1, a_2, a_3 are material parameters, and the directions 1 and 2 are along and cross fiber, respectively. There are two difficulties in using the phenomenological approach: *(1)* no knowledge to guide somewhat arbitrary choice of the function Q; *(2)* high amount of of inter-specimen variability which in-turn translated into wide variability in material parameter values (*Sacks*, 2000). To our knowledge, no pelvic floor model ever used this approach to incorporate anisotropy.

The alternative microstructural approach is based on the continuum theory of fiber-reinforced composites (*Spencer*, 1984), where the strain energy function is expressed in terms of the invariants of the deformation tensor and the fiber direction

$$W = W(I_1, I_2, I_4) \tag{1.9}$$

where $I_4 = \mathbf{N}_f \cdot \mathbf{C} \cdot \mathbf{N}_f = \lambda^2$ is the 4th strain invariant, with $\mathbf{N}_f$ being the unit vector along the fiber direction under the reference (stress-free) configuration, and λ the stretch ratio along the fiber direction. For soft tissues, a common methodology is to decompose the strain energy into two parts

$$W = W_m(I_1, I_2) + W_f(\lambda) \tag{1.10}$$

where W_m represents the contribution from the deformation of the isotropic ground substance matrix, and W_f represents the contribution from the stretched fibers.

Motivated by the Fung-type function, exponential forms are generally chosen for

the function $W_f(\lambda)$. One popular form (already implemented in commercial finite element software LS-DYNA) was proposed by Weiss for modeling ligament (*Weiss* 1994, 1996 & 2001), and it was used to model the ligament part of human pubic symphysis (*Li et al.* 2006 & 2007). Another popular form (already implemented in commercial finite element software ABAQUS) was proposed by Holzapfel for modeling arterial wall (*Holzapfel et al.* 2000 and *Gasser et al.* 2006), which assumes that the directions of fibers are dispersed (with rotational symmetry) about a mean preferred direction. To date this model has not been used in any pelvic floor model, and it was employed in this thesis research. Some other different exponential functions for $W_f(\lambda)$ have also been used in pelvic floor models(*d'Aulignac et al.* 2005, *Martins et al.* 2007, *Parente et al.* 2008, 2009a & 2009b, and *Calvo et al.* 2009).

Time-dependent behavior

Due to large fraction of water in the constituent tissues, soft tissues exhibit both solid-like and fluid-like behaviours, i.e., the mechanical responses change with time. Characteristic behaviours include creep, stress relaxation, and hysteresis under cyclic loading. During vaginal birth the pelvic floor muscles are stretched under time-varying loading conditions, it is not surprising that time-dependent viscoelasticity plays remarkable role in the muscle mechanics. Except one model of the pubic symphysis (*Li et al.* 2006 & 2007), existing pelvic floor models have neglected this important temporal effect.

The theory of *quasi-linear viscoelasticity* (QLV), first proposed by Fung in 1972 (*Fung*, 1972), has been successfully used for modeling the viscoelasticity of soft tissues. In this theory, the second Piola-Kirchhoff stress at time t, $\mathbf{S}(t)$, is given by the convolution integral of strain history $\mathbf{E}(t)$ and the reduced relaxation function $\mathbf{G}(t)$:

$$\mathbf{S}(t) = \int_0^t \mathbf{G}(t-\tau) : \frac{\partial \mathbf{S}^e(\mathbf{E})}{\partial \mathbf{E}} : \frac{\partial \mathbf{E}(\tau)}{\partial \tau}\, d\tau \tag{1.11}$$

where $\mathbf{S}^e$ is the instantaneous nonlinear elastic response. The 4th-order tensor $\mathbf{G}(t)$ reduces to scalar $G(t)$ under the commonly-used assumption of isotropic viscosity, *i.e.*, the relaxation function is the same in all directions. Based on the observed relative insensitivity of the hysteresis to the loading frequency during cyclic loading, Fung further proposed a continuous relaxation spectrum for $G(t)$

$$G(t) = \frac{1 + c[E_I(t/\tau_2) - E_I(t/\tau_1)]}{1 + c\ln(\tau_2/\tau_1)}$$
$$\text{where} \qquad E_I(z) = \int_z^\infty \frac{e^{-y}}{y} dy \tag{1.12}$$

However, due to the difficulty in numerical implementation of the continuous spectrum representation, the reduced relaxation function is often approximated by a Prony series

$$G(t) = 1 - \sum_{i=1}^{n} g_i \left(1 - e^{-t/\tau_i}\right) \tag{1.13}$$

which has been employed in modeling the pubic symphysis (*Li et al.* 2006 & 2007).

Active muscle contraction

A few pelvic floor models have taken into consideration the active contraction of the levator ani muscle (*d'Aulignac et al.* 2005, *Martins et al.* 2007, and *Parente et al.* 2009b), by decomposing the fiber-induced strain energy into passive and active parts. However, in these models, both the chosen forms of 'active strain energy function' and the adopted values of material parameters were somewhat arbitrary and not well justified. Also, these papers did not discuss the benefits of including such additional complexity to the modeling of vaginal birth. Generally, near the end of the second stage of labor, the delivering woman is guided by mid-wife to relax her pelvic floor muscles, and active contraction of pelvic floor muscles tends to hinder vaginal birth. For these reasons, active contraction of the levator ani plays a negligible role in the late stages of vaginal birth, and therefore was ignored in this study.

1.2.2.3 Maternal-fetal interaction

Vaginal birth is a cyclic process in that dynamically-changing uterine and intraabdominal pushing pressures drive the fetus along the birth canal. This periodically stretches a 'ring' formed by the pubic symphysis and the 'U-shaped' ring of levator ani muscle. Modeling the continuously-changing maternal-fetal interaction is a highly nonlinear boundary value problem due to the possibility of intermittent contact and separation. Another challenge comes from the relatively big difference of stiffness between fetal head and maternal muscles, which renders the simulation progresses much slower in order to avoid 'numerical penetration'. Due to these difficulties, most of the existing pelvic floor models ignored maternal-fetal interaction and included only pelvic floor muscles in the geometrical model (*d'Aulignac et al.* 2005, *Lee et al.* 2005 & 2009, and *Noakes et al.* 2008b). In these models, pressures were applied statically on the pelvic floor muscles which obviously deviated far from the realistic dynamic contact loadings. Also, there are no specifications for setting the amplitudes of the driving pressures, and this explains why most of these papers either omitted the details of their pressure settings, or just used an averaged value of intra-abdominal pressure (IAP).

In the last two years, some pelvic floor models have begun to incorporate the maternal-fetal interaction (*Martins et al.* 2007, *Parente et al.* 2008, 2009a & 2009b, and *Li et al.* 2008). In these 'more realistic' models, a challenge arises: should the fetus, from the viewpoint of prescribing boundary condition, be driven in a 'displacement' or 'force' mode? All existing pelvic floor contacting models adopted the former, *i.e.*, applying translational and/or rotational displacements on the fetus. Since the six degrees-of-freedom (DOFs) of the fetus are completely constrained, the simulation can proceed readily. However, this is a modeling convenience, because (1) the results only reflect the static stretching status of the muscles; (2) there is no guide for prescribing the displacement profile; and (3) the 'back-and-forth' motion of fetus

can not be reproduced by prescribing displacements. Alternatively, a dynamically time-changing pressure profile can be prescribed to drive the fetus through the birth canal. However, realistic pushing profile, when combined with realistic geometry, will bring tremendous challenges to finite element simulation, because, in this case, most of the DOFs of fetus are unconstrained, making the progress of simulation unstable, slow, and unpredictable. To overcome this problem, very careful constraints are needed, such as adding additional bony structures, or adopted compromised modeling treatments, such as using simplified geometry. For these reasons, in part of this thesis, I chose to simplify the maternal and fetal geometry to an axisymmetric model to simulate the second stage of birth, with the fetal head being driven by realistic pushing profiles.

1.3 Specific aims

1.3.1 Conceptual model

Given the complexity of the biomechanical and other factors involved in the second stage of labor, we developed a simple conceptual model to organize the main factors in a coherent way. Specifically, we list in the model possible factors that may affect the biomechanical behavior of the pelvic floor structure during the second stage of labor, and the cause-and-effect relationships among them. Then, we highlight the factors that were studied respectively in each chapter of this thesis.

Figure 1.3 shows a conceptual (system analysis) model of our current understanding of the biomechanical interaction between fetal head and pelvic floor muscles during the second stage of labor. The greyed blocks represent the subjects that were studied in this dissertation.

Driven by intrauterine pressure (IUP), the fetal head contacts and stretches pelvic floor muscles, mainly levator ani and perineal body. During the second stage of labor,

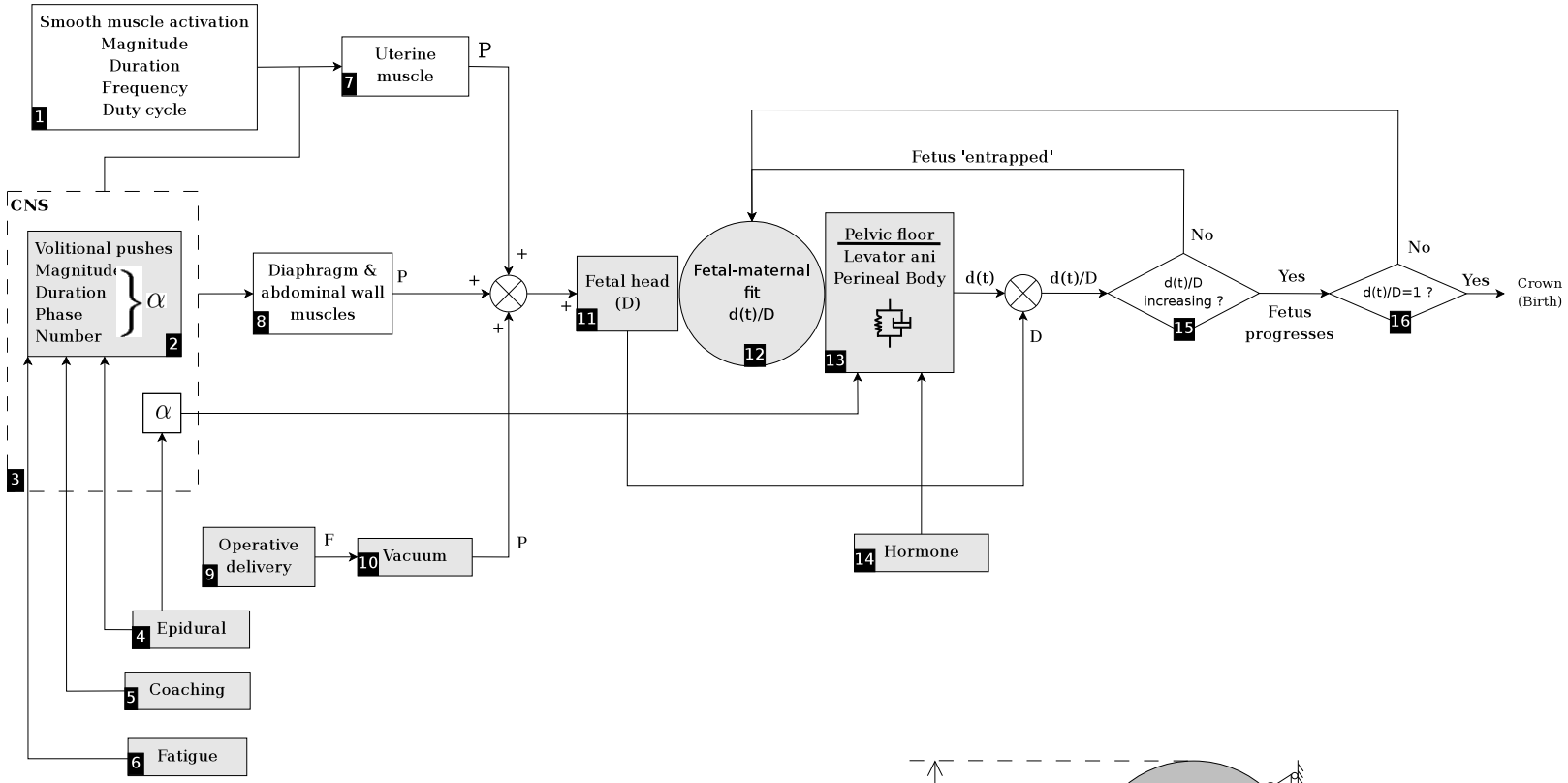

Fetal-maternal fit is parameterized by d(t)/D

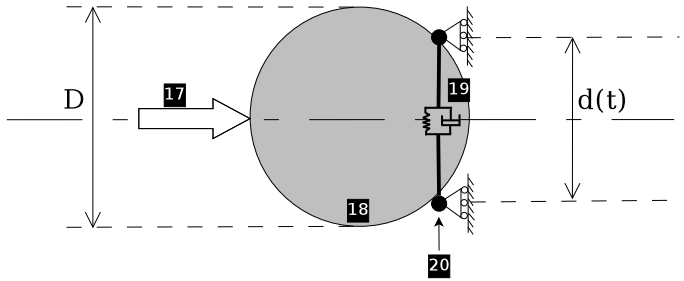

Figure 1.3: Conceptual model of the biomechanical fetal-maternal interactions during the second stage of labor. The fetal head is represented by a sphere, where the pelvic floor muscles are represented by a stretchable ring. The spring-dashpot-complex is used to represent the time-dependent mechanical properties of the pelvic floor muscles.

the mechanical interference between the fetal head and pelvic floor muscles, called fetal-maternal fit in this conceptual model, dynamically changes with time. To better visualize this interference, the system is conceptually simplified to a contacting pair, as shown in the low-right part of Figure 1.3. Here, the fetal head is represented by a sphere (18), while the pelvic floor muscles are represented by a mechanical analog consisting of spring and dashpot (19). For simplicity, it is assumed that the stretchable ring can accommodate only radial distention and no axial motion.

When the fetal head moves back and forth, the muscle ring correspondingly distends or shrinks back, and their changing interference (20) can be parametrized by $\frac{d(t)}{D}$, where $d(t)$ and D are the diameters of the muscle ring and the fetal head, respectively. There are two levels of feedback loop for updating $\frac{d(t)}{D}$. When the muscle ring is stretched, the interference parameter $\frac{d(t)}{D}$ is updated. If $\frac{d(t_1)}{D} < \frac{d(t_2)}{D}$, the fetus is moving forward, otherwise it is 'entrapped' without continuous progress. If $\frac{d(t)}{D} = 1$, the muscle ring already reaches the equator of the fetus head and birth can happen.

The motion of fetal head, and therefore the change of the fetal-maternal fit, are affected by the driving force derived from the intrauterine pressure (17), and the resisting force derived from the stretched muscle ring, determined by the mechanical properties of the pelvic floor muscles.

Driving force: Intrauterine pressure

The driving force to the fetus is generated from involuntary uterine contraction (7), and contraction of diaphragm and abdominal wall muscles (8). To study how sensitive labor duration is to changes in volitional pushing profiles, a 3-D axisymmetric finite element model was developed to study the energetics of the second stage of labor (Chapter V).

The uterine contraction is controlled by the activation of smooth muscles of uterus

(1), and this was not studied in this dissertation. Epidural (4), coaching from obstetrical professionals (5), and maternal fatigue (6) change, via the central nervous system (CNS) of the woman (3), the magnitude, duration, phase, and number of volitional pushes (2). A series of sensitivity analyses were implemented in this dissertation to study how these factors affect the duration of the second stage of labor (Chapters V, VII, and VIII).

When there is no continuous progress of delivery, operative delivery with forceps or vacuum is sometimes used by obstetrical professionals. In this case, operative delivery provides additional driving force to the fetus (9). A sensitivity analysis of the effect of using vacuum was also completed in this dissertation.

Resisting force: Pelvic floor muscles

The mechanical properties of the pelvic floor muscles determine the resistence to the fetal progress (13). The mechanical properties of pelvic floor muscles were measured, and anisotropic visco-hyperelastic constitutive laws of these muscles were developed for finite element modeling (Chapter IV). The effect of pregnancy on the mechanical properties were investigated by tests on pregnant and non-pregnant specimens collected from rat vagina and squirrel monkey pelvic floor muscles (Chapters II and III).

Both epidural (4) and hormone (14) can affect the stiffness of the pelvic floor muscles. A series of analyses were carried out to see how sensitive labor duration is to changes in material properties (Chapter VI).

1.3.2 Specific aims

The specific aims of this dissertation are as follows:

Aim 1: Develop a biaxial test system for biological soft tissues (Appendix A)

Multi-axial test data is vital for developing sound constitutive laws of soft tissues which take into consideration anisotropy of the mechanical properties. Therefore, a biaxial test system is needed for implement custom-made test protocols in order to characterize anisotropic visco-hyperelastic properties of pelvic floor muscles.

Aim 2: Investigate the effects of pregnancy on the mechanical properties of pelvic floor muscles (Chapters II & III)

Since this dissertation addresses the pelvic floor muscles in the second stage of labor, it is necessary to study how term pregnancy affects the mechanical properties of pelvic floor muscles. Due to the difficulty in collecting pregnant specimen from human being, experimental measurements were performed on rat vagina and squirral monkey. It is assumed that the results from specimens of rat and squirral monkey can be used to estimate how much material properties change due to pregnancy that occur in human beings. The primary null hypothesis tested is that term pregnancy does not affect the viscoelastic and failure properties of the tissues.

Aim 3: Develop anisotropic visco-hyperelastic constitutive laws of pelvic floor muscles for finite element modeling (Chapter IV)

Accurate constitutive laws of pelvic floor muscles are vital for finite element modeling of vaginal delivery. Therefore, an important aim of this dissertation is to develop constitutive equations for describing the anisotropic, time-dependent, and nonlinear behavior of pelvic floor muscles. The hypothesis is that it is possible to develop constitutive equations that is able to describe the anisotropic visco-hyperelastic behavior with coefficient of determination $R^2 \geq 80\%$.

Aim 4: Develop a 3-D finite element model for studying the energetics of the second stage of labor (Chapter V)

To date, all published finite element models of human birth process applied displace-

ment boundary conditions to the fetus, therefore precluded the possibility of study the energetics of the second stage of labor. This aim was to develop a feasible finite element model which can apply boundary conditions of time-varying intraabdominal pressure to the fetus head, therefore makes it possible to study the energetics of the second stage of labor.

Aim 5: Implement sensitivity analyses to investigate how sensitive the second stage of labor is to various biomechanical factors (Chapters VI, VII, and VIII)

It is important to know how various biomechanical factors affect the second stage of labor. The factors discussed in this dissertation include material property, operative delivery, and maternal fatigue. The hypothesis is that the duration of the second stage of labor is sensitive to these biomechanical factors.

Aim 6: Develop an improved real-geometry finite element model incorporating the constitutive laws developed in this dissertation (Chapter IX)

Up to now, due to lack of sound constitutive laws for describing pelvic floor muscles, all published real-geometry finite element models of the birth process borrowed' material properties from other soft tissues. This aim was to use the anisotropic visco-hyperelastic constitutive equations developed in Chapter IV to improve the modeling of pelvic floor structure. The primary hypothesis is that the developed theoretical model helps improve our understanding of the biomechanical behavior of the pelvic floor muscles during the second stage of labor and the mechanisms underlying the pelvic floor dysfunction.

CHAPTER II

The Effects of Term Pregnancy on the Biaxial Viscoelastic and Uniaxial Failure Properties of Rat Vagina Tissue

2.1 Introduction

During the second stage of labor in humans, the pelvic floor tissues undergo remarkable distension involving stretch ratio up to 3.2 (*Lien et al.*, 2004). This is a stretch limit that is seldom reached by soft tissues without failure in the non-pregnant states. Therefore, it is reasonable to believe the pelvic floor tissues undergo a remodeling process during gestation and become more distensible at term in order to accommodate the passage of the fetus.

Up to now, the quantitative effects of pregnancy on human pelvic floor striated muscle, perineal body, and vaginal tissues are unknown. However, there are animal data on the effects of pregnancy. For example, pregnancy reduces stiffness, yield point and breaking point of rat cervix (*Watanabe* 1988, *Buhimschi et al.* 2004b). The stretch modulus of ovine cervix decreases gradually but progressively with advancing pregnancy (*Owiny et al.*, 1991). A recent study showed that softening of mice cervix during pregnancy is a unique phase of the tissue remodeling process characterized by increased collagen solubility, maintenance of tissue strength, and upregulation of

genes involved in mucosal protection (*Read et al.*, 2007). A few human data have also been reported, including the reduction in stretch modulus of human cervical tissue with spontaneous labor (*Conrad and Ueland*, 1976). A recent study on human cervix showed that cervical stiffness decreases by 20% during gestation (*Bauer et al.*, 2009).

A quantitative understanding of how pregnancy affects the mechanical properties of levator ani muscle, perineal body, and vaginal tissues is vital to developing reliable biomechanical models for predicting vaginal birth. However, it is both ethically and practically difficult to collect tissue samples from women in parturition. For this reason, we resorted to animal data for gaining insights into the effects of pregnancy, and hypothesize that pregnancy has similar scaling effect on the mechanical properties in animal tissues as that on the properties in human tissues, including levator ani, perineal body and vaginal tissues.

To our knowledge, all published studies about the effects of pregnancy reported tissue stiffness or rupture limit; there is a paucity of data on its effect on the time-dependent properties. The second stage of labor is a continuous and dynamic process and therefore the time-dependent material properties inevitably play an important role in the mechanics of pelvic floor tissues. For this reason, it is necessary to quantify the effect of pregnancy on the time-dependent properties of tissues. In this study, vaginal tissues collected from both pregnant and non-pregnant rats were tested, and the following three null hypotheses were tested:

(1) The nonlinear elasticity of vaginal tissues of nulliparous pregnant rats does not differ at term from the nulliparous non-pregnant controls;

(2) The time-dependent relaxation of vaginal tissues of nulliparous pregnant rats does not differ at term from the nulliparous non-pregnant controls;

(3) The ultimate tensile strength and strain of vaginal tissues of nulliparous pregnant rats does not differ at term from the nulliparous non-pregnant controls;

2.2 Materials and Methods

2.2.1 Specimen preparation and test apparatus

Both pregnant and non-pregnant nulliparous Sprague Dawley rats were ordered from Charles River Inc. The animal strain is CD$^{@}$IGS, meaning that the plug date is considered to be day zero of gestation. The vendor bred female rats when they were 10-week old, and shipped them out at the 17th-day of pregnancy. Therefore, when the pregnant rats arrived at UM-ULAM lab, they were at 12.5-week gestation, $3 \sim 5$ days prior to the expected date of birth. Then, until delivery, the rats were kept in cages and closely monitored 24/7 using a night-vision IR surveillance system (Figure 2.1). In this way, it was guaranteed that the rats were sacrificed in the middle of delivery, and the collected vaginal tissues embodied at-term mechanical properties. For comparison, control specimens of vaginal tissues were also collected from non-pregnant female rats sacrificed at 13-weeks of age. Table 2.1 summarizes the rats used in this study.

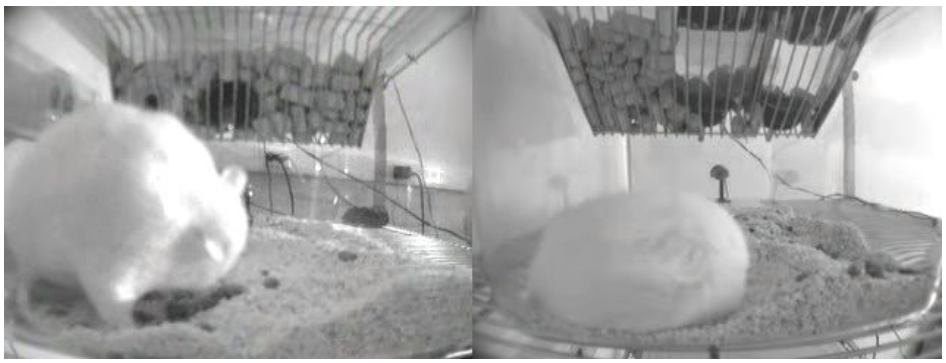

Figure 2.1: An remote surveillance system was set up for 24/7 monitoring of the rats until delivery. When labor began, the observer watching the screen went to the procedure room to sacrifice the animals and collect vaginal tissues. The surveillance system consisted of four night-vision IR bullet cameras (part: PVBULLETEXWP) and a GeoVision PCI DVR card (part: SYS-PCCARD-4CAM), vendored by PalmVID Inc.

Soaked in isotonic saline solution ($PH = 7.2 \pm 0.1$), the obtained vaginal tubes

Table 2.1: Overview of the rats used for studying the effect of pregnancy on the mechanical properties of rat vaginal tissue.

Number of rats:	Pregnant (24), Control (28)
Weight at sacrifice (g)*:	Pregnant (297.13 ± 33.47), Control (236.68 ± 18.92)
Length of pregnancy (days):	mean 22, maximum 23, minimum 21
Number of born pups at sacrifice**:	mean 4, maximum 7, minimum 2

* The weight of pregnant rats included the weights of unborn pups.
** Generally there are $10 \sim 12$ pups in each delivery (data from Charles River Inc.)

were kept frozen in freezer. At the day of testing, the tissues were thawed at room temperature and then cut into either thin square slabs for biaxial tests, or dogbone-shaped slabs for uniaxial failure tests.

A custom-made soft tissue test system was developed as part of this dissertation research to be capable of both uniaxial and biaxial tests. A detailed description of the system is presented in Appendix A. Briefly, four motor-driven stages are positioned along four orthogonal motion axes, providing up to four symmetric and stretching loadings to the specimens, Specimens were mounted to the test system by either sutures (biaxial test) or custom-made clamps (uniaxial tests). The specimens were orientated such that the two orthogonal loading directions were along and cross fiber, respectively. Tissue deformations were measured by recording the real-time movements of dark markers on the surface of specimens using a video tracking system. The loadings and marker positions were recorded continuously and synchronisingly at 10 Hz. An ultrasound thickness-measuring system was used to measure the cross-sectional thickness (and therefore the area) of the specimen, required for the stress calculation.

2.2.2 Test protocols

Equi-biaxial viscoelasticity tests

A total of 16 pregnant and 14 control specimens of rat vagina were used in biaxial viscoelasticity tests. The thawed specimen was cut into a square-shaped slab with edges aligned to the fiber and cross-fiber directions. For the rat vaginal tube, tissue fibers were aligned with the longitudinal direction. The typical specimen size used in this study was of $\sim$ 1.0 mm thickness and 10 $\sim$ 15mm length of each edge. The markers were positioned about 3 mm apart around the central region. The specimen was mounted to the test device in a trampoline-like fashion using three or four heavy-duty sutures and staples on each edge. In this way, the specimen can freely expand along the four lateral directions (Figure 2.2). With a custom-designed suture connector, the slackness of each suture can be adjusted individually so that all sutures were tightened so as to barely exert force.

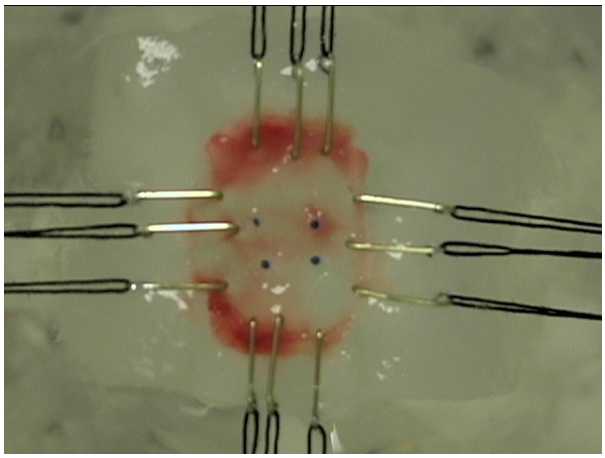

Figure 2.2: Fixation of thin square slab of specimen in biaxial test

Our pilot tests showed that applying $\sim$ 0.1 N loading can completely eliminate specimen slackness. Therefore, as a reference for all our tests on rat vaginal tissues, each specimen was preloaded to 0.1 N and the gauge positions of markers were stored.

This was followed by preconditioning - the specimen was cyclically stretched, in equi-axial mode, between 0 and 30% elongation for 5 cycles, with constant rate of 0.5 mm/sec, to ensure each specimen had settled before actual measurement began.

After the specimen had rested at its reference state for 15 minutes to recover, the specimen was equi-axially stretched in a 'ramp-and-hold' mode normal to the four edges. The stretching history and the corresponding stress response of a ramp-and-hold test is shown in Figure 2.3. The specimen was first linearly stretched up to 10 mm elongation at a constant rate of 1.0 mm/sec, then followed by a 90-minute static relaxation with the specimen being held at fixed stretched length. The forces along the two axes and the spatial movements of markers were continuously recorded at 10 Hz, and a MATLAB code was used to implement off-line video analysis for extracting 2-D strains.

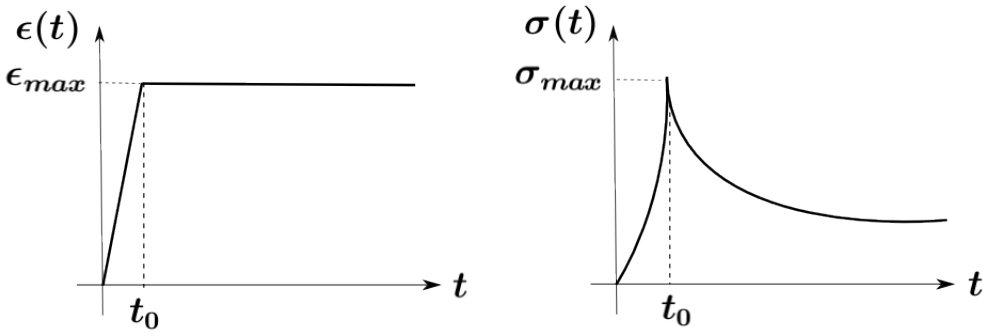

(a) Ramp-and-hold stretch (b) Stress response

Figure 2.3: The strain and stress histories in the ramp-and-hold stretch test. In all of the tests on rat vagina, the specimens were first linearly stretched up to 10 mm elongation at a constant rate of 1.0 mm/sec, then followed by a 90-minute relaxation at fixed stretching level. Thus, the time to reach peak strain ϵ_{max} was $t_0 = 10$ sec.

Uniaxial failure tests

A total of 12 pregnant and 10 control specimens of rat vagina were used in uniaxial failure tests. The circumferential (cross-fiber) direction was chosen as the loading direction in our unaxial failure tests, for two reasons: (1) during rat delivery the primary deformation of rat vaginal tube is radial distension; (2) it is assumed ad-hoc that the tissue is more compliant and easier to failure in the cross-fiber direction. To eliminate interference from the lateral constraint due to clamping, the specimen was cut into dog-bone shape, so that tissue deformation was localized in a 3×10 mm rectangular region where two markers aligned along loading direction were positioned (Figure 2.4-a). After the same referencing and preconditioning procedures as used in the biaxial test, the specimen was stretched at a constant rate of 0.1 mm/sec until specimen failure. Here a low stretching speed was selected to ensure quasi-static failure properties were obtained. The tissue failure is defined as the onset of a significant drop in recorded stress by more than 30%, and the corresponding ultimate tensile strength (UTS) and ultimate tensile strain (UTE) were extracted from the recorded stress-strain curve (Figure 2.4-b).

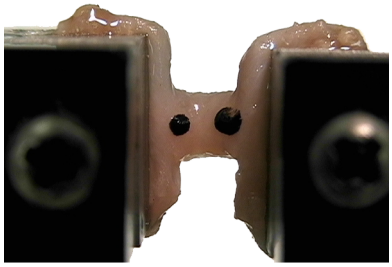

(a) Clamping of specimen

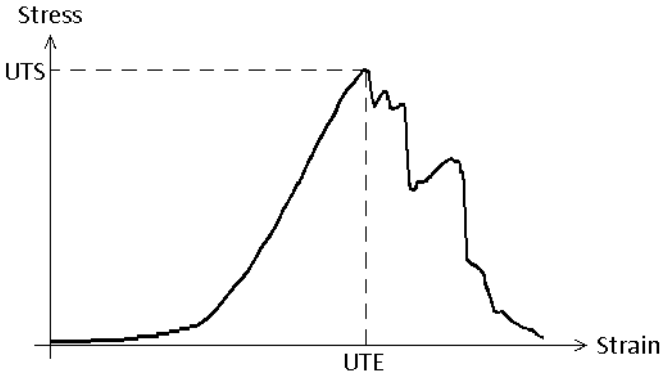

(b) Stress-strain curve

Figure 2.4: Uniaxial failure test. 'UTS' and 'UTE' denote the ultimate tensile strength and the ultimate tensile strain respectively.

2.2.3 Description of QLV theory

The quasi-linear viscoelastic (QLV) theory, proposed by Fung (*Fung*, 1972), was used to fit the strain and stress data. According to this theory, the 2nd Piola-Kirhhoff stress at time t, $\boldsymbol{S}(t)$, is expressed by the convolution integral of Green-Lagrangian strain $\boldsymbol{E}(t)$ and the reduced relaxation function $\boldsymbol{G}(t)$:

$$S_{ij}(t) = S^e_{kl}(0+)G_{ijkl}(t) + \int_0^t G_{ijkl}(t-\tau)\,\frac{\partial S^e_{kl}(E_{ij})}{\partial E_{ij}}\,\frac{\partial E_{ij}(\tau)}{\partial \tau}d\tau \tag{2.1}$$

where the superscript e represents instantaneous stress response. For our test condition $S^e_{kl}(0+) = 0$, the first term vanishes. $\boldsymbol{G}(t)$ is a 4th-rank tensor, consisting of 81 components. For symmetric biaxial loading condition, the shearing stress and strain are negligible, i.e. $S_{12} = 0$, and $E_{12} = 0$. Also, since tensor $\boldsymbol{G}$ is symmetric, we have $G_{ijkl} = G_{klij}$. Finally, the 81 components reduce to G_{1111}, G_{1122}, and G_{2222}. Here, the subscripts 1 and 2 denote the directions along and cross fiber, respectively. In this study, to simplify our analysis, the coupling of viscoelasticity along the two orthogonal loading directions was neglected, then we were left with two functions $G_1(t)$ and $G_2(t)$

$$S_i(t) = \int_0^t G_i(t-\tau)\,\frac{\partial S^e_i(E_i)}{\partial E_i}\,\frac{\partial E_i(\tau)}{\partial \tau}d\tau, \qquad i = 1,2 \tag{2.2}$$

where the Green-Lagrangian strains were calculated from stretch ratios as following

$$E_i = \frac{1}{2}\left(\lambda_i^2 - 1\right), \qquad i = 1,2 \tag{2.3}$$

with λ_1 and λ_2 being stretch ratios along and cross fiber respectively. Since the second Piola-Kirchhoff stress $\boldsymbol{S}(t)$ does not have straightforward physical meaning, it was only used for internal data analysis in this study. The results of stress were presented with the measure of Cauchy stress $\boldsymbol{\sigma}(t)$, also called true stress, which is the

force per unit *current* cross-sectional area. The two stress measures are related by

$$\boldsymbol{\sigma} = J^{-1}\boldsymbol{F}\cdot\boldsymbol{S}\cdot\boldsymbol{F}^{T} \tag{2.4}$$

Also, the results of strain are presented with stretch ratios for the purpose of straightforwardness. The details of how to extract stretch ratios, the second Piola-Kirchhoff stress, Cauchy stress, and Green-Lagrangian strains from experimental data are described in Appendix B.

To model the insensitivity of hysteresis to strain rate over several decades of change, a phenomenon commonly observed in dynamic tests of soft tissues, Fung proposed following continuous relaxation spectrum for representing the reduced relaxation function

$$G_i(t) = \frac{1 + C_i[E_I(t/\tau_2^i) - E_I(t/\tau_1^i)]}{1 + C_i \ln(\tau_2^i/\tau_1^i)}, \qquad i = 1, 2 \tag{2.5}$$

with

$$E_I(z) = \int_z^\infty \frac{e^{-y}}{y} dy$$

where the parameter C_i controls the degree of viscous effect, while parameters τ_1^i and τ_2^i govern the high- and low-frequency relaxations, respectively (*Sauren and Rousseau*, 1983).

An exponential function was used to fit the instantaneous elastic response

$$S_i^e(E_i) = A_i \cdot \left(e^{B_i \cdot E_i} - 1\right), \qquad i = 1, 2 \tag{2.6}$$

where A_i and B_i are constants. By taking derivatives, it can be seen that the product A_iB_i is the initial slope of the $S_i^e(t) \sim E_i(t)$ curve at $E_i = 0$, while B_i controls the (upswing) curvature of the curve.

2.2.4 Analysis of test data

The constants in QLV model, $\boldsymbol{\theta}_i = \{A_i, B_i, C_i, \tau_1^i, \tau_2^i\}$, $i = 1, 2$, were estimated by fitting experimental data. Here, the data in two loading directions, $i = 1, 2$, were fitted separately. When fitting viscoelastic data, it is commonly assumed that, if the ramping stretch is sufficiently fast, the stress relaxation in the ramp data is negligible. With this assumption, the instantaneous elastic response $\sigma^e(\epsilon)$ can be obtained by fitting the ramping data using relation (2.6), while the reduced relaxation function $G(t) = S(t)/S_{max}$, can be obtained by fitting the relaxation data using relation (2.5). However, since it is impossible to apply a step increase in strain, the ramp data inevitably embody stress relaxation, therefore the obtained instantaneous tissue stiffness is underestimated. On the other hand, since the peak stress σ_{max} is not truly an instantaneous response, the obtained reduced relaxation function is overestimated.

To overcome the problems inherent in a finite-rate ramp stretch, a nonlinear optimization algorithm, based on Abramowitch's approach (*Abramowitch and Woo*, 2004), was used for analyzing test data. In this approach, the ramping and relaxation data were pooled together to directly fit the convolution integral of $S_i^e(E_i)$ and $G_i(t)$, therefore obviating the need to assume that relaxation is negligible during the ramp stage. The direct benefit of this approach is that relatively slower ramp stretching is permitted in the test. In this way, in addition to improved parameter estimation, some experimental challenges associated with high stretching rate, such as poorly approximated strain history and stretching instability of specimen, can be bypassed.

For a set of experimental data $(t_j, \hat{\sigma}_j)$, the material parameters, denoted by $\boldsymbol{\theta} = \{A, B, C, \tau_1, \tau_2\}$, can be obtained by solving following nonlinear optimization problem using the Levenberg-Marquardt algorithm

$$\min_{\boldsymbol{\theta}} \sum_j [\hat{\sigma}_j - \sigma(t_j, \boldsymbol{\theta})]^2 \tag{2.7}$$

A MATLAB code was written to numerically solve for model parameters.

Since this is a highly nonlinear optimization problem, the solution is sensitive to the initial guess of the parameter values. To overcome this issue, an initialization procedure based on Sauren's approach (*Sauren et al.*, 1983) was used to quickly extract approximate values of model parameters, the these values were used as the initial guesses for the nonlinear optimization. The formula for approximating model parameters is

$$\begin{cases} \tau_2 = e^{\gamma - K/\alpha} \\ \tau_1 = \tau_2 e^{1/\alpha} \\ C = \alpha \left[1 - \dfrac{1}{G(\infty)} \right] \end{cases} \tag{2.8}$$

where $\gamma \sim 0.577$ is the Euler's constant, α and K are the slope and intercept of linear regression of plot

$$\frac{G(t) - G(\infty)}{1 - G(\infty)} \sim \ln(t)$$

Therefore, by directly fitting using relation (2.6), combining with relation (2.8), an approximation of model parameters can be quickly calculated, serving as a reasonable initial guess of the optimization solution.

The data regression procedure described above was implemented for each specimen to extract material constants, then the regression results were presented by the mean and standard deviation values of these parameters. To see how pregnancy and fiber direction affect material properties, unpaired one-sided t-tests were also implemented, with $P < 0.05$ denoting a significant difference.

2.3 Results

2.3.1 Nonlinear elastic responses

The stress-strain relations predicted by nonlinear regression were compared with the experimentally measured stress-strain relations (Figure 2.5). Here, comparisons were carried out between pregnant and control specimens, and between the longitudinal and circumferential directions of the rat vaginal tubes. The regressed constants A and B governing the stress-strain relation are listed in Table 2.2.

Table 2.2: The regressed values of constants A and B (Mean±SD) for the stress-strain relation.

		Pregnant	Control	P-value
A	Long.	0.091 ± 0.015	0.151 ± 0.012	< 0.001
	Circ.	0.127 ± 0.025	0.145 ± 0.017	0.034
	P-value	0.025	0.816	
B	Long.	3.54 ± 0.338	3.85 ± 0.323	0.017
	Circ.	2.09 ± 0.287	2.952 ± 0.321	< 0.001
	P-value	< 0.001	< 0.001	

Note: The number of specimens for biaxial tests: pregnant(14), control(16). The P-values were from unpaired two-sided t-tests. The unit of A is MPa, and B is unitless.

The stress levels of pregnant tissues was considerably lower than those of control specimens, in both the longitudinal and circumferential directions. Except the P-value comparing CL and CC of 0.816, all other P-values were below 0.05, therefore the null hypothesis that pregnancy does not affect the stress-strain relation was rejected.

The test results demonstrated that, in addition to pregnancy, fiber orientation also notably affected the stress response of the tissues. The tissues were much stiffer in along the fiber (longitudinal) direction compared with across the fiber (circumferential) direction. This conclusion holds for both pregnant and control tissues.

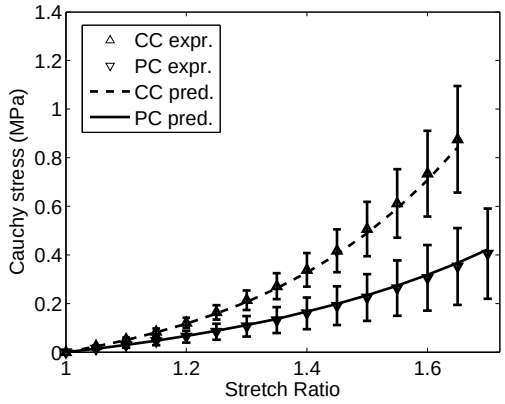

(a) CC vs. PC

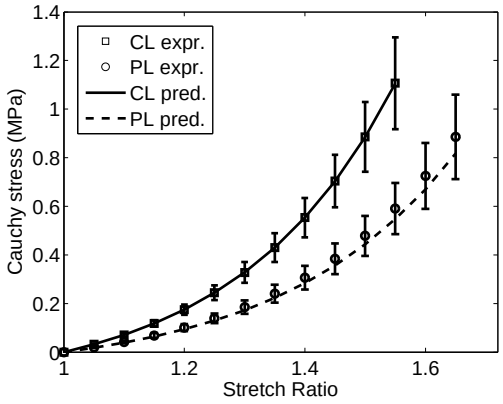

(b) CL vs. PL

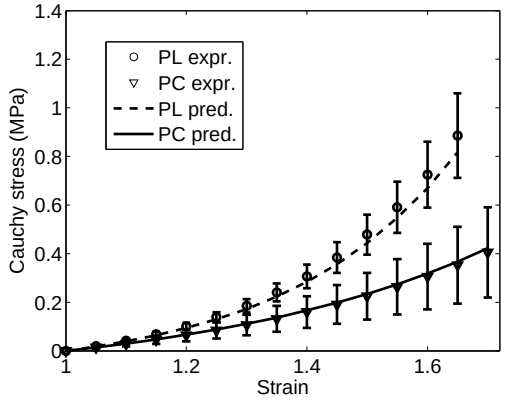

(c) PL vs. PC

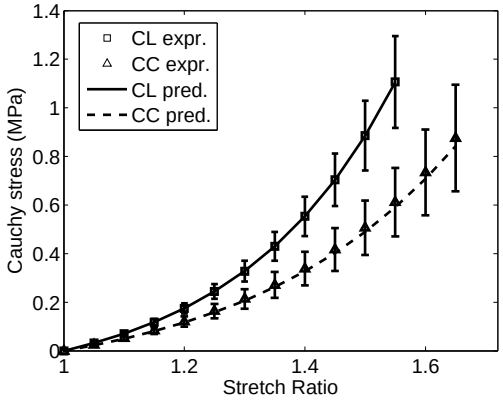

(d) CL vs. CC

Figure 2.5: Theretically predicted stress-strain relation versus experimentally measure stress-strain relation. The number of specimens for biaxial tests: pregnant (14), control (16). The notations of the specimens are: CC (control, circumferential), CL (control, longitudinal), PC (pregnant, circumferential), and PL (pregnant, longitudinal). The tissue fibers were aligned with the longitudinal direction of the rat vaginal tube. The stretch rate was 1.0 mm/sec.

2.3.2 Stress relaxation

The stress relaxation predicted by nonlinear regression was compared with the experimentally measured stress-strain relations (Figure 2.6). The regressed material constants C, τ_1, and τ_2 governing the relaxation behavior are listed in the Table 2.3. As the parameter most affecting the relaxation behavior, the constant Cs for pregnant tissues were significantly larger than those of control tissues ($P < 0.001$) in both fiber and cross-fiber directions, meaning that a higher degree of stress relaxation was

Table 2.3: The regressed values of constants C, τ_1, and τ_2 (Mean±SD) for relaxation behavior.

		Pregnant	Control	P-value
C	Long.	0.357 ± 0.047	0.187 ± 0.036	< 0.001
	Circ.	0.394 ± 0.062	0.202 ± 0.023	< 0.001
	P-value	0.004	0.708	
τ_1	Long.	0.673 ± 0.188	0.87 ± 0.264	0.115
	Circ.	0.584 ± 0.276	0.787 ± 0.235	< 0.001
	P-value	0.057	0.84	
τ_2	Long.	2124.31 ± 161.99	2624.31 ± 412.99	0.006
	Circ.	1886.28 ± 134.14	2389.16 ± 199.14	< 0.001
	P-value	0.001	0.218	

Note: The number of specimens for biaxial tests: pregnant(14), control(16). The P-values are calculated from unpaired two-sided t-tests.

induced by pregnancy. As for the short time constant, τ_1, no significant difference between pregnant and control tissues were observed in the longitudinal direction ($P = 0.115$), but it was observed in the circumferential direction ($P < 0.001$). The long time constant, τ_2, showed a significant difference between pregnant and control tissues in both longitudinal and circumferential directions ($P = 0.006$ and $P < 0.001$ respectively). The null hypothesis that pregnancy does not affect the stress relaxation behavior of the rat vaginal tissues was therefore rejected.

The results showed that fiber orientation has less influence on stress relaxation than pregnancy. For control tissues, the high P-values ($P = 0.708$, 0.84, and 0.218 for C, τ_1, and τ_2 respectively) comparing the longitudinal and circumferential directions indicate that the relaxation property is almost isotropic. For pregnant tissues, even though the P-values of C and τ_2 were 0.004 and 0.001, respectively, the P-value for τ_1 is 0.057, and the difference in stress relaxation due to fiber orientation is minimal (Figure 2.6-C).

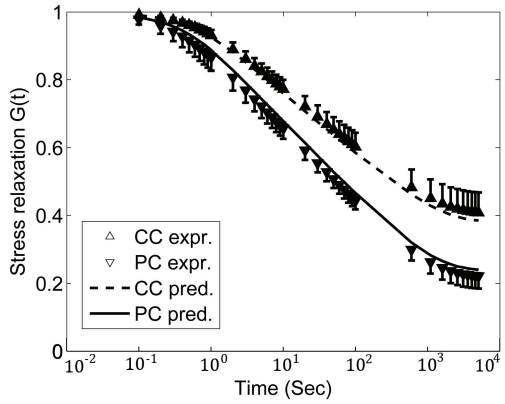

(a) CC vs. PC

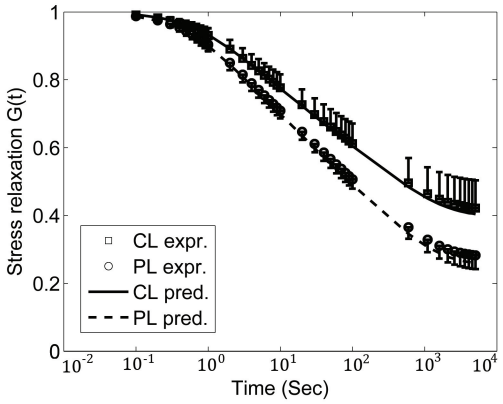

(b) CL vs. PL

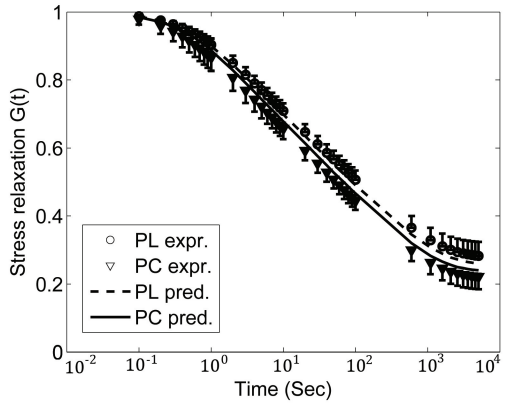

(c) PL vs. PC

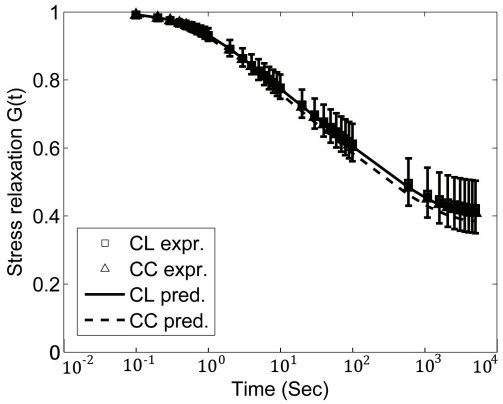

(d) CL vs. CC

Figure 2.6: Theretically predicted stress relaxation versus experimentally measure stress relaxation. The number of specimens for biaxial tests: pregnant(14), control(16). The notations of the specimens are: CC (control, circumferential), CL (control, longitudinal), PC (pregnant, circumferential), and PL (pregnant, longitudinal). The tissue fibers align with the lobgitudinal direction of the rat vaginal tube. The specimens were relaxed for 90 minutes. Only half of the error bar is displayed for visual clarity.

2.3.3 Uniaxial failure data

The uniaxial failure test data for both pregnant and control tissues are shown in Figure 2.7. To see how pregnancy affects the ultimate tensile strain (UTE) and ultimate tensile strength (UTS), these failure data are plotted in Figure 2.8, and the corresponding P-values from t-tests are listed in Table 2.4.

These test results demonstrated that pregnancy not only makes rat vagina tissues

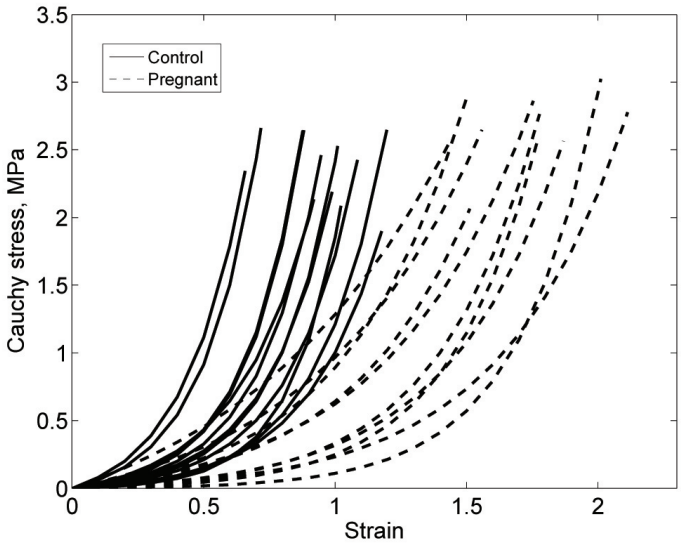

Figure 2.7: Experimental data of uniaxial failure tests on both pregnant and control rat vaginal tissues. The specimens were stretched along the circumferential (cross-fiber) direction with a stretching rate 0.1 mm/sec until failure.

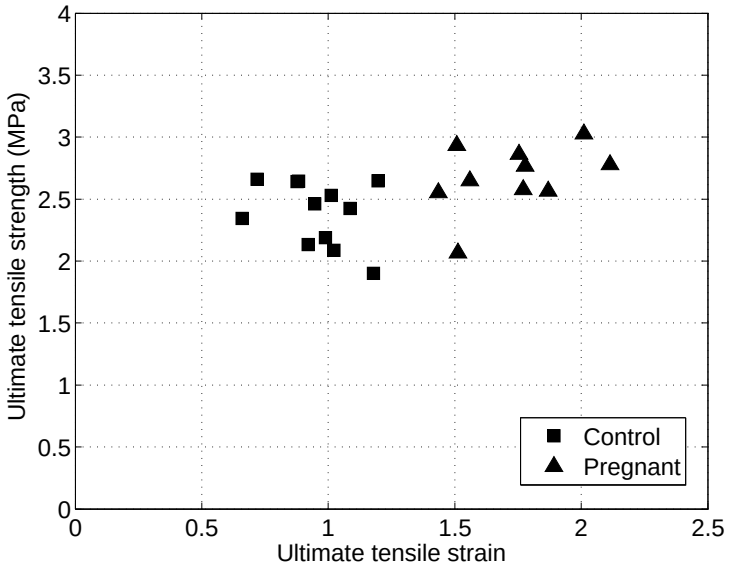

Figure 2.8: The ultimate tensile strain (UTE) and ultimate tensile strength (UTS) of rat vagina along circumferential (cross-fiber) direction. Note, the UTS used here is the Cauchy (true) stress, i.e., force per unit of current area.

more extensible, but also more tolerant to higher stress levels. Compared with control tissues, the pregnant tissues had both higher ultimate tensile strain ($P < 0.001$) and

Table 2.4: The (Mean±SD) ultimate tensile strain and ultimate tensile strength of rat vaginal tissues in the cross-fiber direction.

	Pregnant	Control	P-value
UTE	1.731 ± 0.227	0.957 ± 0.163	< 0.001
UTS (MPa)	2.676 ± 0.304	2.388 ± 0.258	0.02

The number of specimens: pregnant(14), control(16). The P-values are calculated from unpaired two-sided t-tests.

higher ultimate tensile strength ($P = 0.02$). Therefore, the null hypothesis that pregnancy does not affect the failure properties of rat vagina tissue was rejected.

2.4 Discussion

To our knowledge, published studies about the effect of pregnancy on the mechanical properties of soft tissues have all been based on uniaxial tests, and the time-dependent properties were ignored. The study of rat vagina tissues in this thesis is the first investigation of how pregnancy affects the viscoelastic properties using biaxial tests. The most important finding was that pregnancy not only decreases the tissue stiffness by at least two-fold, but also makes the tissue more viscous (fluid-like), with long-term stress level decreased by nearly two-fold. These findings indicate that the rat vagina tissue appears to undergo considerable adaptation to accommodate the extreme extension of vagina during labor. It is likely that pregnancy-related hormones play an important roles in this adaptation, but a historical study was not carried out in this thesis.

Our failure data showed that the ultimate tensile strain for the pregnant specimen was significantly higher than the control specimens ($P < 0.001$), agreeing well with literature data; for example, a study by Buhimschi showed that pregnancy reduced the breaking point (in length, mm) of the rat cervix (*Buhimschi et al.*, 2004a). However,

their paper also stated that pregnancy reduced the yield point (in force, N) of the rat cervix. The present study contradicts that finding in that the ultimate tensile strength of pregnant specimens was higher than that of control specimens. This disparity can be explained as follows. In the literature (*Buhimschi et al.*, 2004a), the yield point was represented with a tension force. In our study, the UTS is represented by Cauchy stress, which was calculated as the tension force divided by deformed cross-sectional area (CSA). The decrease of CSA nullified the effect of decreasing tension force, keeping the calculated UTS at a relatively high value.

The biaxial tests help to reveal the anisotropy of tissue properties induced by fibers embedded inside the tissues. Our test results showed that fiber markedly increases the tissue stiffness by nearly two-fold. However, it is interesting to note that there was no pronounced difference in stress relaxation with respect to fiber orientation.

The specimens of pregnant animals used in existing published studies were generally collected either during late-pregnancy or at postpartum.In this study, all specimens of pregnant rats in this study were collected during delivery. Therefore, our data and results can provide information more closely relevant to our goal of study, namely how the changes in tissue properties facilitate vaginal birth.

The main limitation of this study is that, to simplify data analysis, the coupling of viscoelasticity between along and cross fiber directions were neglected. Therefore, the decomposed equation (2.2) was used to approximate the tensor equation (4.17). Also, uncoupled equation (2.6) is used to describe instantaneous elastic responses in two directions. Since the goal of this study is to quantify the effect of term-pregnancy on the viscoelasticity of rat vagina in the along- and cross-fiber directions, these decomposition are acceptible. However, when the goal is to develop constitutive law of the tissue, as in Chapter IV, the coupling between two loading direction has to be taken into consideration.

CHAPTER III

The Effects of Term Pregnancy on the Biaxial Viscoelasticity and Uniaxial Failure Properties of Pelvic Floor Muscles of Squirral Monkey

3.1 Introduction

The study in this chapter was motivated by the same goal as the Chapter II, but the tests were performed on the levator ani muscle of squirrel monkey. We extended our tests of the effect of pregnancy to monkey for two reasons. First, there is no pelvic floor muscle in rat; secondly, we believe monkey, as a non-human primate, share similar pelvic floor anatomy as human, therefore be able to provide more relevant information for understanding how pregnancy affect the mechanical properties of human pelvic floor tissues. Biaxial ramp-and-hold viscoelasticity tests were performed on the levator ani and perineal body specimens collected from both nulliparous pregnant and nulliparous non-pregnant squirrel monkeys. For the reason of expense, we could not collect sufficient number of specimens, so the failure test was not carried out in this study. Following two hypotheses were tested:

(1) The nonlinear elasticity of the levator ani muscle of nulliparous pregnant squirrel monkey do not differ at term from that of the nulliparous non-pregnant controls;

(2) The time-dependent relaxation of the levator ani muscle of nulliparous pregnant squirrel monkey do not differ at term from that of the nulliparous non-pregnant controls;

3.2 Materials and Methods

There nulliparous non-pregnant and three nulliparous pregnant squirrel monkeys were sacrificed at University of Texas at Austin, and each animal were dissected into two intact sides, one side for histological study in UTA, while the other half side was delivered to University of Michigan for biomechanical tests. In the Biomechanics Research Lab at UM, a total of 3 pregnant and 3 non control levator ani specimens were collected for biaxial tension tests (Figure 3.1).

Figure 3.1: Dissection of squirrel mokey to collect the levator ani specimen.

The test device and testing protocols were the same as those used for testing on rat vagina, and the details are described in Chapter II. In short, the specimens were cut into square-shaped slabs with edges aligned to the fiber and cross-fiber directions.

The typical specimen size was $\sim$ 2.0 mm thickness and 10 $\sim$ 15mm length of each edge. The specimen was equi-axially stretched on four edges in a 'ramp-and-hold' mode at a constant rate of 1.0 mm/sec, then followed by a 90-minute relaxation with the specimen being held at fixed stretch length. The forces along the two axes and the spatial movements of markers were continuously recorded at 10 Hz.

The quasi-linear viscoelastic (QLV) theory, proposed by Fung (*Fung*, 1972), was used to fit the strain and stress data. The details of this theory and the data regression method are described in Chapter II.

3.3 Results

The experimentally recorded ramp-and-hold data of the levator ani specimens are plotted in Figure 3.2, and the material parameters from data regression are listed in Table 3.1.

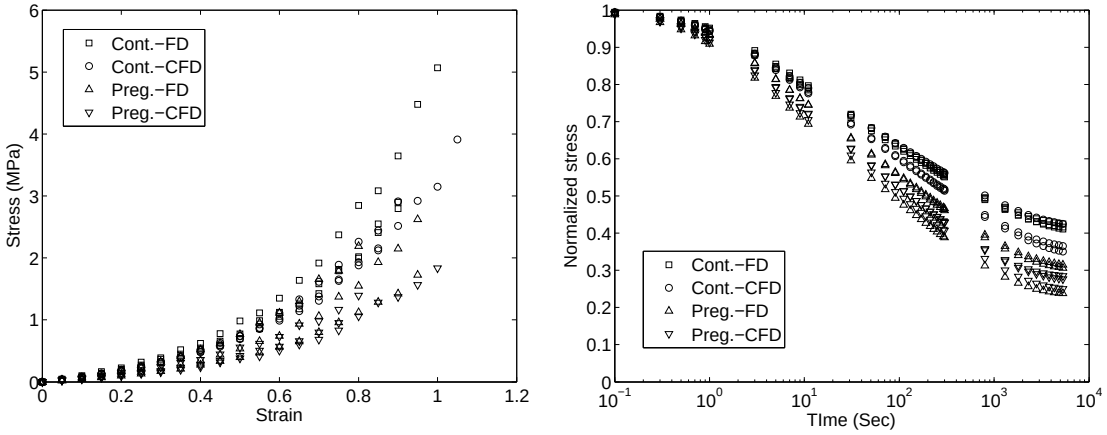

(a) Ramp data (b) Relaxation data

Figure 3.2: Experimental recorded ramp-and-hold data for the levator ani musle. The data were recorded at 10Hz, but only part of data were plotted her for clarity. Also, the data are separated into ramp and relaxation parts for easy plot, where the normalized stress is the relaxation stress divided by the peak stress. 'FD' and 'CFD' denotes along-fiber and cross-fiber directions.

Table 3.1: The (Mean±SD) material parameters from regression of experimental data.

		Pregnant	Control	P-value
A	FD	0.161 ± 0.04	0.255 ± 0.038	0.043
	CFD	0.168 ± 0.034	0.263 ± 0.026	0.018
	P-value	0.829	0.804	
B	FD	2.982 ± 0.206	2.874 ± 0.173	0.524
	CFD	2.54 ± 0.017	2.671 ± 0.216	0.435
	P-value	0.067	< 0.272	
C	FD	0.327 ± 0.005	0.179 ± 0.011	0.046
	CFD	0.347 ± 0.029	0.212 ± 0.037	0.007
	P-value	0.681	< 0.263	
τ_1	FD	0.973 ± 0.156	1.128 ± 0.132	0.262
	CFD	0.882 ± 0.065	1.163 ± 0.157	0.046
	P-value	0.403	0.781	
τ_2	FD	2776.6 ± 366.8	3466.2 ± 632.9	0.103
	CFD	2604.3 ± 174.1	4005.8 ± 461.5	0.008
	P-value	0.503	0.495	

Note: The P-values were from unpaired two-sided t-tests. The unit of A is MPa, and B is unitless. 'FD' and 'CFD' denotes along-fiber and cross-fiber directions.

As can be seen, the P-values comparing the pregnant and control specimens for the parameter 'A' are less than 0.05 (0.043 for FD and 0.018 for CFD), but they are all above 0.05 for parameter 'B' (0.829 for FD and 0.804 for CFD). Since 'B' controls the upswing curvature of the stress-strain curve, and 'A·B' denoted the initial slope of the curve at the zero strain, we can only say pregnancy affects the stress-strain curve at the toe region, but can not get definitive conclusion about the whole curve. Therefore, the first null hypothesis is not rejected.

The parameter 'C' are significantly different between pregnant and control specimens (0.046 for FD and 0.007 for CFD). Since 'C' is the most important parameter affecting the viscous behavior (*Sauren and Rousseau*, 1983), we can conclude that pregnancy significantly affect the relaxation behavior, and the second null hypothesis

is rejected.

For other material parameters, we can not conclude definitively whether pregnancy affect them significantly, since, depending on the fiber direction (FD or CFD), the P-value was either larger or lower than 0.05.

3.4 Discussion

The results presented in this chapter are preliminary due to the limited number of monkey specimens that were available. From the P-values in Table 3.1, it can be concluded that pregnancy significantly affects the viscosity of the levator ani muscle. However, we cannot conclude definitively whether the tissue stiffness is significantly affected by pregnancy. Since only 3 pregnant and 3 control specimens were tested, cross-specimen variations, especially any possible existence of 'outlier' data, may distract us from the true statistical significance underlying the experimental data. Therefore, conducting tests on more suirrel monkey specimens is necessary in order to draw definitive conclusions.

From our communication with Lisa Pierce, who dissected the squirrel monkey at the University of Texas at Austin and conducted histological study, we were informed that the levator ani muscle of squirrel monkey was lower in term pregnant animal (P=0.035), indicating remodeling took place during pregnancy.

In summary, the second null hypothesis was rejected but the first one was not. This conclusion still need tests on more specimens to support it. The issue of specimen availability in this chapter was from the budget constraint, and can be corrected if more specimens are available in future.

CHAPTER IV

Anisotropic Visco-Hyperelastic Properties of Human Pelvic Floor Muscles: Constitutive Laws for Finite Element Modeling

4.1 Introduction

Accurate constitutive equations of female human pelvic floor muscles are vital for finite element studies of vaginal delivery and birth-induced muscle injuries. Unfortunately, these kinds of material property data are not yet available. So, it is not surprising that existing published pelvic floor models have 'borrowed' material properties from other soft tissues, such as cardiac tissue (*d'Aulignac et al.* 2005, *Martins et al.* 2007, *Parente et al.* 2008, 2009a & 2009b, and *Calvo et al.* 2009), tongue and facial muscles (*Lee et al.*, 2005), and skeletal muscles (*Li et al.*, 2008).

The purpose of this study was to derive the constitutive laws of human levator ani muscle and perineal body required by finite element modeling. To measure the mechanical properties of these muscles, we developed a tensile testing system capable of conducting both uniaxial and biaxial tests on soft tissues. Since the deformation of pelvic floor muscles during the birth process is time-dependent, finite and nonlinear, the constitutive framework adopted here is anisotropic visco-hyperelasticity. A specific form of anisotropic constitutive equation proposed by Holzapfel was chosen for

this study (*Holzapfel et al.*, 2000). The explicit constitutive formulas for this model under our biaxial test condition are derived in this chapter, and the model parameters were determined by fitting biaxial experimental data. Since this model has been implemented in the commercial finite element code, ABAQUS, the results obtained can directly facilitate finite element modeling of the human pelvic floor.

4.2 Materials and methods

4.2.1 Constitutive modeling

4.2.1.1 Continuum mechanics preliminaries

The mathematics of the biaxial test are generally based on following assumptions:

- The deformation of the target central region is homogeneous if the region size is small relative to the specimen size;
- The tissue is incompressible;
- In-plane shearing is negligible considering symmetric and orthogonal loadings on rectangular thin specimen;

Based on these assumptions, the *deformation gradient tensor* around the central target region can be expressed as

$$\mathbf{F} = \frac{\partial \mathbf{x}}{\partial \mathbf{X}} = \begin{bmatrix} \lambda_1 & 0 & 0 \\ 0 & \lambda_2 & 0 \\ 0 & 0 & 1/(\lambda_1\lambda_2) \end{bmatrix} \tag{4.1}$$

where λ_1 and λ_2 are stretch ratios in the two orthogonal in-plane directions. Note, the incompressibility condition, $\det \mathbf{F} = 1$, is enforced by setting the off-plane stretch ratio $\lambda_3 = 1/(\lambda_1\lambda_2)$. The vectors $\mathbf{x}$ and $\mathbf{X}$ represent the positions of material particles

in the undeformed and deformed configurations. The *right* and *left Cauchy-Green* tensors are, respectively,

$$\mathbf{C} := \mathbf{F}^T\mathbf{F}, \qquad \mathbf{B} := \mathbf{F}\mathbf{F}^T \tag{4.2}$$

and their first three *invariants* are

$$I_1 = tr\mathbf{C} = \lambda_1^2 + \lambda_2^2 + \frac{1}{\lambda_1^2\lambda_2^2} \tag{4.3}$$

$$I_2 = \frac{1}{\lambda_1^2} + \frac{1}{\lambda_2^2} + \lambda_1^2\lambda_2^2 \tag{4.4}$$

$$I_3 = \det\mathbf{C} = (\det\mathbf{F})^2 = J^2 = 1 \tag{4.5}$$

In-plane anisotropy of fiber-reinforced tissue is often modeled by *transverse isotropy*, i.e., the material has axis (fiber orientation) of symmetry, and when rotated about this axis its mechanical response remains the same. In this case, an additional important invariant can be introduced

$$I_4 = \mathbf{N}\cdot\mathbf{C}\mathbf{N} = \lambda_f^2 \tag{4.6}$$

where $\mathbf{N}$ is the unit vector in the fiber direction under the reference (undeformed) configuration, and λ_f is the stretch ratio of fiber. Here, only one family of fibers is assumed. We assume the fibers are continuously embedded in ground substance matrix and, under deformation, it moves 'seamlessly' with the surrounding material points. Therefore, we can assume $\lambda_f = \lambda_1$ if, without loss of generality, the 1-st coordinate aligns with fiber direction.

For an incompressible, transversely isotropic, hyperelastic material, the pseudo strain energy can be decomposed into three parts

$$\begin{aligned} W &= W(I_1, I_2, I_3, I_4) \\ &= W_m(I_1, I_2) + W_f(\lambda_1) - \frac{p}{2}(J-1) \end{aligned} \tag{4.7}$$

where W_m represents the contribution from the deformation of the isotropic ground substance matrix, and W_f represents the contribution from the stretch of fibers. The third term $(p/2)(J-1)$ enforces incompressibility with the scalar p serving as an intermediate *Lagrange multiplier* and being identified as a hydrostatic pressure.

Given the form of the strain energy function, the *Cauchy stress tensor* $\boldsymbol{\sigma}$, also called true stress, can be calculated by (*Holzapfel*, 2000)

$$\begin{aligned}\boldsymbol{\sigma} &= -p\mathbf{I} + 2\left[\left(\frac{\partial W_m}{\partial I_1} + I_1\frac{\partial W_m}{\partial I_2}\right)\mathbf{B} - \frac{\partial W_m}{\partial I_2}\mathbf{B}^2 + I_4\frac{\partial W_f}{\partial I_4}\mathbf{n}\otimes\mathbf{n}\right] \\ &= -p\mathbf{I} + 2\left[\left(\frac{\partial W_m}{\partial I_1} + I_1\frac{\partial W_m}{\partial I_2}\right)\mathbf{B} - \frac{\partial W_m}{\partial I_2}\mathbf{B}^2\right] + \lambda_1\frac{\partial W_f}{\partial \lambda_1}\mathbf{n}\otimes\mathbf{n}\end{aligned} \tag{4.8}$$

where the operator $\otimes$ denotes the tensor product, or the dyad, of two vectors. Vector $\mathbf{n}$ is the unit vector in the fiber direction under the current (deformed) configuration, and if, without loss of generality, setting the current fiber direction as the local 1-direction, we have

$$\mathbf{n}\otimes\mathbf{n} = \begin{bmatrix} 1 & 0 & 0 \\ 0 & 0 & 0 \\ 0 & 0 & 0 \end{bmatrix} \tag{4.9}$$

4.2.1.2 Hozalpfel's transversely isotropic hyperelastic model

The specific form of strain energy function W proposed by Holzapfel wes chosen in this study (*Holzapfel et al.* 2000 and *Gasser et al.* 2006). It was chosen for two reasons: (1) it is easy to implement and has been successfully used for some anisotropic soft tissues, such as the artery wall; and (2) this model has been implemented in ABAQUS, a commercial finite element code. In this model, the neo-Hookean model is used for the isotropic ground substance matrix

$$W_m = C_{10}(I_1 - 3) \tag{4.10}$$

Only one family of fibers is considered in this study, even though the original model can account for more. The corresponding form of function W_f is

$$\begin{aligned} W_f &= \frac{k_1}{2k_2}\left(e^{k_2\langle E_f\rangle^2}-1\right) \\ \text{with} \quad E_f &:= \kappa(I_1-3)+(1-3\kappa)(I_4-1) \end{aligned} \tag{4.11}$$

where the operator $\langle\cdot\rangle$ stands for the Macauley bracket and is defined as $\langle x\rangle = (|x|+x)/2$. The model assumes that the direction of collagen fibers are dispersed (with rotational symmetry) about a mean preferred direction (*ABAQUS*, 2008). The parameter $\kappa\,(0 \le \kappa \le 1/3)$, describes the level of dispersion in the fiber direction

$$\kappa = \frac{1}{4}\int_0^{\pi} \rho(\Theta)\sin^3(\Theta)d\Theta \tag{4.12}$$

with $\rho(\Theta)$ the orientation density function that characterizes the distribution. $\kappa = 0$ represents perfectly-aligned fibers (no dispersion) and $\kappa = 1/3$ represents randomly distributed fibers (isotropic material). In this study the fibers are assumed to be perfectly-aligned. Combining with $I_4 = \lambda_1^2$, the function of W_f reduces to

$$\begin{aligned} W_f &= \frac{k_1}{2k_2}\left[e^{k_2\langle\lambda_1^2-1\rangle^2}-1\right] \\ \text{or} \qquad \lambda_1\frac{\partial W_f}{\partial\lambda_1} &= \begin{cases} 2k_1\lambda_1^2(\lambda_1^2-1)e^{k_2(\lambda_1^2-1)^2} & \lambda_1 \ge 0 \\ 0 & \lambda_1 < 0 \end{cases} \end{aligned} \tag{4.13}$$

As can be seen, the collagen fibers can support only tension. There are three material parameters, C_1, k_1, and k_2, to be determined from fitting experimental data.

Substituting relations (4.9) and (4.10) into (4.8), we can obtain

$$\begin{aligned}\sigma_{11} &= -p + 2C_1\lambda_1^2 + \lambda_1\frac{\partial W_f}{\partial \lambda_1}\\ \sigma_{22} &= -p + 2C_1\lambda_2^2\\ \sigma_{33} &= -p + \frac{2C_1}{\lambda_1^2\lambda_2^2}\end{aligned} \tag{4.14}$$

The thin slab of specimen stretched by in-plane forces can be viewed as being under the generalized plane stress status, i.e., all out-of-plane stress components vanish. Therefore, the value of the intermediate Lagrange multiplier p can be solved by setting $\sigma_{33} = 0$. Substituting the obtained p value into σ_{11} and σ_{22}, finally we obtain the explicit constitutive formulas for calculating the two in-plane stress components under the case of biaxial tension test

$$\begin{aligned}&\text{Along fiber direction:} \quad \sigma_{11} = 2C_{10}\left(\lambda_1^2 - \frac{1}{\lambda_1^2\lambda_2^2}\right) + \lambda_1\frac{\partial W_f}{\partial \lambda_1}\\ &\text{Cross fiber direction:} \quad \sigma_{22} = 2C_{10}\left(\lambda_2^2 - \frac{1}{\lambda_1^2\lambda_2^2}\right)\end{aligned} \tag{4.15}$$

4.2.1.3 Model of viscoelasticity

The theory of *quasi-linear viscoelasticity* (QLV) was used to model the time-dependent behavior of the pelvic floor muscles (*Fung*, 1972). In this theory, the 2nd Piola-Kirchhoff stress at time t, $\mathbf{S}(t)$, is given by the convolution integral of Green-Lagrangian strain history $\mathbf{E}(t)$ and the reduced relaxation function $\mathbf{G}(t)$:

$$\boldsymbol{S}(t) = \boldsymbol{S}^e(0+)\boldsymbol{G}(t) + \int_0^t \boldsymbol{G}(t-\tau)\frac{\partial \boldsymbol{S}^e(\boldsymbol{E}(\tau))}{\partial \tau}d\tau \tag{4.16}$$

or, in indicial notation

$$S_{ij}(t) = S^e_{kl}(0+)G_{ijkl}(t) + \int_0^t G_{ijkl}(t-\tau)\,\frac{\partial S^e_{kl}(E_{ij}(\tau))}{\partial \tau}d\tau \tag{4.17}$$

where the superscript e represents instantaneous stress response. For our test condition $S^e_{kl}(0+) = 0$, the first term vanishes. $\boldsymbol{G}(t)$ is a 4th-rank tensor, consisting of 81 components. For symmetric biaxial loading condition, the shearing stress and strain are negligible, i.e. $S_{12} = 0$, and $E_{12} = 0$. Also, since tensor $\boldsymbol{G}$ is symmetric, we have $G_{ijkl} = G_{klij}$. Finally, the 81 components reduce to G_{1111}, G_{1122}, and G_{2222}. Here, the subscripts 1 and 2 denote the directions along and cross fiber, respectively. In this study, isotropic viscoelasticity is assumed, *i.e.*, $G_{1111}(t) = G_{1122}(t) = G_{2222}(t) = G(t)$. Finally, the QLV equation reduces to

$$\begin{aligned}
\text{Along fiber direction:} \quad S_{11} &= \int_0^t G(t-\tau)\left(\frac{\partial S^e_{11}(\lambda_1)}{\partial \lambda_1}\frac{\partial \lambda_1}{\partial \tau} + \frac{\partial S^e_{11}(\lambda_2)}{\partial \lambda_2}\frac{\partial \lambda_2}{\partial \tau}\right) d\tau \\
\text{Cross fiber direction:} \quad S_{22} &= \int_0^t G(t-\tau)\left(\frac{\partial S^e_{22}(\lambda_2)}{\partial \lambda_2}\frac{\partial \lambda_2}{\partial \tau} + \frac{\partial S^e_{22}(\lambda_1)}{\partial \lambda_1}\frac{\partial \lambda_1}{\partial \tau}\right) d\tau
\end{aligned} \tag{4.18}$$

where the instantaneous elastic response $S^2_{11}(\lambda_1, \lambda_2)$ and $S^e_{22}(\lambda_1, \lambda_2)$ can be calculated from relation (4.15) using following relation

$$\boldsymbol{S} = J\boldsymbol{F}^{-1}\boldsymbol{\sigma}\boldsymbol{F}^{-T} \tag{4.19}$$

A feature often observed in dynamic stretching tests of biological soft tissues is that the hysteresis is relatively insensitive to strain rate over several decades of change. Based on this observation, *Fung* (1973) proposed a continuous relaxation spectrum for $G(t)$

$$\begin{aligned}
G(t) &= \frac{1 + c[E_I(t/\tau_2) - E_I(t/\tau_1)]}{1 + c\ln(\tau_2/\tau_1)} \\
\text{with} \qquad E_I(z) &= \int_z^\infty \frac{e^{-y}}{y} dy
\end{aligned} \tag{4.20}$$

which provides a smooth,linear decrease from short to long relaxation times (Figure

4.1)

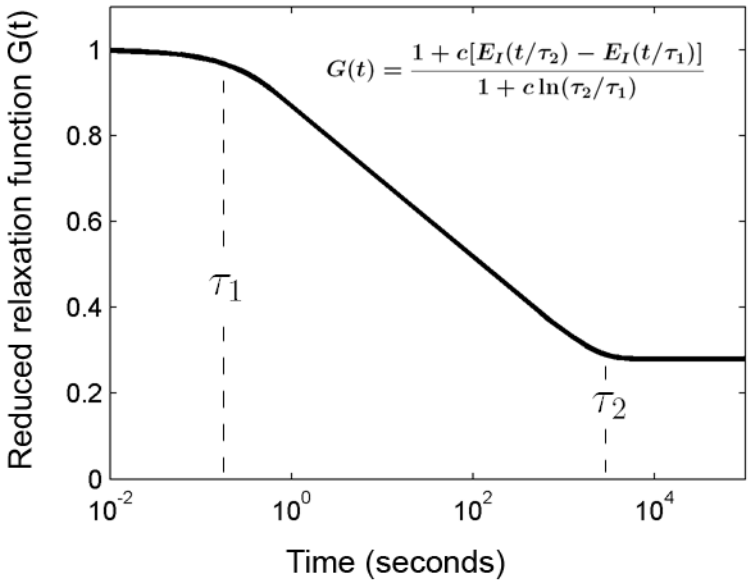

Figure 4.1: The continuous spectrum relaxation function proposed by *Fung* (1973). Here, τ_1 and τ_2 are short and long time constants, respectively, denoting the lower and upper limits of the constant damping range of the relaxation function.

However, due to the high discrepancy in parameter estimation and the difficulty in numerical implementation, the continuous spectrum representation of $G(t)$ is almost never used for numerical modeling. Instead, the Prony series is commonly used to approximate the $G(t)$ function

$$G(t) = 1 - \sum_{i=1}^{n} g_i \left(1 - e^{-t/\tau_i}\right) \tag{4.21}$$

where g_i and τ_i are relaxation parameters. The dilemma of using Prony series of the form (4.21) is that small n, such as 2, cannot reproduce the linear transition between short and long term relaxations, but larger n means too many parameters to estimate, leading to curve-fitting instability. To overcome this problem, the following special

form of Prony series is used in this study to approximate $G(t)$

$$G(t) = G_\infty + \frac{1 - G_\infty}{i_{max} - i_{min} + 1} \sum_{i=i_{min}}^{i_{max}} \exp\left(-\frac{t}{10^i}\right) \tag{4.22}$$

Here, $10^{i_{min}}$ and $10^{i_{max}}$ delimit the span of the linear relaxation transition, and G_∞ is the long-term normalized stress level. Characterized by equal spectral strength and relaxation times spread one decade apart, this function can provide reasonable approximation to relaxation behaviors with a span of linear transition (*Tschoegl*, 1989).

4.2.2 Estimation of model parameters

The two in-plane stretch ratios can be calculated by (see formula B.15 on page 179)

$$\text{Along fiber direction:} \quad \lambda_1(t) = \frac{1}{2} \frac{\left[x_1^{(4)}(t) - x_1^{(1)}(t)\right] + \left[x_1^{(3)}(t) - x_1^{(2)}(t)\right]}{\left[X_1^{(4)} - X_1^{(1)}\right] + \left[X_1^{(3)} - X_1^{(2)}\right]} \tag{4.23}$$

$$\text{Cross fiber direction:} \quad \lambda_2(t) = \frac{1}{2} \frac{\left[x_1^{(3)}(t) - x_1^{(4)}(t)\right] + \left[x_1^{(2)}(t) - x_1^{(1)}(t)\right]}{\left[X_1^{(3)} - X_1^{(4)}\right] + \left[X_1^{(2)} - X_1^{(1)}\right]} \tag{4.24}$$

where $X_i^{(m)}$ and $x_i^{(m)}(t)$, $m = 1, 2, 3, 4$ are the i-th component of the initial and current position vectors of the m-th marker, and $\mathbf{x}^{(m)(t)}$ can be from extracted from the recorded video images. The in-plane Cauchy stresses can be calculated by (see formula B.17 on page 180)

$$\text{Along fiber direction:} \quad \sigma_{11} = \lambda_1 F_1 / A_1 \tag{4.25}$$

$$\text{Cross fiber direction:} \quad \sigma_{22} = \lambda_2 F_2 / A_2 \tag{4.26}$$

where F_1 and F_2 are stretching forces applied along and transverse to the fiber directions, and A_1 and A_2 are the corresponding *initial* cross-sectional areas in the two

directions. The Appendix B gives the details of the derivations of these formulas. Then, the two components of the 2nd Piola-Kirchhoff stress, S_{11} and S_{22}, can be calculated using relation (4.19).

A methodology similar as the one used in Chapter II was used to regress on ramp-and-hold test data. Specifically, the ramping and relaxation data were pooled together to directly fit the equation (4.18). Here, numerical scheme is needed for calculating integration.

At a series of time instants t_i, $i = 1, 2, \cdots, n$, the deformation of the specimen, $\{\lambda_1(t_i), \lambda_2(t_i)\}$, the corresponding Cauchy stresses $\{\sigma_{11}(t_i), \sigma_{22}(t_i)\}$, and therefore the 2nd Piola-Kirchhoff stresses $S_{11}(t_i), S_{22}(t_i)$, were measured via camera and loadcell respectively. At the same time, the model-predicted stress values $\{\hat{S}_{11}(t_i), \hat{S}_{22}(t_i)\}$ can be calculated using formula (4.18). Then, solving for material parameters by curve-fitting experimental data is an optimization problem as following

$$\min_{\boldsymbol{\beta}} \sum_{i=1}^{n} \left\{ [\hat{S}_{11}(t_i) - S_{11}(t_i)]^2 + [\hat{S}_{22}(t_i) - S_{22}(t_i)]^2 \right\} \tag{4.27}$$

where $\boldsymbol{\beta}$ denotes the model parameter set

$$\boldsymbol{\beta} = \{C_{10}, k_1, k_2, i_{min}, i_{max}, G_\infty\}$$

This is a highly nonlinear optimization problem. In order to avoid the over-fitting problem in optimization, only part of the data points that represent the trend of the curve were used in optimization. Also, a constraint of $i_{min} < i_{max} \in \{-1, 0, 1, 2, 3, 4\}$ was used, since generally the spectrum of relaxation is within the range of $[10^{-1}, 10^4]$.

Note, the QLV theory requires the instantaneous elastic stress be based on the second Piola-Kirchhoff stress measure. However, this stress measure does not have straightforward physical interpretation, therefore it was used only for internal conversion here. In this study all results of stress were presented by Cauchy (true) stress,

which has a intuitive physical interpretation, force per current cross-sectional area.

4.2.3 Tissue testing

Pelvic floor specimens were collected from fresh female cadavers, soaked in isotonic saline solution and kept frozen at $-20\,^{\circ}\mathrm{C}$ in a freezer. At the day of testing, the tissues were thawed at room temperature. For the biaxial test, the specimens were cut into thin square shape, with $2 \sim 3$ mm thick and $10 \sim 15$ length of edge. Four dark markers, being $5 \sim 8$ mm apart, were placed on the surface of the specimen, symmetrically around the center of the specimen, and their motions were recorded by a video tracking system for calculating 2-D in-plane strains. The specimen was mounted to the test device in a trampoline-like fashion using staples and heavy-duty sewing sutures (Figure 4.2). For the uniaxial failure test, the specimens were cut into dog-bone shape. The length of the middle size-reduced region was about $10 \sim 15$ mm, and the cross-sectional area was about 5×5 mm^2. Two markers, less than 5 mm apart, were positioned at the surface of the specimen along the loading direction for measuring stretching strain.

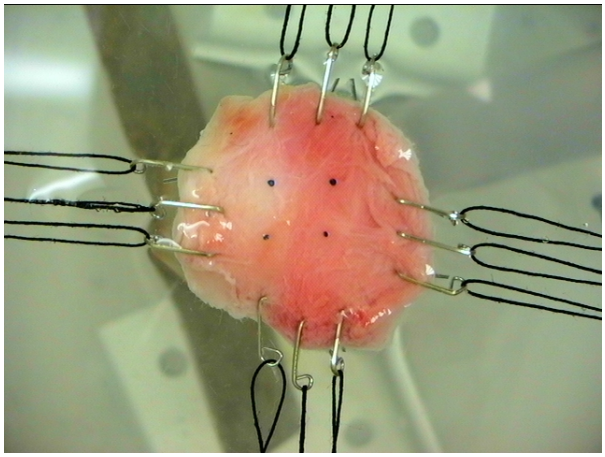

Figure 4.2: A specimen of pubovisceral muscle mounted with staples and sutures.

In the equi-axial ramp-and-hold tests, the specimens were stretched simultane-

ously along four edges at a rate of 1.0 mm/sec, while in the failure tests the specimens were stretched continuously at a rate of 0.1 mm/sec until failure. Here the low stretch speed was selected to ensure quasi-static failure property was obtained. The tissues used in these tests are summarized in Table 4.1. Here, the PVM and PIM were treated together as levator ani muscle, so their data were pooled together for regression and the obtained material parameters were deemed as to represent the levator ani muscle.

Table 4.1: The number of test specimens used in fitting the material properties.

	Biaxial ramp-and-hold tests	Uniaxial failure tests
PVM	5	4
PIM	2	3
PB	5	4

Abbreviations: pubovisceral muscle (PVM), puboiliococcygeal muscle (PIM), and perineal body (PB).

4.3 Results

Table 4.2: Material parameters obtained from data regression

	C_{10} (MPa)	k_1 (MPa)	k_2	G_∞	i_{min}	i_{max}
Levator ani muscle	0.3532	0.0827	0.3242	0.36	-1	3
Perineal body	0.5870	0.0287	0.6497	0.31	-1	3

The material parameters of levator ani muscle and perineal body, obtained by curve-fitting experimental data, are listed in Table 4.2. The comparisons between experimentally recorded and the model predicted time history of stresses are plotted in Figures 4.3 and 4.4.

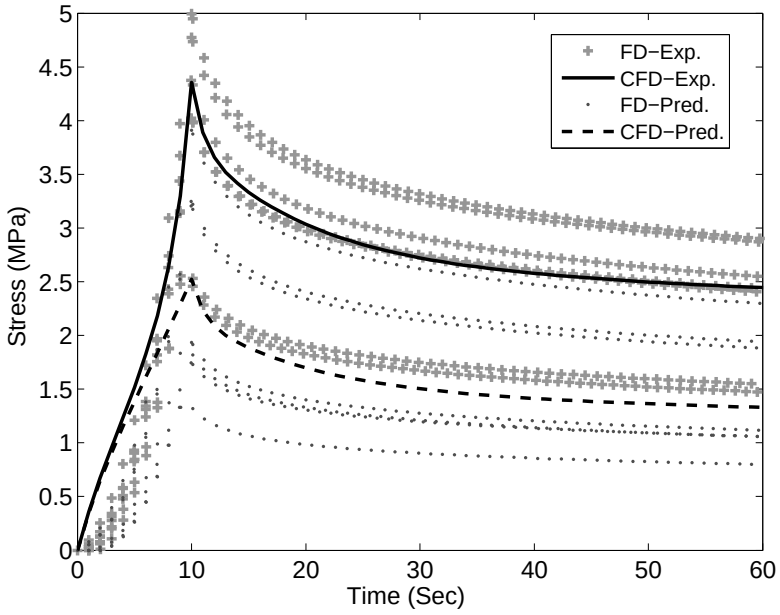

Figure 4.3: Comparison between experimentally recorded stress and model predicted stress for thelevator ani muscle. The R^2 values for FD and CFD are 0.72 and 0.75 respectively. The experimental data were recorded at 10 Hz over 1 hour. However, in this and the following figure, only part of data are shown here for clarity. The abbreviations 'FD' and 'CFD' represent the fiber and cross-fiber directions, respectively.

The experimentally recorded failure tests are shown in Figure 4.5, and the corresponding ultimate tensile strength (UTE) and ultimate tensile strain (UTE) are listed in Table 4.3.

Table 4.3: The ultimate tensile strengths (UTS) and ultimate tensile strains (UTE), for the levator ani muscle and perineal body, along the fiber directions (Mean±SD).

	Levator ani muscle	Perineal body
UTE	1.75 ± 0.19	1.78 ± 0.2
UTS (MPa)	7.65 ± 2.464	10.11 ± 2.86

4.4 Discussion

To our knowledge, there are no published material parameters describing the anisotropic visco-hyperelastic properties of human pelvic floor tissues. Therefore,

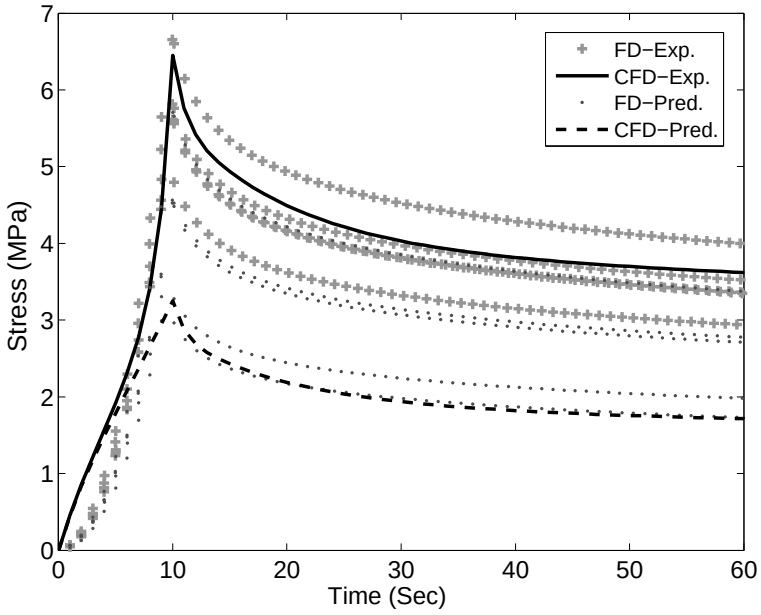

Figure 4.4: Comparison between experimentally recorded stress and model predicted stress for the perineal body. The R^2 values for FD and CFD are 0.78 and 0.62 respectively. The abbreviations 'FD' and 'CFD' represent fiber and cross-fiber directions, respectively.

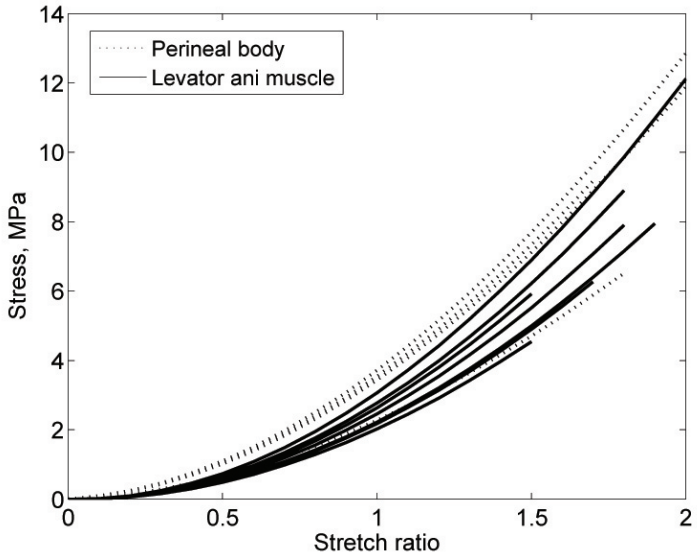

Figure 4.5: Failure test data for the levator ani muscle and perineal body

previous published computer models of pelvic floor structure 'borrowed' material properties from other soft tissues. This is the reason why the quantitative discussions

in those models focused on tissue strain rather than stress. The results from this study fills this knowledge gap, and will therefore help improve finite element simulations of on human pelvic floor muscles. Also, since the constitutive equation used in this study has been implemented in the popular ABAQUS finite element solver, it can be implemented feasibly and conveniently.

The curve-fitting methodology of regressing on whole test data, instead of separating into ramp and relaxation parts, precluded the assumption of negligible relaxation in the ramp data, therefore making it acceptable to use relatively lower ramp stretch rates in these tests. The nonlinear optimization of data regression converged rapidly and robustly.

One limitation of the constitutive equation used in this study is that the simple neo-Hookean model was used for modeling the isotropic ground substance matrix. As shown in Figure 4.3 and Figure 4.4, the coefficients of determination (R^2) were not satisfactory. The reason is that the one-parameter neo-Hookean model cannot describe the upswing curvature (hardening) of the stress-strain curve in the low and median strain range. Also, this model performs unsatisfactorily in modeling the tissue toe region, i.e., low stress in low strain region. This problem is especially obvious in curve-fitting the stress-strain curve along the cross-fiber direction. Using some more sound strain energy functions helps address this problem.

Several strain energy functions have been proposed to model the strain hardening in stress-strain curves at large strains. One family of such models is called *power law* models, initially proposed by *Knowles* (1977), in which the strain energy function takes the form

$$W = \frac{\mu}{2b}\left[\left(1 + \frac{b}{n}(I_1 - 3)\right)^n - 1\right] \tag{4.28}$$

where μ is the shear modulus, and b and n are dimensionless positive material constants.Letting $n \to \infty$, the power law reduces to the strain energy function that Fung proposed to describe biological materials (*Fung*, 1967). Another family of models is

called *limiting chain extensibility* model, initially proposed by *Gent* (1996), in which the strain energy takes the form

$$W = -\frac{\mu}{2} J_m \log\left(1 - \frac{I_1 - 3}{J_m}\right) \tag{4.29}$$

where μ is the shear modulus, and J_m is the constant limiting value for $I_1 - 3$. The stress is unbounded when $I_1 \to J_m + 3$.

Both of these two families of models have some molecular bases, and they model strain-hardening quite well. An interesting point is that both the power model and the limiting chain extensibility model reduce to the neo-Hookean model when letting $n = 1$ in (4.28) or letting $J_m \to \infty$ in (4.29), respectively. Therefore, both these two models can be used to correct the problem of poor curve-fitting using neo-Hookean model.

It worths to mention that the anisotropic viscohyperelastic model implemented in this study has been implemented in the popular commercial code ABAQUS. Therefore, material constants obtained here can be directly used as input for simulating the borth process using ABAQUS. When using other strain-hardening models, the increased number of material constants and more complicated forms of strain energy function may bring difficulty in the stability of nonlinear optimization. Also, in order to implement these models in commercial codes, for example ABAQUS, custom user subroutines have to be coded in FORTRAN language.

The results presented here are preliminary due to the limited number of human specimens that were available. Therefore, no detailed statistical analysis have been performed in this study. This weakness can be bypassed by testing more specimens in the future.

CHAPTER V

A Study of the Energetics of the Second Stage of Human Labor Using a 3-D Axisymmetric Finite Element Model

5.1 Introduction

The second stage of labor refers to the laboring period starting from when the cervix fully dilates until the fetus head crowns. During this period, the uterus contracts once every three minutes, with each contraction lasting about one minute. To deliver her baby, a woman has to supplement this by 'bearing down' (or 'pushing'), i.e., volitionally contracting her diaphragm and abdominal wall muscles, during each uterine contraction. This combined effort gradually helps drive the fetal head along the birth canal so that it passes through the 'ring' formed by the pubic symphysis and the 'U-shaped' ring of levator ani muscle (*Ashton-Miller and Delancey*, 2009).

The mean duration of the second stage of labor is almost 70 minutes, with 27% of patients having the duration exceeding 2 hours (*Schiessl et al.*, 2005). According to the definition by the American College of Obstetricians and Gynecologists (as of 2000), a *prolonged second stage of labor* refers to, in nulliparous patients, a lack of continuing progress over 3 hours with or 2 hours without regional anesthesia, and, in multiparous patients, a lack of progress over 2 hours with or 1 hour without regional

anesthesia (*ACOG*, 2000). It has been reported that prolonged second stage of labor has no or a weak association with poor neonatal outcomes, but is strongly associated with increased risks of adverse maternal and perinatal outcomes, and high rate of operative delivery (*Moon et al.* 1990, *Menticoglou et al.* 1995, *Myles and Santolaya* 2003, *Cheng et al.* 2004, and *Altman and Lydon-Rochelle* 2006). It is not surprising that during a prolonged second stage of labor many women may become exhausted and eventually need operative delivery (with forceps and/or vacuum). Forceps delivery, however, increases the risk of a levator ani defect by 14.7 (*Kearney et al.*, 2006) and the risk of perineal injury by 10-fold (*Christianson et al.*, 2003).

To speed up the labor process, the woman is coached by obstetricians or midwives to push in phase with the uterus contraction. A typical *coached pushing* style is a 10-second process during which the woman takes a deep breath, holds and bears down together with the uterine contractions (*Klein*, 2006). As to the pushing style, the coached push can be timed so as to take place before, during, and after the peak uterine contraction force. So, this raises the questions: When should the coached push be best timed relative to the peak uterine contraction and should it be repeated within one cycle of the uterine contraction? Medical professionals currently favor several different pushing styles, and there is no consensus about what the optimal pushing pattern is for the second stage of labor. Therefore, it would be helpful to know which pushing style maximizes the probability of vaginal delivery before the patient becomes exhausted. *Lien et al.* (2009) developed a simple 3-D model to examine pushing efficacy by varying the number and magnitude of pushes; in this model the pushing profiles were generated by a Gaussian function and the levator ani muscle was represented by viscoelastic bands. A push timed with peak uterine contraction was deemed most effective.

This study is an improvement over Lien's model in six respects: (1) a more general continuum mechanics approach was used to replace the geometrical approach; (2)

realistic pushing profiles, extracted from clinic records, were employed; (3) numerical implementation was based on finite element method instead of MATLAB Simulink; (4) the maternal-fetal-interaction was modeled using a dynamic contact condition instead of purely geometrical constraints; (5) a more accurate constitutive equation for levator ani muscle was used, derived from rigorous tests; (6) a sensitivity analysis covers not only the number and magnitude, but also the phase of the directed pushing. The goal of this study was to build a conceptual framework for modeling the energetics of the second stage of labor, by which a wider range of sensitivity analyses can be implemented, such as the effects of volitional pushing styles, muscle material properties, maternal fatigue, and operative delivery.

5.2 Methods

5.2.1 Geometrical model

To simulating the maternal-fetal interaction during the second stage of labor, the pelvic floor muscles would have to be represented by subject-specific real geometry, and the fetus would have to be driven by pushing force. This would make the finite element implementation slow, unstable, and unpredictable, due to lack of accurate motion constraints. For this reason, in all existing real-geometry pelvic floor models (*Martins et al.* 2007, *Parente et al.* 2008, 2009a & 2009b, and *Li et al.* 2008), a somewhat arbitrarily assumed motion path was used to constrain the motion of the fetus so that the simulation can proceed smoothly. In this study, our interest focuses on the maternal pushing patterns, therefore we want to keep realistic pushing profiles but we have to make a compromise on geometry by using simplified axisymmetric 3-D model. In this way, the motion of the fetus is completely determined by the pushing force and the maternal-fetal-interaction.

As a first-order approximation, the female pelvic floor was represented by a trun-

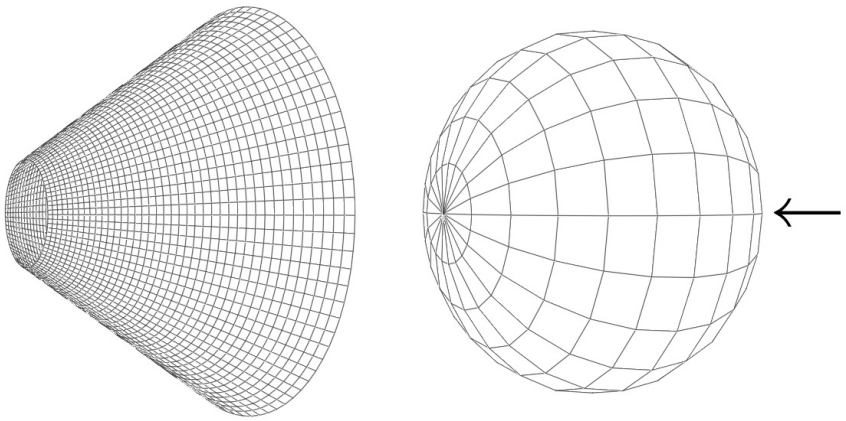

Figure 5.1: 3-D axisymmetric finite element model of the second stage of labor. Cyclic pushing force drives the fetal head, represented by a rigid sphere, moving along the 'birth canel', represented by a truncated cone.

cated conical membrane supported at its cranial edge. Considering the 10% reduction in size due to molding effect (*Carlan et al.*, 1991), a rigid sphere of 9 cm-diameter was used to represent the 50th percentile fetal head (*Chitty et al.*, 1994) (Figure 5.1). The simulation started from where the sphere just contacts the cone.

5.2.2 Governing equations

It is assumed that the maternal-fetal system is under quasi-static condition, i.e., the inertial effect is ignored. The governing equation is the Cauchy's equation of equilibrium

$$\text{div}\boldsymbol{\sigma} + \mathbf{b} = \mathbf{0} \qquad \text{or} \qquad \frac{\partial \sigma_{ij}}{\partial x_j} + b_i = 0 \tag{5.1}$$

satisfying the *natural* boundary conditions (applied traction force)

$$\boldsymbol{\sigma}\mathbf{n} = \bar{\mathbf{t}} \qquad \text{or} \qquad \sigma_{ij} n_j = \bar{t}_i \tag{5.2}$$

on boundary $\partial\Omega_\sigma$, the *essential* boundary conditions (prescribed displacement)

$$\mathbf{u} = \bar{\mathbf{u}} \qquad \text{or} \qquad u_i = \bar{u}_i \tag{5.3}$$

on boundary $\partial\Omega_u$, and the contact discontinuity condition

$$(\boldsymbol{\sigma}^+ - \boldsymbol{\sigma}^-)\mathbf{n} = 0 \qquad \text{or} \qquad (\sigma_{ij}^+ - \sigma_{ij}^-)n_j = 0 \tag{5.4}$$

along an interior contacting boundary $\partial\Omega_C$ where $x_i^+ = x_i^-$. Here, $\boldsymbol{\sigma}$ is the Cauchy stress tensor, $\mathbf{b}$ the body force per unit of current volume, $\bar{\mathbf{t}}$ the applied force per unit of current surface area, $\bar{\mathbf{u}}$ the prescribed displacement, $\mathbf{n}$ the unit vector normal to the boundary surface, and $\boldsymbol{\sigma}^+$ and $\boldsymbol{\sigma}^-$ represents the discontinuous stresses at the contacting point. To solve this boundary-value problem by finite element method, the following equivalent *weak form* of equilibrium equation is employed

$$\begin{aligned} \delta\Pi &= \int_\Omega \boldsymbol{\sigma} : \frac{\partial(\delta\mathbf{u})}{\partial\mathbf{x}} dv - \int_\Omega \mathbf{b}\cdot\delta\mathbf{u} dv - \int_{\partial\Omega} \bar{\mathbf{t}}\cdot\delta\mathbf{u} ds = 0 \\ \text{or} \quad \delta\Pi &= \int_\Omega \sigma_{ij}\frac{\partial(\delta x)_i}{\partial x_j} dv - \int_\Omega b_i(\delta x)_i dv - \int_{\partial\Omega} \bar{t}_i(\delta x)_i ds = 0 \end{aligned} \tag{5.5}$$

which is a statement of the principle of virtual work. Here, $\delta\mathbf{u}$ is the virtual displacement field which has to satisfy the essential condition. Note the natural condition is part of the weak form, and therefore automatically satisfied.

5.2.3 Pushing profiles

The total intrauterine pressure (IUP) acting on the fetus is the sum of the basal tone, the uterine contraction, and the woman's volitional pushing. Table 5.1 lists the characteristic IUP values used in this study, which were extracted from (*Buhimschi et al.*, 2004a).

The shape of the uterine contraction was reproduced based on clinical IUP recordings (one example is shown in Figure 5.2). The pixel values of points on the IUP curve were extracted from the recorded image using a Matlab code, then the obtained curve was scaled in two directions so that th characteristic IUP values listed in Table 5.1

Table 5.1: Characteristic intrauterine pressure values used in this study

Variable	Value
Duration of one uterine contraction (second)	101
Tone (mmHg)	20.8
Tone + Uterine contraction (mmHg)	64.5
Tone + Uterine contraction + pushing (mmHg)	95.9

were matched.

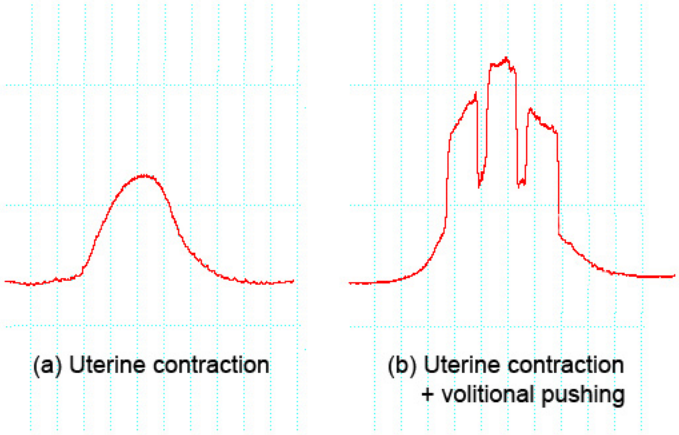

Figure 5.2: A sample trace of an intrauterine pressure (IUP) recorded under two conditions in the laboring room, kindly provided by Dr. Catalin S. Buhimschi (Yale University).

A logistic function was used to reproduce the 10-second wide volitional pushing profile

$$P(t) = \begin{cases} 0 & \text{if } t < c - w/2 \\ A\left(1 - \dfrac{1}{1 + [v(t - c + w/2)]^3}\right) & \text{if } c - w/2 \le t < c \\ A\left(1 - \dfrac{1}{1 + [v(-t + c + w/2)]^3}\right) & \text{if } c \le t \le c + w/2 \\ 0 & \text{if } t > c + w/2 \end{cases} \tag{5.6}$$

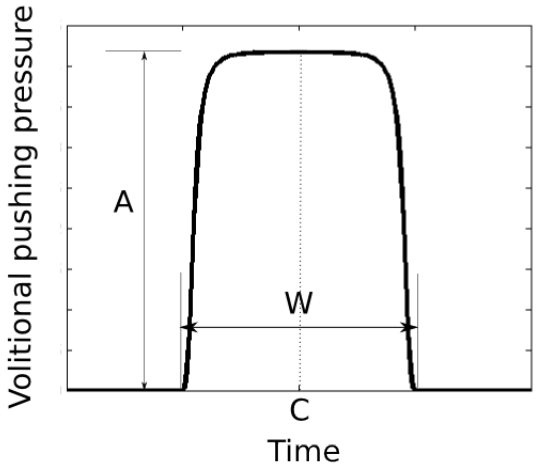

Figure 5.3: Generation of volitional pushing pulse using a logistic function, where the c, w, and A denote the location, width, and magnitude of the pushing pulse.

where P and t are pressure and time (Figure 5.3). The parameter values used here are $w = 10\,\text{seconds}$, $v = 2$, and $A = 95.9 - 64.5 = 31.4\,\text{mmHg}$.

The location of the pushing pulse, controlled by the value of c, can be before, during, and after the peak of the uterine contraction force. In this study, by combining the three basic locations, we investigated the efficacies of six pushing patterns defined by *Lien et al.* (2009): *Peak*, *Triple*, *Pre-Peak*, *Peak-Post*, *Pre*, and *Post* (Figure 5.4).

5.2.4 Boundary conditions

The free-body-diagram of the model is shown in Figure 5.5. The driving force to the fetal head (F_p) was computed by multiplying intraabdominal pressure by the effective pushing area of the fetal head. The location, direction, and magnitude of the resisting force from pelvic floor muscles (F_c) dynamically changed with the contact status. A damping drag force from surrounding uterine liquid and pelvic floor structures F_d was also included.

As the axisymmetric constraint, zero displacement along circumferential direction was prescribed for all nodes on the conical shell. To representing the muscular-bony

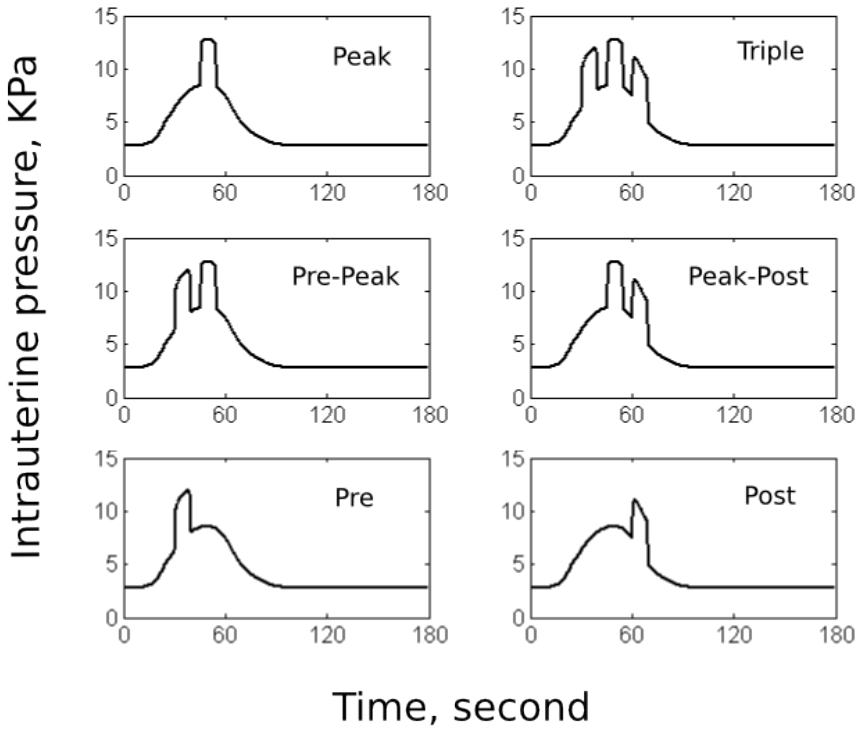

Figure 5.4: One cycle of intrauterine pressure (IUP), which is a superimposition of basal tone, uterine contraction, and volitional pushing. It is assumed that each cycle lasts 3 minutes. The interval between two consecutive pushes is set to 5 seconds, since this value makes the obtained shape of the triple IUP profile best matches Buhimschi's recordings.

connection, the cranial edge of the conical shell was set to be translationally fixed but rotationally free. The remaining part of the cone, including the distal edge, can freely extend axially to accommodate the passage of the fetal head.

The rigid sphere of the fetal head was allowed to move only along the axial direction, but was constrained on all other degree-of-freedoms (both translational and rotational). Cyclic intrauterine pressure was applied to drive the fetus forward. The surrounding uterine liquid and pelvic floor structure impose drag forces on the fetus, simulated by a linear damping dashpot

$$\boldsymbol{f}_d = -\eta \cdot \mathbf{v} \tag{5.7}$$

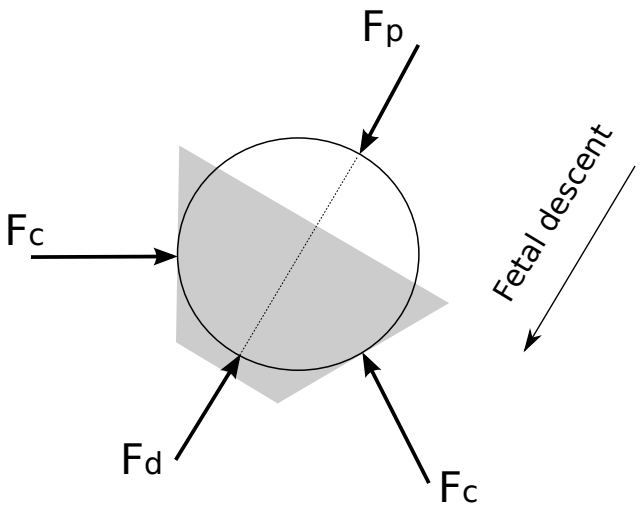

Figure 5.5: Free-body-diagram of the fetal head in the birth model. Here, F_p is pushing force due to intraabdominal pressure, F_c is the resisting force due to contact with the pelvic floor muscles, and F_d is the dragging force from surrounding uterine liquid and pelvic floor structures.

where $\boldsymbol{f}_d$ is the dragging force on the fetus, $\mathbf{v}$ is the velocity of the fetus, and η is the constant of damping coefficient. Here, the negative sign means that the drag force acts in the opposite direction as the moving fetus. Due to the complexity in the maternal-fetal interaction, it is impossible to measure the *in-vivo* value of η. For this reason, η was determined by *trial-and-error*. Specifically, different η values were tried with the triple-pushing simulation until the chosen value can lead to birth in 90 minutes, which is typically observed in the hospital at University of Michigan (DeLancey, personal communication). As long as the final value of η was determined, it is used as a standard value for simulations of all other pushing styles.

5.2.5 Material properties

For simplicity, the maternal pelvic floor muscle was assumed to be isotropic visco-hyperelastic. The three-parameter extended Mooney-Rivlin model was used to de-

scribe the nonlinear elastic property

$$W = C_{10}(I_1 - 3) + C_{01}(I_2 - 3) + C_{11}(I_1 - 3)(I_2 - 3) \tag{5.8}$$

As justified in Chapter VI (Section 4.2.1.3 on page 51), a Prony series with equal spectral strength and relaxation times spread one decade apart was used to approximate $G(t)$

$$G(t) = G_\infty + \frac{1 - G_\infty}{i_{max} - i_{min} + 1} \sum_{i=i_{min}}^{i_{max}} \exp\left(-\frac{t}{10^i}\right) \tag{5.9}$$

where $10^{i_{min}}$ and $10^{i_{max}}$ are short- and long-time constants, delimiting a span of linear transition from short to long relaxation. The values of the material parameters used in this study are derived from our experimental data on human pelvic floor muscle and perineal body, as described in Chapter IV.

5.2.6 Pushing efficacy index

An ideal pushing management strategy might aim to keep the duration of the second stage of labor (T) as short as possible; at the same time it requires as little maternal effort as possible, represented by the total number of volitional pushes (N). So, the efficacy of a pushing style is *inversely* proportional to the product $N \cdot T$. To measure how efficient a pushing strategy is with respect to the triple pushing style, a parameter, called efficacy index (EI), was defined as

$$\text{EI} = \frac{N_{tri} \cdot T_{tri}}{N \cdot T} \tag{5.10}$$

where N_{tri} and T_{tri} are the labor duration and the total number of volitional pushing number for the triple pushing style. The higher the EI value, the higher the pushing efficacy.

5.3 Results

The predicted descent of the fetal head in the triple pushing case is shown in Figure 5.6. The overall fetus motion exhibits a temporal sigmoid pattern, a result of the time-dependent nonlinear elastic property of the muscles. At beginning the fetal head descended rapidly because of the initial low muscle stiffness, but later its progress slows due to the increased resistance from the stretched and stiffening muscle. Near the end, especially after the maternal-fetal contacting region passes beyond the sphere's equator, the fetal descent accelerates until delivery. Even though the driving IUP magnitude is cyclically repeated, the amplitude of the fetal head forward stroke increases with time, resulting from the time-dependent muscle response in the form of *creep* deformation.

The distributions of the circumferential stress along the axial direction for three descent levels are also plotted in Figure 5.6. Integration of the circumferential stress along the axial direction gave us the stretching force that acts on the pelvic floor tissues (the shell elements for the tissue were assumed to be 1.0 mm in thickness). As can be seen, the largest stretching stress appears at the distal end of the muscle cone, and the stretching force increased with the descent of the fetal head.

The predicted muscle force resisting the fetal head progress is shown in Figure 5.7. Even though the muscles are stretched more and more with time, the resisting force on the fetus still decreases slowly with time, showing the time-dependent muscle response, this time in the form of stress *relaxation*.

Driven by the cyclic pushing IUP, the fetus exhibits oscillatory descent. The predicted history of the lowest descent point, corresponding to the peaks of the volitional pushing force, for all six pushing profiles are plotted in Figure 5.8. The estimated durations of the second stage of labor, the total numbers of volitional pushes, and the pushing efficacy index, are summarized in Table 5.2 and Figure 5.9. The predicted duration of labor (in minutes), and the total number of pushes for the Triple, Peak,

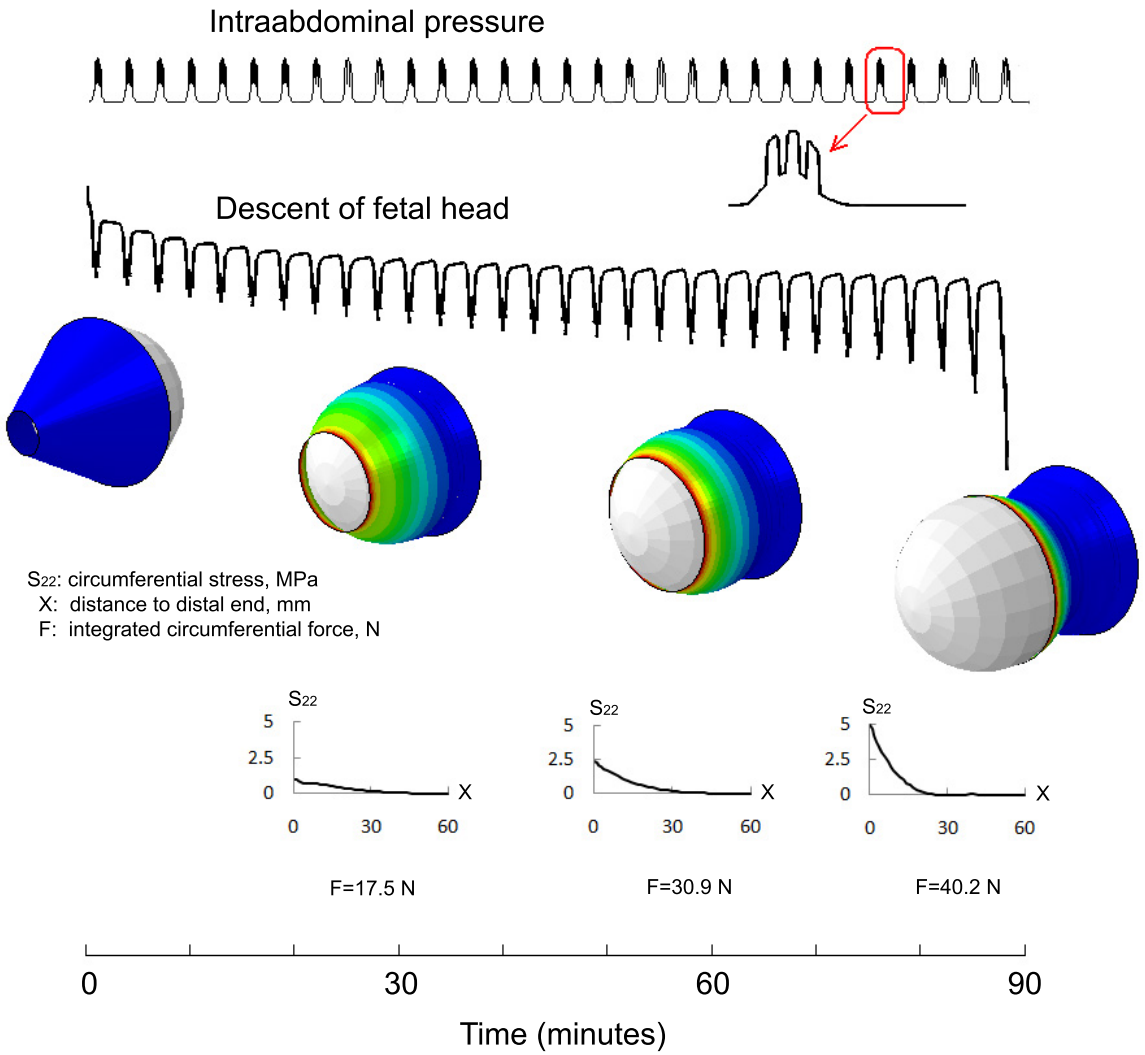

Figure 5.6: Predicted descent of fetal head for the triple pushing case. Also displayed are the corresponding triple-push IUP profile and the deformations of the conical structure. In each pushing cycle, the interval between two consecutive 10-second pushes is 5 seconds. The birth happened at the 30th pushing cycle, i.e., the duration of the second stage of labor was 90 minutes. The axial distribution of circumferential stress and the corresponding tension forces (by integration) at different descent locations are also displayed.

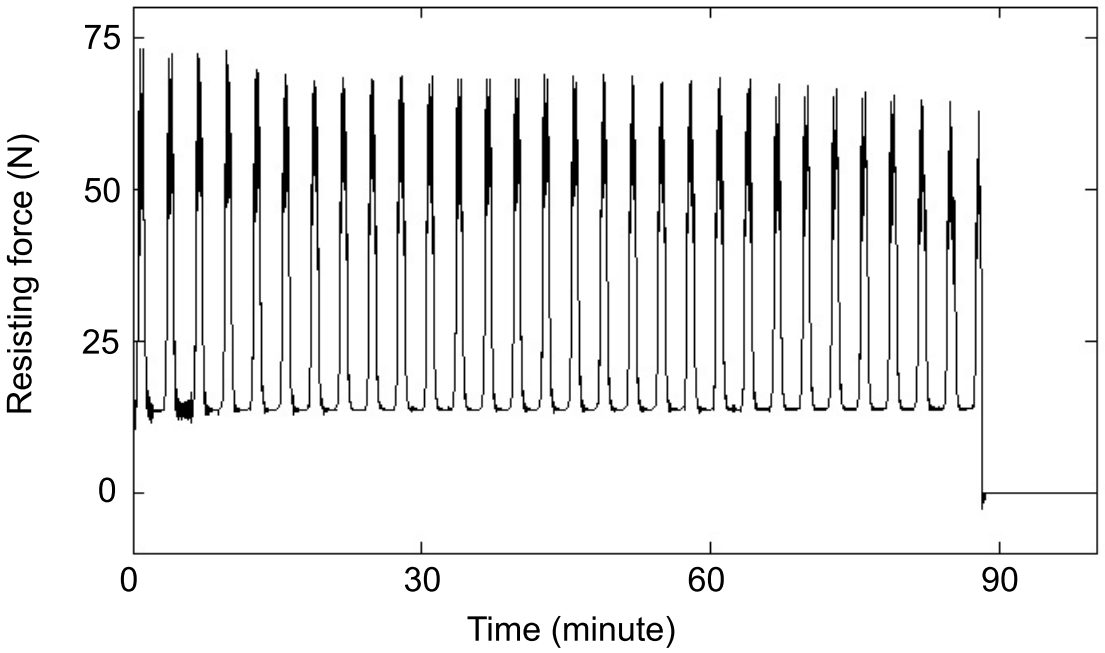

Figure 5.7: The change in predicted resistance force acting on the fetal head with time in the case of triple pushing.

Table 5.2: The efficacies of the six pushing profiles predicted by simulations

	Triple	Peak	Pre-Peak	Peak-Post	Pre	Post
Duration of the second stage of labor (minute)	90	138	108	108	171	174
Number of total volitional pushes	90	46	72	72	57	58
Efficacy index	1.00	1.28	1.04	1.04	0.83	0.80

Pre-Peak, Peak-Post, Pre and Post pushing styles were 90 and *90*, 18 and *46*, 108 and *72*, 108 and *72*, 171 and *57*, 171 and *58*, respectively. The single *Peak* push in one uterine contraction cycle has the highest efficacy index, 1.28, and the single off-centered push (*Pre* or *Post*) has the lowest EI value (around 0.8). Also, it can be seen that the *Pre-Peak* and *Peak-Post* (EI= 1.04) are slightly more efficient than the triple push ($EI = 1.0$).

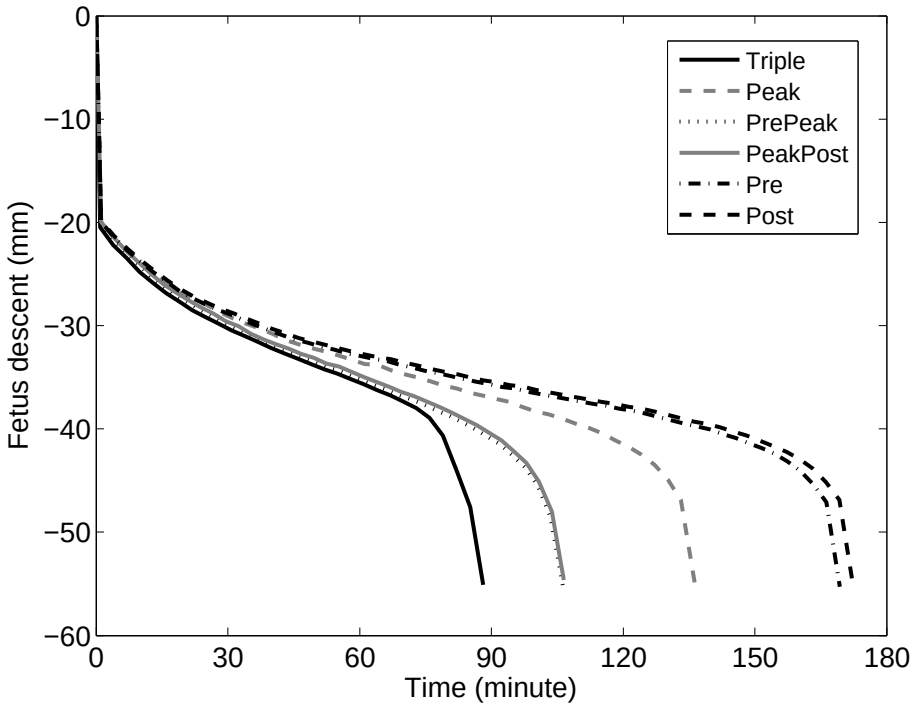

Figure 5.8: The predicted descents of the fetus for the six pushing styles

The sensitivity of the duration of the second stage of labor to variations in the triple pushing magnitude was examined, and the results are shown in Figure 5.10. As can be seen, the predicted labor duration was very sensitive to changes in pushing magnitude. For example, the labor duration increased by 27% when the pushing force decreased by 10%. When the pushing magnitude decreased beyond 25%, the model predicted that the fetus oscillated without further progress.

The sensitivity to pushing phase was also investigated using the *Pre-Peak* pushing profile. Specifically, the interval between the '*Pre*' and '*Peak*' pushes was adjusted to be 5, 10, 15, 20 and 25 seconds. The simulation results, shown in Figure 5.11, demonstrated that the predicted labor duration increased rapidly when the interval between two pushes increased. When the interval is larger than 25 seconds, the pre push is too far from the peak uterine contraction to meaningfully contribute to

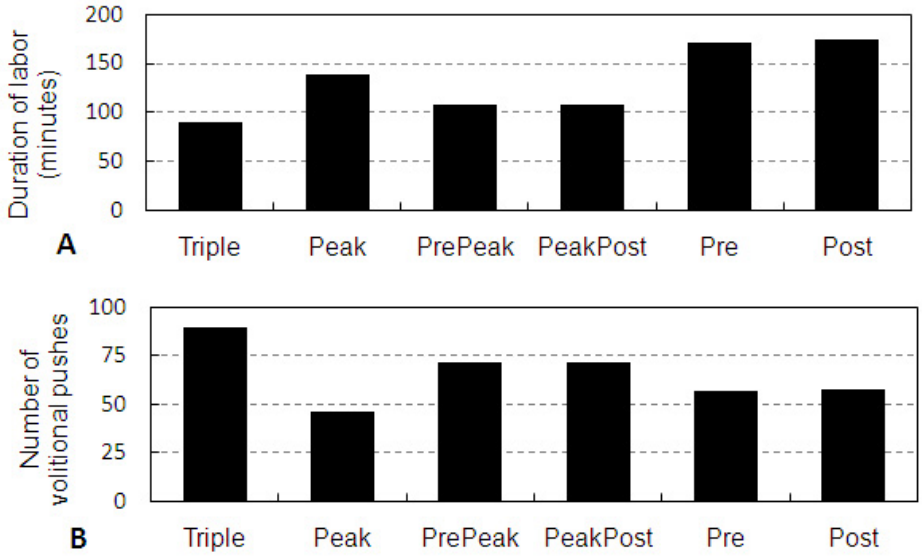

Figure 5.9: **A.** The predicted duration of the second stage of labor for different pushing styles. **B.** The total number of the volitional pushes by pushing style.

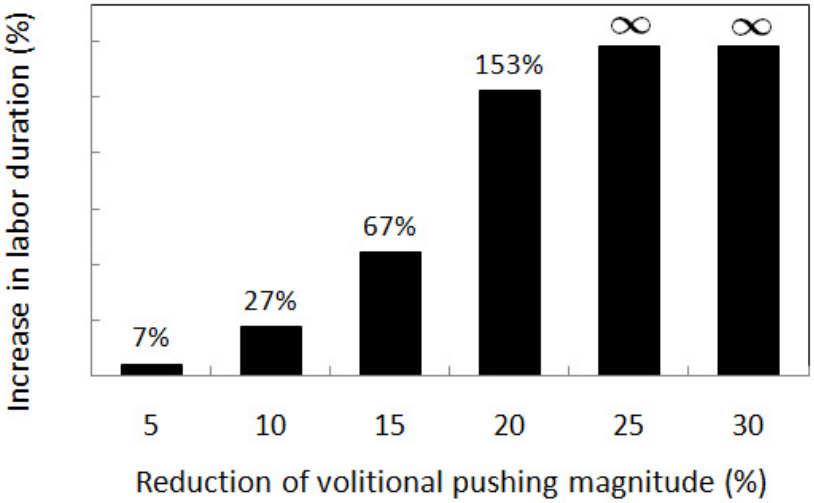

Figure 5.10: The predicted sensitivity of the duration of the second stage of labor to variations in the volitional pushing magnitude. The bars labelled with ∞ indicate that no continuous progress in fetus descent, i.e., no birth was predicted to happen. Calculations were based on the case of *triple* pushing profile.

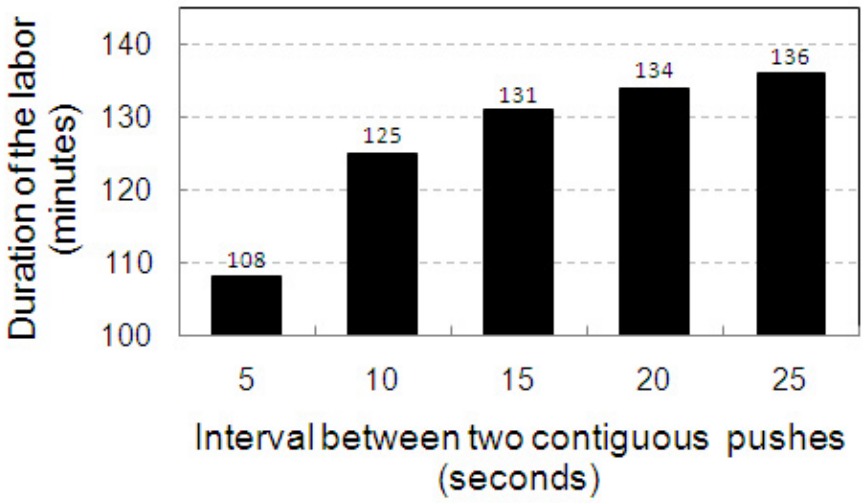

Figure 5.11: The predicted sensitivity of the duration of the second stage of labor to variations of the interval between two contiguous volitional pushes. Calculations were based on the case of *Pre-Peak* pushing profile, and the interval between the two volitional pushes was 5, 10, 15, 20 and 25 seconds.

the labor duration, i.e., the labor duration of the 'Pre-Peak' push increased to 136 minutes, almost the same as that of pure 'Peak' push, 138 minutes.

5.4 Discussion

Prolonged second stage of labor is strongly associated with increased risks of adverse maternal and perinatal outcomes, and high rate of operative delivery (*Moon et al.* 1990, *Menticoglou et al.* 1995, *Myles and Santolaya* 2003, *Cheng et al.* 2004, and *Altman and Lydon-Rochelle* 2006). The labor duration is affected by various obstetrical operational factors, and the physiological status of the pelvic floor structure of the woman. It is of practical significance to develop a theoretical model which can quantify the dependence of labor duration on these factors and therefore provides guides for obstetrical professionals. A pioneer model developed by *Lien et al.* (2009) studied how 6 different patterns of maternal effort might affect the progress during the second stage of labor. As an improvement over Lien's model, the model devel-

oped in this study provides a more general conceptual framework for modeling the energetics of the second stage of labor, by which a wide range of sensitivity analyses can be implemented, such as the effects of volitional pushing styles, muscle material properties, maternal fatigue, and operative delivery.

Using 3-D finite element method, our model is able to not only simulate dynamically changing maternal-fetal-interaction, but also incorporate more accurate constitutive law for pelvic floor muscles.

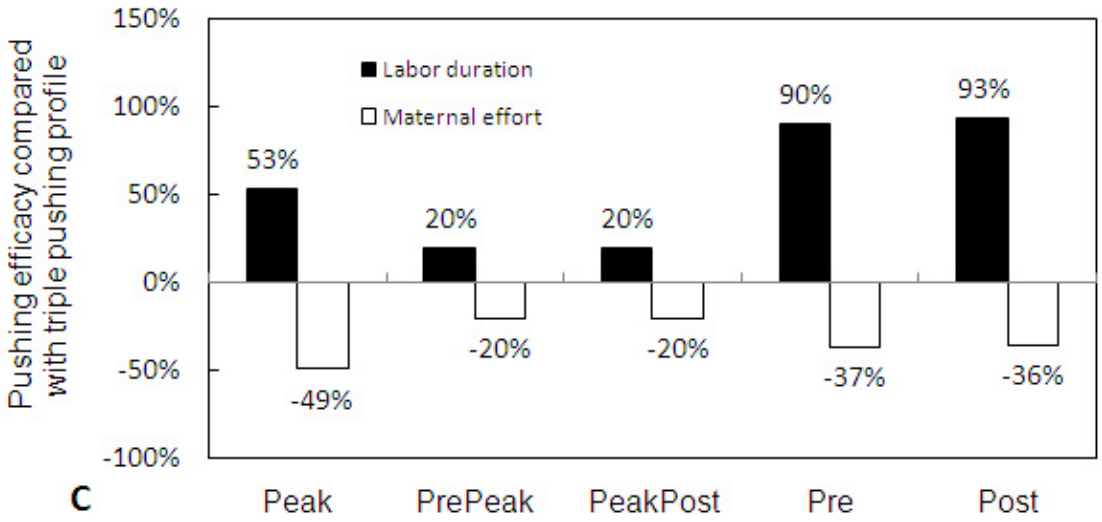

Figure 5.12: The relative changes of the labor duration and the number of volitional pushes, compared with the triple pushing profile.

Saving maternal effort by reducing the number of volitional pushes per uterine contraction is inevitably accompanied by increase of labor duration, as shown in Figure 5.12. By introducing the efficacy index (EI), the effect of changing the number of pushes per uterine contraction can be quantitatively compared. A same conclusion as that in *Lien et al.* (2009) is obtained that the centered single-push style, 'Peak', has the highest pushing efficiency (EI= 1.28), while the off-centered single-push styles, 'Pre' or 'Post', is lest efficient in making use of maternal effort ($EI = 0.8$).

Another important finding is that the labor duration is very sensitive to changes in the pushing magnitude. A nearly exponential relation between increase in labor

duration and reduction in pushing magnitude was observed in simulation results. When the pushing magnitude decreased by 25%, the model predicted failue of birth without operational delivery. The most important reason causing reduction in pushing magnitude is maternal fatigue, therefore it is important to improve caring during the second stage of labor to minimize maternal fatugue.

The third important finding is that the push timed at the peak of uterine contraction makes best use of maternal effort, and the pushing efficacy decayed fast when the push was timed away from the peak. Therefore, when there are more than one pushes in each uterine contraction, all pushes should be as close to the peak of uterine contraction as possible. However, the closer between two consecutive pushes, the easier for maternal fatigue to occur.

Due to the low descent rate of the fetal head, the second stage of labor can be viewed as a quasi-static process, i.e., the inertial effects of the system can be ignored. Ideally, this type of process should be solved by an implicit finite element solver, such as ABAQUS/Implicit. However, due to the relative low efficiency of ABAQUS/Implicit in modeling sophisticated contact problems, the explicit solver ABAQUS/Explicit was used in this study. In order to make sure the model was solved appropriately, the system kinematic energy (due to the inertial effect) and the strain energy (due to muscle stretching) are compared in Figure 5.13. As can be seen, the predicted kinetic energy was negligible, while the strain energy increases with the stretch of the muscle. Therefore, the simulation results solved by explicit solver are acceptible.

One limitation of this model is that maternal fatigue was neglected. For example, the simulation results show that increasing the volitional pushing magnitude, or decreasing the interval between two contiguous pushes, resulted in shorter labor duration. However, intuitively, these two cases should hasten maternal fatigue, and therefore should not necessarily shorten labor duration. The effect of maternal fatigue

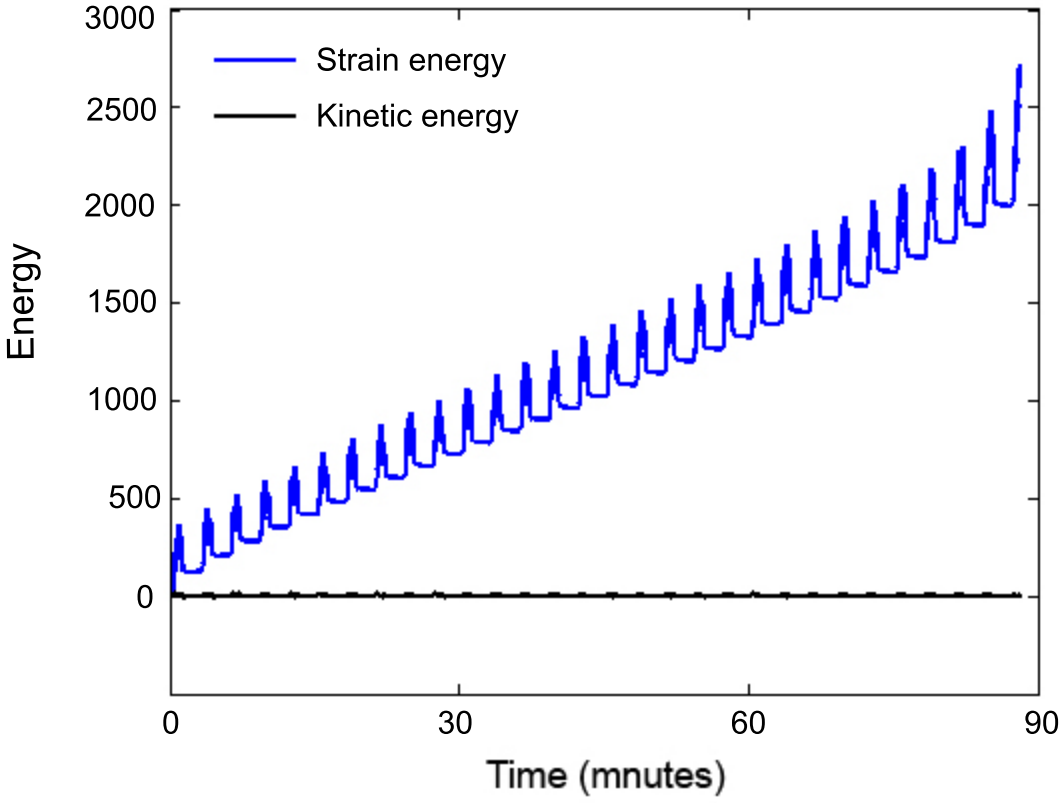

Figure 5.13: The predicted strain energy and kinematic energy, the former is accumulated due to muscle deformation, while the latter is due to the inertial effect.

is therefore explicitly explored in Chapter VIII.

Other limitations of the modeling approach include the gross simplification of the maternal anatomy, the fetal head morphology, and the assumption of a rigid fetal skull. While these simplifications affect the absolute values of muscle stress and strain, they should not affect the qualitative results from the model. In other words, a more detailed and anatomically accurate model will likely show similar trends to the effect of the dependent variables and covariates.

A further limitation includes the use of an isotropic material law to represent striated muscle. Striated muscle is known to be anisotropic, with a fiber oriented

along the circumferential direction, rendering it stiffer in that direction. The effect of muscle stiffness on the duration of the second stage of labor is explicitly addressed in Chapter VI.

CHAPTER VI

Effects of Levator Ani Muscle Viscoelastic Properties on the Duration of the Second Stage of Human Labor: A Sensitivity Study Using a 3-D Axisymmetric Finite Element Model

6.1 Introduction

During the second stage of labor, the fetal head is driven progressively through the pelvic canal, while the levator ani muscles undergoe a stretch ratio up to 3.2 (*Lien et al.*, 2004). This is a stretch ratio seldom reached by soft tissues without failure under non-pregnant states. Therefore, it is reasonable to believe that those muscles may undergo a remodeling process during pregnancy so as to become sufficiently flexible at term to facilitate passage of fetus.

From a biomechanics perspective, the mechanical properties of the pelvic floor muscles determine how these muscles deform when stretched by the fetal head. Soft tissue generally exhibit nonlinear elasticity under large deformation. Also, since the second stage of labor is a continuous and dynamic process lasting generally more than one hour, time-dependent responses also play important role in the mechanics of pelvic floor structure. The mechanical responses of soft tissues are typically biphasic, being

mixture of solid and fluid phases. The *solid-like* elastic property is controlled by the concentrations of collagen and elastin inside tissues, while the *fluid-like* viscous property is controlled by the water content of tissues.

Variations of mechanical properties at the macrostructural level during pregnancy is evidence of the remodeling process at the, as shown by studies on animal and human cervix (*Watanabe* 1988, *Buhimschi et al.* 2004a, *Owiny et al.* 1991, and *Conrad and Ueland* 1976). As an example, one study showed that softening of the mice cervix during pregnancy is a unique phase of the tissue remodeling process characterized by increased collagen solubility, maintenance of tissue strength, and upregulation of genes involved in mucosal protection (*Read et al.*, 2007). There is, however, currently a paucity of literature on changes of material properties of human and animal pelvic floor muscles induced by muscle remodeling during pregnancy.

In addition to tissue remodeling, other factors may also change the material properties of pelvic floor muscles, such as aging and hormonal influences. Aging is associated with significant changes of collagen in tissues leading to increased stiffness and rigidity (*Bailey et al.*, 1998). A recent study on pelvic floor tissues suggested that aging is associated with increased degradation of collagen (*Tinelli et al.*, 2009). Hormones can also change the mechanical properties of the maternal pelvic floor tissues. For example, a study on uterus, cervix, and vagina of rats showed that relaxin stimulated growth of these tissues by increasing water content and tissue mass (*Vasilenko and Mead*, 1987). According to this research, relaxin made alterations in the fluid matrix and proteoglycan metabolism rather than in collagen concentration. In another study on rat cervix (*Downing and Sherwood*, 1986), relaxin induced a decrease in collagen concentration and an increase in collagen solubility, therefore increasing the cervix extensibility. Another study on gilts suggested that relaxin increased the wet and dry weights, water content, and the glycosaminoglycan/collagen ratio between days 80-110 of gestation (*O'Day-Bowman et al.*, 1991). From these studies, we can

say that relaxin not only changes tissue elasticity, but also alters the time-dependent viscosity property.

Results from our tests on rat vagina and squirral monkey pelvic floor tissues demonstrated that pregnancy bring remarkable changes to both the stiffness and time-dependent behavior of those tissues (Chapter II and III). Although there is a paucity of literature on how the visco-elastic properties of human pelvic floor muscles change due to pregnancy, we hypothesize that similar changes occur in human tissues as those observed in animals. Thus, our primary hypothesis is that the duration of the second stage of labor is systematically affected by changes in pelvic floor tissue elasticity and viscosity.

6.2 Methods

The details of the 3-D axisymmetric finite element model for the second stage of labor, including the geometrical model, the time profile of the intrauterine pressure, and boundary conditions are given in Chapter V (Section 5.2 on page 64). Thus, only the mathematical formula for describing the viscoelastic properties of tissues, and the explanations of model parameters, are presented here.

The theory of quasi-linear viscoelasticity (OLV), proposed by Fung (*Fung*, 1972), was used to model the viscoelastic responses of the pelvic floor muscles, where the 2nd Piola-Kirchhoff stress at time t, $\mathbf{S}(t)$, is expressed in terms of a convolution integral of strain history $\mathbf{E}(t)$, and the reduced relation function $\mathbf{G}(t)$

$$\mathbf{S}(t) = \int_0^t \mathbf{G}(t-u) : \frac{\partial \mathbf{S}^e(\mathbf{E})}{\partial \mathbf{E}} : \frac{\partial \mathbf{E}(u)}{\partial u}\, du \tag{6.1}$$

where $\mathbf{S}^e$ is the instantaneous nonlinear elastic response (sometimes called *instantaneous stiffness*), which can be determined by the pseudo-strain energy function

W

$$\mathbf{S}^e = \frac{\partial W}{\partial \mathbf{E}}$$

The pelvic floor muscles were assumed to be isotropic hyper-elastic, and the three-parameter extended Mooney-Rivlin model was used to describe the nonlinear elastic response

$$W = C_{10}(I_1 - 3) + C_{01}(I_2 - 3) + C_{11}(I_1 - 3)(I_2 - 3) \tag{6.2}$$

where C_{10}, C_{01}, and C_{11} are material constants which were determined from our test data on female human levator ani and perineal body (Chapter IV). To study the sensitivity of the labor duration to the tissue stiffness, these three constants were adjusted proportionally to generate variations of instantaneous elastic response of the muscles.

It is assumed that tissue relaxation is the same in all directions, so the 4th-order tensor $\mathbf{G}(t)$ reduces to a scalar reduced relaxation function. The Prony series is widely used to approximate the reduced relaxation function $G(t)$. For example, a commonly used form is a two-term series

$$\begin{aligned} G(t) &= 1 - g_1 \cdot (1 - e^{-t/\tau_1}) - g_2 \cdot (1 - e^{-t/\tau_2}) \\ &= G_\infty + g_1\, e^{-t/\tau_1} + g_2\, e^{-t/\tau_2} \end{aligned} \tag{6.3}$$

where

$$G_\infty = \frac{\sigma_\infty}{\sigma_0} = 1 - g_1 - g_2 \tag{6.4}$$

is the long-term stress level normalized by the instantaneous stress. A typically observed relaxation behavior of soft tissue is that the hysteresis loop is relatively insensitive to strain rate over several decades of change, therefore there is a region of relatively constant slope in the $G(t)$ $\log(t)$ curve, transiting from short to long relaxation times. However, the equation (6.3) fails to reproduce the linear transition. This problem can be partially solved by increasing the number of series terms, but

that increases the number of model parameters, leading to curve-fitting instability. Another problem is that the parameters in (6.3) have overlapping contribution to relaxation. For example, the long-term stress level G_∞ is controlled by both g_1 and g_2, and the initial slope of relaxation is affected simultaneously by τ_1, g_1 and g_2. This makes it more difficult to carry out sensitivity analysis.

As described in Chapter VI (Section 4.2.1.3 on page 51), a Prony series with equal spectral strength and relaxation times spread one decade apart was used to approximate $G(t)$

$$G(t) = G_\infty + \frac{1 - G_\infty}{i_{max} - i_{min} + 1} \sum_{i=i_{min}}^{i_{max}} \exp\left(-\frac{t}{10^i}\right) \tag{6.5}$$

where $10^{i_{min}}$ and $10^{i_{max}}$ are short- and long-time constants, delimiting a span of linear transition from short to long relaxation. The advantage of using this discrete spectrum relaxation function is that only three parameters, G_∞, i_{min}, and i_{max} are involved, and each parameter has its own (i.e., non-overlapping) physical interpretations

- G_∞ affects how much stress remains after long-term time of relaxation;
- i_{min} affects the rate of the initial, i.e., short-term, relaxation;
- i_{max} affects how long it will take for the stress level to reach long-time equilibrium.

Knowing the general rule of how these parameters affect the relaxation process, we want to further know how sensitive the duration of the second stage of labor is to changes of these parameters. The sensitivity analyses were performed by adjusting one parameter while keeping other parameters fixed.

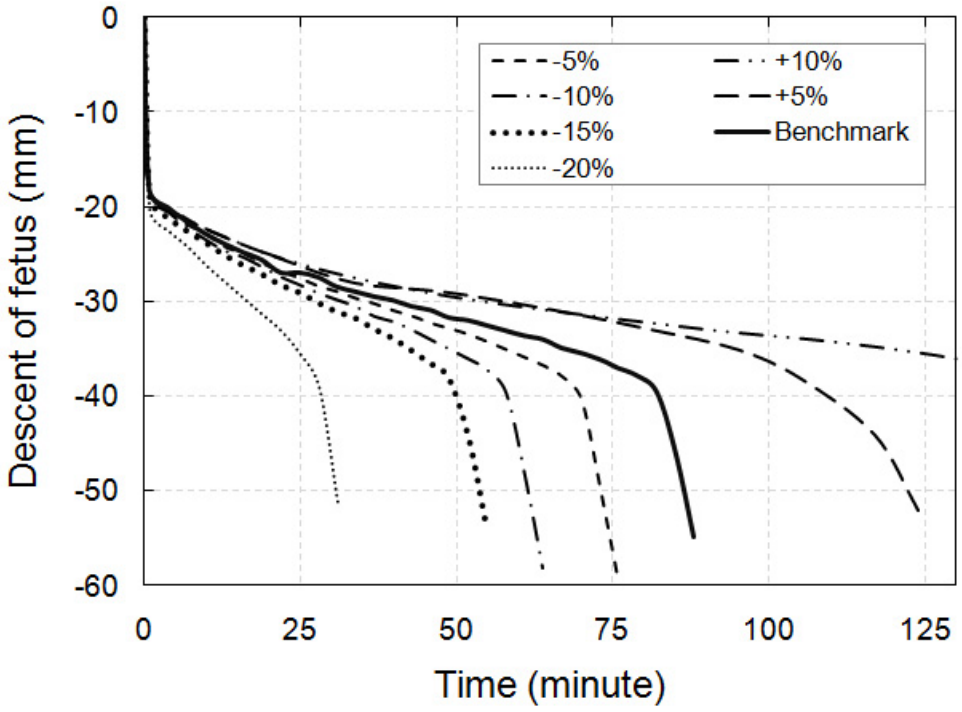

Figure 6.1: The predicted time history of fetus descent corresponding to relative changes of tissue stiffness. Here, '+' and '-' represent an increase and decrease of tissue stiffness, respectively.

6.3 Results

Tissue stiffness was adjusted by proportionally changing the values of C_{10}, C_{01}, and C_{11} in the strain energy. The predicted fetus descents and labor durations for different tissue stiffnesses are shwon in Figure 6.1 and Figure 6.2, respectively. Sensitivity analysis showed that the duration of the second stage of labor was more sensitive to increased stiffness than decreased stiffness. For example, decreasing pelvic floor stiffness by 5% and 10% shortened the labor duration by 16.7% and 30%; whereas increasing it by 5% and 10% increased the labor duration by 37.7% and 186.7%. Decreasing stiffness by 15% shortened labor duration by 40%, while increasing it by 15% led to oscillation of fetus movement without further progress.

The effects of short and long time relaxation on the duration of the second stage

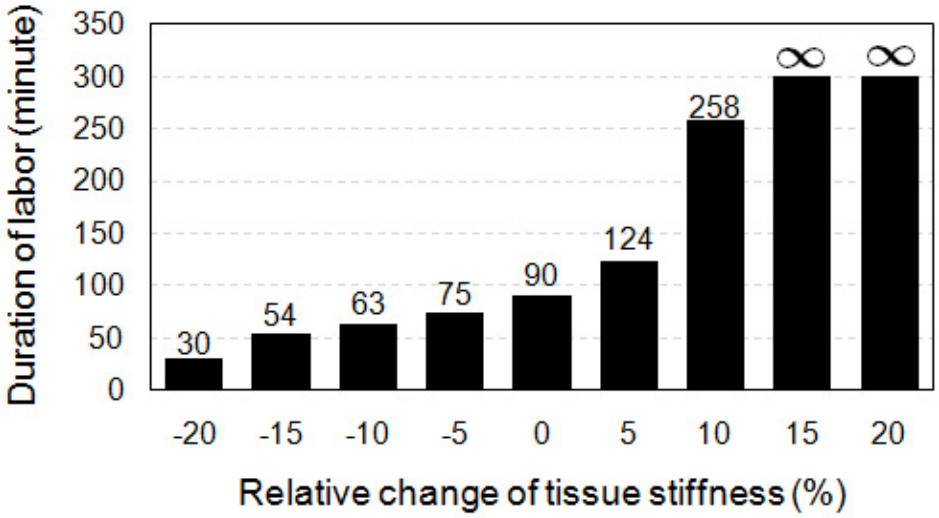

Figure 6.2: The predicted effect of different tissue stiffness on the duraton of the second stage of labor. The bars labelled with ∞ indicate no continuous progress of fetus descent.

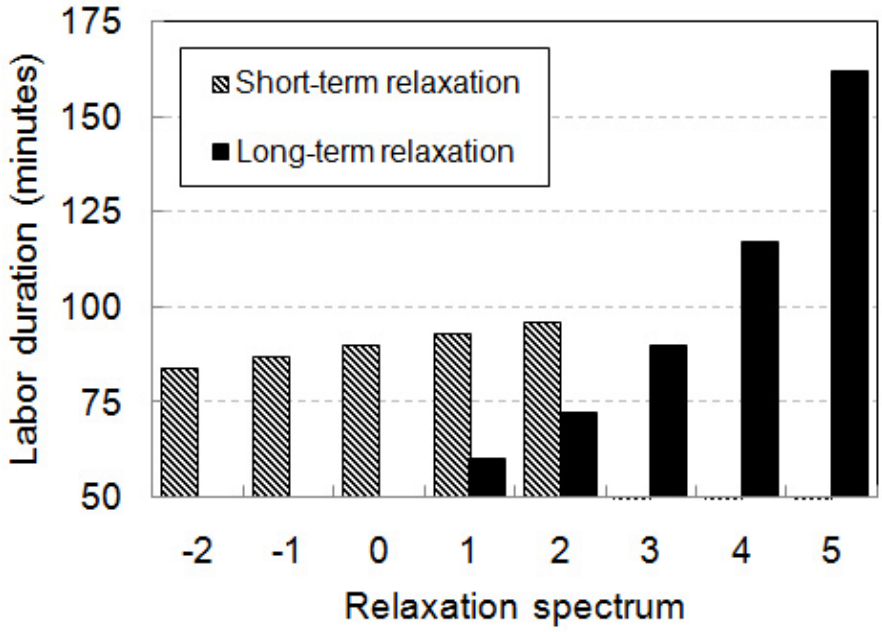

Figure 6.3: The predicted sensitivities of labor duration to changes of short- and long-term relaxation. The abscissa values represent the relaxation spectrum, i.e., value of i denotes the time of 10^i seconds.

of labor were investigated by changing the range of the constant slope region the relaxation spectrum, demarcated by $10^{i_{min}}$ and $10^{i_{max}}$. The benchmark simulation, calculated with $i_{min} = 0$ and $i_{max} = 3$, corresponded to 90-minute labor duration. Then, the sensitivity analyses were performed by systematically adjusting $i_{min} = -1, -2, 0, 1, 2$ while keeping $i_{max} = 3$, and adjusting $i_{max} = 1, 2, 3, 4, 5$ while keeping $i_{min} = 0$. The results are shown in Figure 6.3, from which it can be seen that

- The labor duration is more sensitive to the long-term relaxation than to the short-term relaxation. For example, when the short-term relaxation $10^{i_{min}}$ increased by two decades (10^0 to 10^2), the labor duration increased by 6.7%. However, same increase in the long-term relaxation i_{max} (from 10^3 to 10^5) led to an 80% increase of labor duration.

- The change of labor duration is almost *linearly* dependent on the change of i_{min}, but have strongly *nonlinear* dependence on the change of i_{max}.

- For long-term relaxation, the labor duration is more sensitive to increasing i_{max} than to decreasing it. For example, increasing i_{max} by two decades increased labor duration by 80%, while decreasing i_{max} by two decades decreased labor duration by 33%.

The effect of long-term residual stress level on the duration of the second stage of labor was analyzed by adjusting the value of G_∞ while keeping other parameters fixed. As shown in Figure 6.4, the labor duration was more sensitive to increasing G_∞ than to decreasing G_∞. For example, taking $G_\infty = 0.3$ as the reference, decreasing it by 17% and 33% shortened the labor duration by 16% and 29%, while increasing G_∞ by 17% and 33% increased the labor duration by 42% and 161%. Decreasing G_∞ by 50% shortened the labor duration by 39%, while increasing it by 50% led to stagnation of fetal progress.

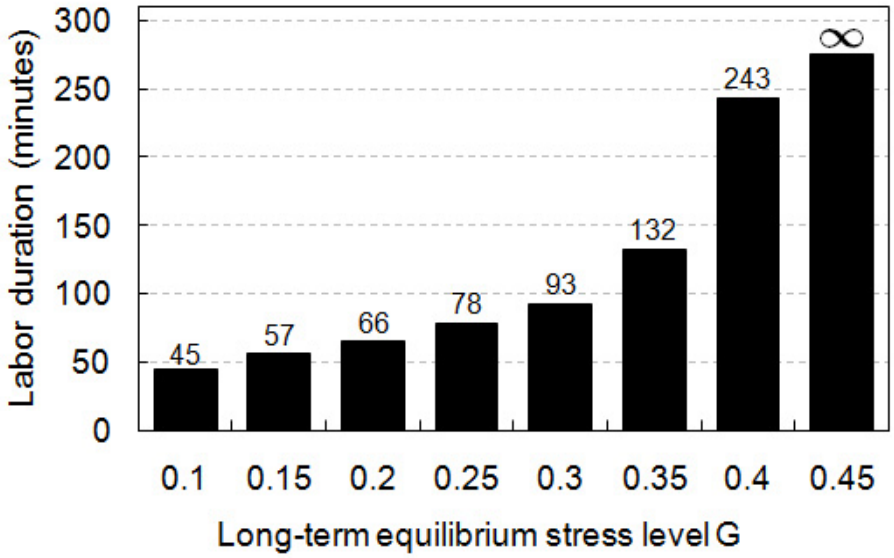

Figure 6.4: The calculated durations of the second stage of labor corresponding to different values of G_∞, the long-term equilibrium stress level normalized by initial instantaneous stress. The bar labelled with ∞ indicates that fetal progress was stagnated.

6.4 Discussion

The goal of this study was to shed light on how changes in material properties of the pelvic floor muscles affect the duration of the second stage of labor. The most important finding was that, for all visco-hyperelasticity material parameters investigated in this study, the duration of the second stage of labor is more sensitive to an increase than to a decrease in parameter values. Since increasing these parameters led to lengthening of labor duration, we can conclude that the duration of the second stage of labor is more sensitive to material property changes impeding labor progress than changes facilitating labor progress.

The intercept of the tangent line of $G(t)$ function at $t = 0$ with the abscissa, τ_0, can be calculated using following equation

$$-\frac{1}{\tau_0} = \frac{\partial G(t)}{\partial t}\Big|_{t=0} = -\frac{1 - G_\infty}{i_{max} - i_{min} + 1} \sum_{i=i_{min}}^{i_{max}} \frac{1}{10^i}$$

Also, denoting $\tau_{0.99}$ to be the time when 99% of total relaxation has happened, then we can use following equation to solve for $\tau_{0.99}$

$$(1-0.99)(1-G_\infty) = -\frac{1-G_\infty}{i_{max}-i_{min}+1}\sum_{i=i_{min}}^{i_{max}} \exp\left\{-\frac{\tau_{0.99}}{10^i}\right\}$$

Using the values of $i_{min}=0$, $i_{max}=3$, and $G_\infty = 0.28$, we can obtain

$$\tau_0 \approx 5 \text{ seconds}, \qquad \tau_{0.99} \approx 2016 \text{ seconds}$$

as shown in Figure 6.5.

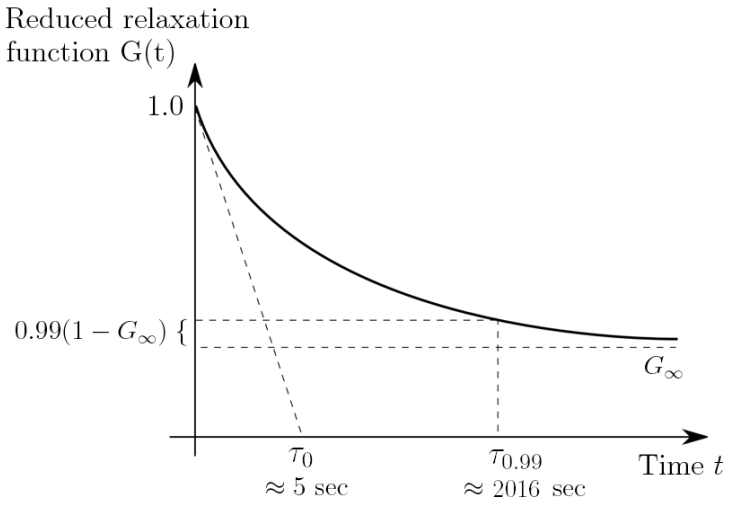

Figure 6.5: Schematic plot of the reduced relaxation function $G(t)$, with τ_0 and $\tau_{0.99}$ being calculated from typical values of relaxation parameters: $G_\infty = 0.28$, $i_{min} = 0$, and i_{max}=3.

During the second stage of labor, the temporal duration of each volitional push and uterine contraction are about 10 seconds and 100 seconds, respectively (*Buhimschi et al.*, 2004a). Therefore, when the pelvic floor muscles are stretched by the fetal head, the instantaneously induced peak stress drops so rapidly that the main resistance to fetal progression comes from already relaxed muscle stress. This explains why the labor duration is relatively insensitive to short-term relaxation(i_{min}).

Since a typical uterine contraction cycle lasts about 180 seconds, and completing 99% relaxation requires about 2016 seconds, we can conclude that muscle stresses are mainly determined by relaxation spectra of 10^1, 10^2, and 10^3 seconds. When i_{max} increases, stress relaxes more slowly and requires a longer time to reach long-term equilibrium, therefore labor duration is sensitive to an increase of i_{max}.

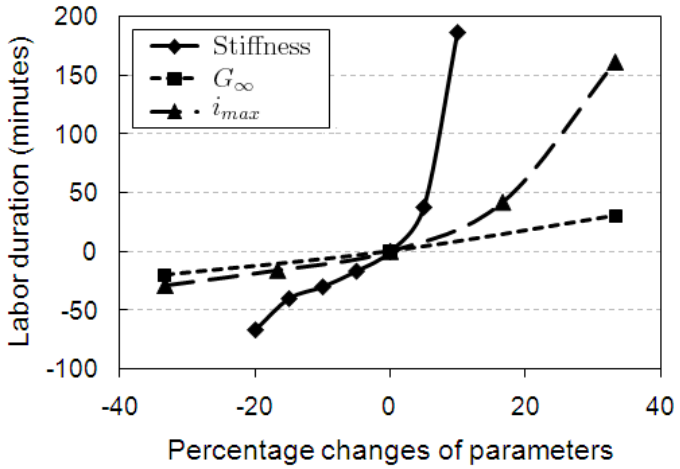

Figure 6.6: Comparison of effects of visco-hyperelasticity parameters on the duration of second stage of labor.

Another important finding is that, among the material parameters, the tissue stiffness has the most significant effect on the duration of the second stage of labor. As shown in Figure 6.6, where the effects of tissue stiffness, G_∞, and i_{max} were compared, the labor duration was most sensitive to tissue stiffness, and least sensitive to i_{max}.

One obvious limitation of this study is that the finite element model was based on simplified geometry, as discussed in Chapter V. Another limitation is that the muscle is assumed to be isotropic. From the study in Chapter II, anisotropy in material property induced by embedded muscle fiber has negligible effect on stress relaxation, but significantly affect the tissue stiffness. Therefore, anisotropy of material property should be included in our simulations. However, since the model used here is a geometrically simplified axisymmetrical cone, the benefit of including anisotropy is

not obvious. The effect of anisotropy is discussed in Chapter IX.

CHAPTER VII

Effects of Vacuum Extractor Usage on the Pelvic Floor Stress During The Second Stage of Labor: A Sensitivity Study Using a 3-D Axisymmetric Finite Element Model

7.1 Introduction

Operative vaginal deliveries refer to applying direct traction on the fetus head to complete the second stage of stage in short time. According to American College of Obstetricians and Gynecologists (*ACOG*, 2000), after the fetal head is engaged and the cervix is fully dilated, operative vaginal delivery should be considered when (1) there is a prolonged second stage of labor, i.e., lack of continuing progress for the time period prescribed by ACOG; (2) there is concern of immediate or potential fetal compromise, for example, non-reassuring fetal heart tones; (3) there is a need to shorten the second stage of labor for maternal benefit, for example, when the woman is exhausted.

A statistical study showed that the rate of operative vaginal delivery fell from 9.4% of live births in 1994 to 5.2% in 2004 (*Martin et al.*, 2007). Even though the rate of operative delivery is declining, vacuum is replacing forceps to become the

instrument of choice in the United States. In 2004, of all live births using operative delivery, vacuum comprised 79% while forceps comprised 21% (*Martin et al.*, 2007). The theoretical advantages of the vacuum extractor over forceps include (1) no need to insert space-occupying steel blades within the vagina; (2) less requirement in precise positioning over the fetal head; (3) No impinging on maternal soft tissues when rotating the fetal head. However, there is no definitive answer to the question which instrument, vacuum or forceps, is a better device in terms of maternal and fetal complications. Vacuum extraction causes significantly less maternal trauma than forceps delivery (*Vacca et al.* 1983, *Bofill et al.* 1996, *Johanson and Menon* 2000, *Wen et al.* 2001, and *Caughey et al.* 2005). On the other hand, it has also been shown that vacuum extraction carries higher neonatal risks then forceps (*Vacca et al.* 1983, *Bofill et al.* 1996, *Johanson and Menon* 2000, and *Demissie et al.* 2004). Also, detachment of vacuum cup can cause vacuum extraction to fail more than forceps delivery (*Johanson and Menon*, 2000). Despite these issues, vacuum extractor is rapidly replacing forceps to become the predominant instrument used in the second stage of labor, since the new designs of vacuum cups reduce the chance of cup 'pop-off' and the risk of injury to the infant (*Johanson et al.*, 1993). This chapter focuses on the biomechanical implications for the mother's pelvic floor muscles using the vacuum extractor; the effects on the fetal head are beyond the scope of this study. Therefore, in what follows, only the biomechanics of pelvic floor muscle and maternal complications associated with vacuum extraction are discussed.

A study on $50,210$ vaginal deliveries showed that the rates of third- and fourth-degree perineal lacerations were 1.7% for spontaneous vaginal delivery, but 9.3% for vaginal deliveries with vacuum extraction (*Angioli et al.*, 2000). Another study pointed out that a combination of episiotomy with vacuum extraction caused even higher risk of severe perineal laceration (*Kudish et al.*, 2006). Therefore, from the perspective of biomechanics, these tears in the tissues between the vagina and the anus

may be caused by excessive tissue tensile stress levels at the site of injury. Understanding how the different operational factors of vacuum extraction affect the stress development in the pelvic floor muscles is helpful for improving obstetrics care. The most important operational factors include the magnitude and the duration of force application during extraction.

Careful control of the vacuum extraction force is known to be important. One study showed that a vacuum traction force less than 11.5 kg was relatively safe for the infant and mother, while traction force exceeding 13.5 kg caused increased risks of maternal sphincter damage and fetal scalp injury (*Vacca*, 2006). Some authors suggested that 0.6 kg/cm^2 ($\approx$ 11.7 kg for a vacuum cup of 5 cm diameter) is the optimal peak vacuum pressure (*Lucas*, 1994). In the present study, a sensitivity analysis was performed to study how vacuum force level affects the stress development in the pelvic floor muscles.

It has been recommended that vacuum traction be intermittent and coordinated with the maternal expulsive efforts (*Cunningham et al.*, 2005), and it is believed that lowering the level of vacuum suction between contractions helps to decrease the rate of fetal scalp injury. However, there is another opinion that the vacuum force should be kept constant to prevent fetal loss of station during contractions and also to reach rapid delivery. One randomized controlled trial comparing intermittent suctioning with constant suctioning found no significant difference in time to delivery, method failure, maternal lacerations, episiotomy extension, incidence of cephalohematoma, and neonatal outcome (*Bofill et al.*, 1997). In the present study, we compared the predicted stresses in the maternal pelvic floor muscle induced by constant vacuum forceg until delivery, with intermittent vacuum force coordinated with maternal expulsive efforts.

The goal of this study, therefore, is to shed a light on the mechanism underlying the injury of perineal lacerations from the perspective of biomechanics. Sensitivity

analyses were performed to test the hypothesis that variations in operational factors of vacuum extractions markedly affect the stress status of the pelvic floor muscle during the second stage of labor.

7.2 Methods

7.2.1 Finite element model

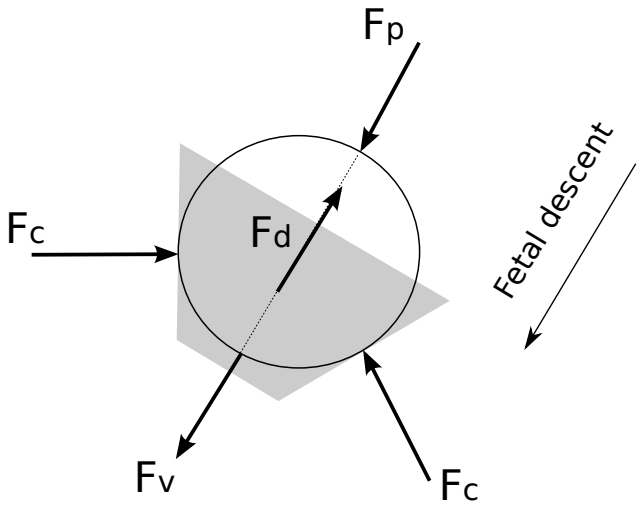

acuum

Figure 7.1: Free-body-diagram of the fetal head in the birth model. Here, F_p is pushing force due to intraabdominal pressure, F_c is the resisting force due to contact with the pelvic floor muscles, F_v is the vacuum force applying on the fetal head, and F_d is the dragging force from surrounding uterine liquid and pelvic floor structures.

The details of the 3-D axisymmetric finite element maternal pelvic floor model for the second stage of labor, including the geometry, time profile of the intrauterine pressure, and the boundary conditions are given in Chapter V (Section 5.2 on page 64). The free-body-diagram of the model is shown in Figure 7.1. The driving force to the fetal head (F_p) was computed by multiplying intraabdominal pressure by the effective pushing area of the fetal head. The location, direction, and magnitude of the resisting force from pelvic floor muscles (F_c) dynamically changed with the contact status.

The vacuum force applied on the fetal head F_v was computed by multiplying vacuum pressure with the area of vacuum cup. The vacuum force was fixed to be normal to the fetal head, and the variation application angle was neglected in this study. A damping drag force from surrounding uterine liquid and pelvic floor structures F_d was also included.

A simulation case predicting failure of spontaneous vaginal delivery (i.e., no continuous fetal progress) was used as the starting state for simulating vacuum extraction. Considering that maternal exhaustion is one of the main reasons leading to operative delivery, the starting situation for the vacuum extraction simulations was established by reducing the magnitude of the intrauterine pressure (IUP) by certain amount such that no continuous progress of fetal head was predicted and the fetal descent was still about half-way to crowning after 2 hours of the second stage of labor (Figure 7.2).

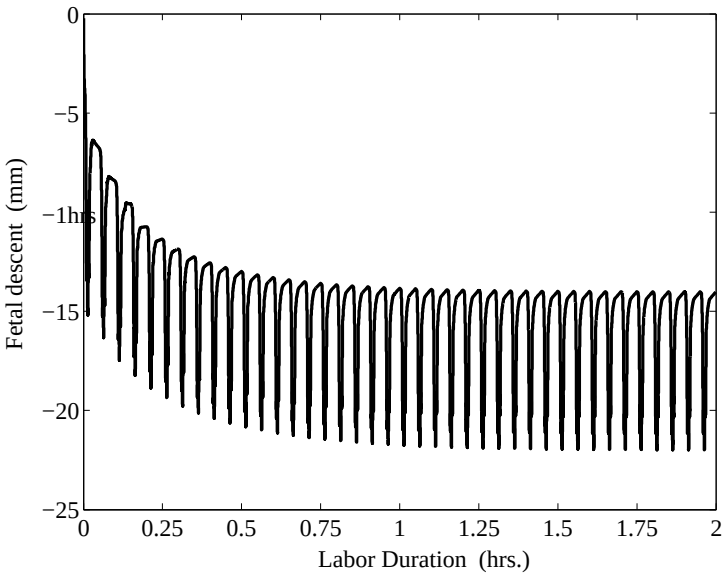

Figure 7.2: A simulated failure of spontaneous vaginal delivery, served as the starting point for modeling vacuum extraction. Here, the driving intrauterine pressure (IUP) was reduced so that, at the time of 2 hours, there is no longer continuous fetal progress and the fetal descent is about half-way to crowning.

7.2.2 Selection of vacuum extraction force

The selection of the vacuum extraction force magnitude in sensitivity analysis was based on literature data. One study suggested that the optimal peak vacuum pressure be 0.6 kg/cm^2 (*Lucas*, 1994); this corresponds to 58.8 KPa, 441 mmHg, or a vacuum force of 11.7 kg for a vacuum cup of 50 mm diameter. Another study on 119 attempted vacuum deliveries concluded that at least 80% of nulliparae and their infants may be delivered by vacuum extraction with relative safety if the traction force does not exceed 11.5 kg (*Vacca*, 2006). Therefore, the levels of vacuum extraction force simulated in this study were 8 kg, 10 kg, and 12 kg. All these pulling forces were applied fast (within 1 second). Statistical study on 119 vacuum assisted deliveries showed that the average duration of vacuum deliveries were $10 \sim 15$ minutes ($3 \sim 5$ pulls). Therefore, our simulations were limited to 15 minutes of applying vacuum extraction. If there was no prediction of delivery within 15 minutes, it was deemed as a failured vacuum delivery. The application of the vacuum extraction force (superimposed on the inrauterine pressure) began when uterine contraction began, and was maintained until delivery, if it occured. The timing of applying vacuum force with respect to one cycle of uterine contract is shown in Figure 7.3.

7.2.3 Duration of force application during vacuum extraction

Sensitivity analyses of two vacuum application patterns, continuous and intermittent, were performed. For the intermittent vacuum extraction, a vacuum pressure of 600 mmHg was used during volitional contractions and 100 mmHg were used between volitional contractions (*Bofill et al.*, 1997). Therefore, the constant force level in the continuous application and the high force level in the intermittent application were set to be 12 kg, while three forces, 2 kg, 4 kg, and 6 kg, were used for the low level in the intermittent application. The timing of intermittent vacuum pressure was set to coordinate with maternal effort, as shown in 7.4.

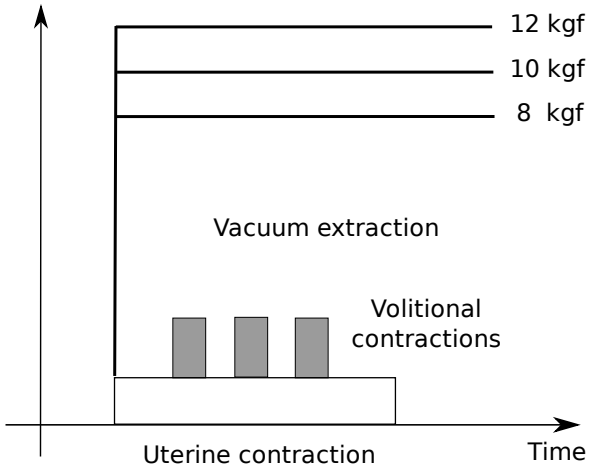

Figure 7.3: Schematic representation of the timing of vacuum extraction force with respect to the uterine contraction and volitional pushes.

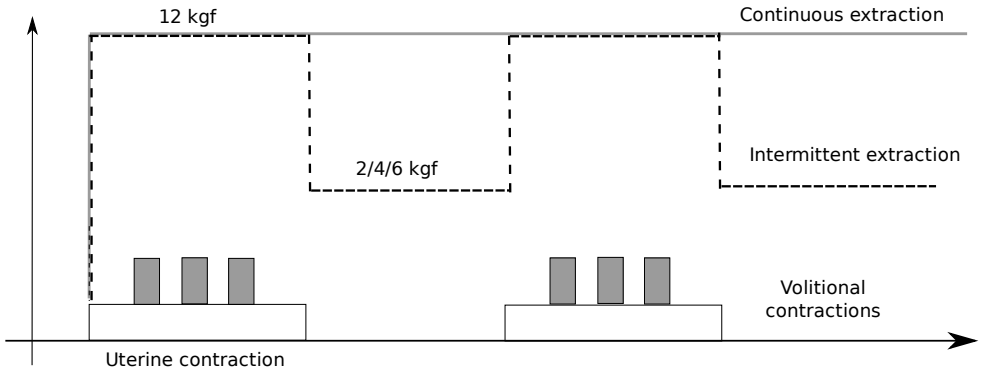

Figure 7.4: Schematic representation of two vacuum application patterns, continuous vs. intermittent.

7.3 Results

7.3.1 Level of vacuum extraction force

The sensitivity analyses were implemented to study how vacuum extraction level affects fetal descent, and levator muscle stress and stretch ratio at the distal end of the pelvic floor muscle. The predicted fetal descents during vacuum extraction for

vacuum forces of 8 kg, 10 kg, and 12 kg are shown in Figure 7.5. It was predicted that delivery happened at the times of 4.4 minutes and 9.6 minutes for 12 kg and 10 kg forces, respectively. However, for 8 kg vacuum force, no delivery within 15 minutes was predicted, meaning this vacuum level was insufficient for vacuum assisted delivery.

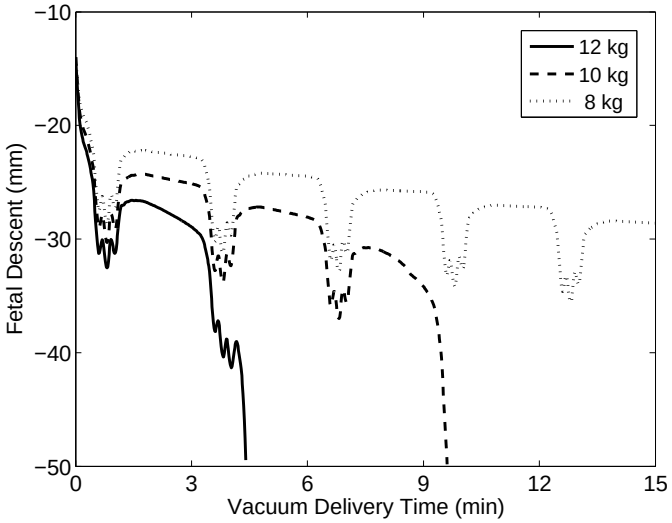

Figure 7.5: The predicted fetal descents during vacuum extraction for vacuum fextraction orces of 8 kg, 10 kg, and 12 kg.

The predicted time histories of the circumferential stresses (S_{22}) at the distal end of the pelvic floor muscle for different vacuum extraction forces are shown in Figure 7.6. As can be seen, for the 12 kg and 10 kg vacuum forces, the stress levels increased sharply near the end of the second stage of labor. The higher the vacuum extraction force, the higher the level of S_{22}, and also the faster the increase of stress level. For example, the stress level at fetal crowning for 12 kg is about 9.7 MPa, while that value for 10 kg is about 7.4 MPa.

The predicted time histories of the circumferential stretch ratios at the distal end of the pelvic floor muscle, for vacuum extraction forces of 8 kg, 10 kg, and 12 kg, are shown in Figure 7.7. The maximum stretch ratio almost reached 3.5 at the time of fetal crowning. Although the final maximum stretch ratios were at similar level, the

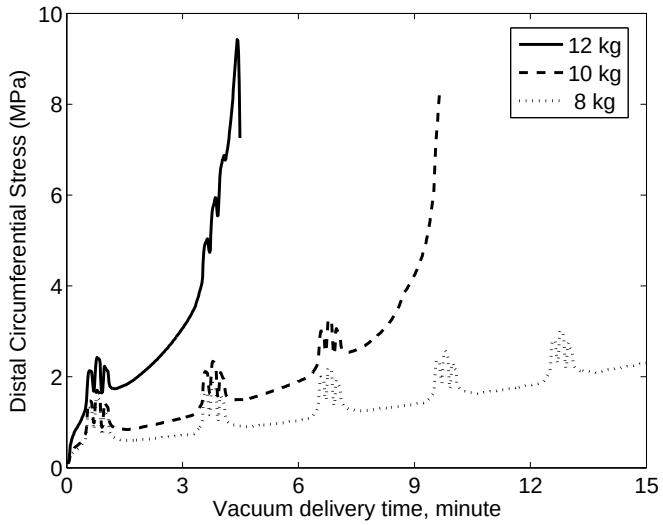

Figure 7.6: The predicted time history of the circumferential stresses at the distal end of the pelvic floor muscle, for vacuum extraction forces of 8 kg, 10 kg, and 12 kg.

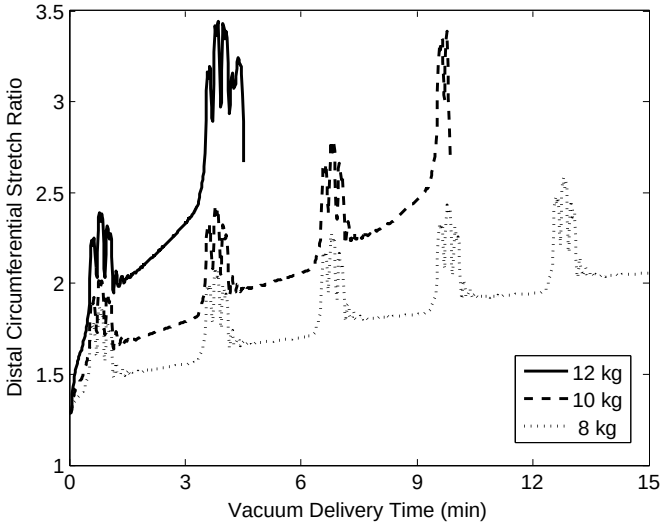

Figure 7.7: The predicted time history of the circumferential stretch ratios at the distal end of the pelvic floor muscle, for vacuum forces of 8 kg, 10 kg, and 12 kg. Same vacuum applying rate of 12 kg/min was used for all forces.

12 kg case had doubled average stretch rate that the 10 kg case had, due to its 50% shorter time to fetal crowning.

7.3.2 Force duration during vacuum extraction

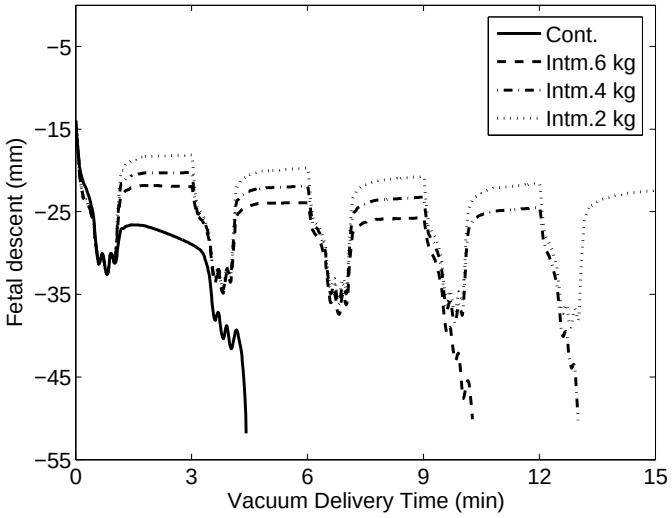

Figure 7.8: The predicted fetal descents among continuous and intermittent extractions. 12 kg vacuum force was used for the contraction extraction, while the intermittent vacuum forces switched between high (12 kg) and low (2/4/6 kg), coordinated with maternal effort.

The continuous and intermittent vacuum extractions were compared in terms of fetal descent, stress and stretch ratio at the distal end of the pelvic floor muscle. The predicted fetal descents during vacuum extraction are shown in Figure 7.8. Delivery were predicted to happen at the times of 4.4, 10.3 and 13 minutes for the 12 kg continuous vacuum extraction, $12-6$ kg, and $12-4$ kg intermittent extractions, respectively. For the $12-2$ kg intermittent extraction, no delivery was predicted within 15 minutes.

The predicted time history of the stresses (S_{22}) and stretch ratio in the circumferential direction at the distal end of the pelvic floor muscle are shown in Figure 7.9 and Figure 7.10 respectively. As can be seen, decreasing the vacuum extraction force between maternal efforts remarkably reduced the stress and stretch levels.

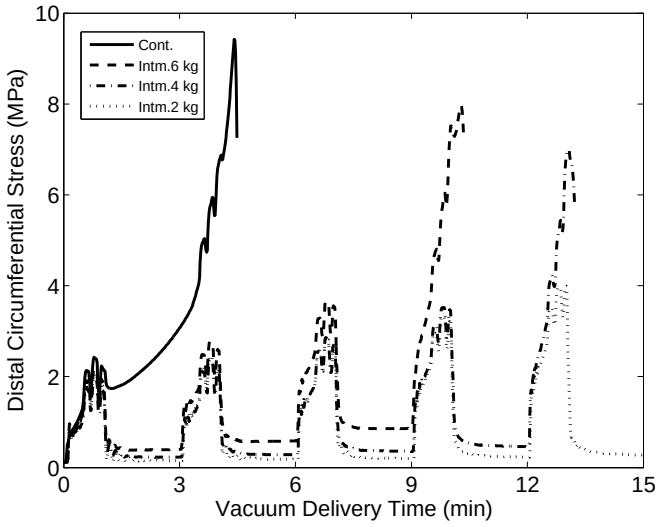

Figure 7.9: Comparison of the predicted time histories of the circumferential stresses at the distal end of the pelvic floor muscle, between continuous and three intermittent vacuum extractions. 12 kg vacuum force was used for the contraction extraction, while the intermittent vacuum forces switched between high (12 kg) and low (2/4/6 kg), coordinated with maternal effort.

7.4 Discussion

The goal of this study was to analyze how the different operational factors of vacuum extraction affect the stress and strain statuses in the pelvic floor muscles. In this way, biomechanics should help shed light on the mechanism underlying maternal muscle injuries, such as perineal lacerations, induced by vacuum delivery. To our knowledge, this work is the first computer model aiming to quantitatively analyze the biomechanics of operational delivery using vacuum extraction.

Some biomechanical models of muscle strain injury suggested that muscle strain correlates most with risk of muscle strain injury in vivo (*Lieber and Fridén* 1993, *Garrett* 1996). Other studies showed that, in addition to muscle strain, other factors, such as muscle stress and strain rate, are also relevant to the risk of muscle injury (*Brooks et al.*, 1995, *Brooks and Faulkner*, 2001 *Orchard* 2002). In vacuum delivery,

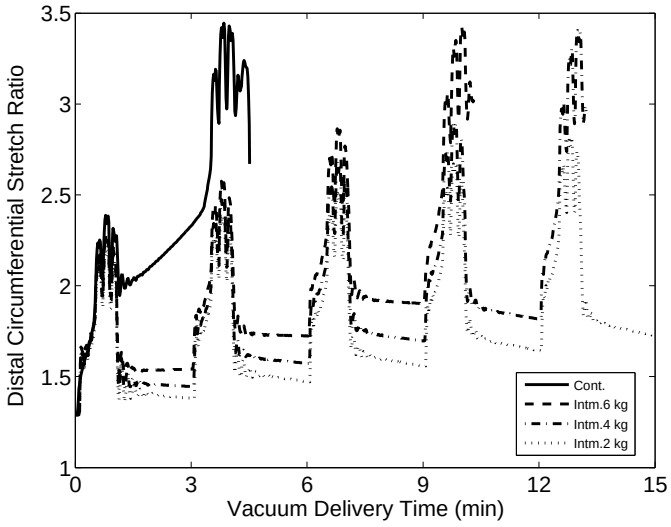

Figure 7.10: Comparison of the predicted time histories of the circumferential stretch ratios at the distal end of the pelvic floor muscle, between continuous and intermittent vacuum extractions. 12 kg vacuum force was used for the contraction extraction, while the intermittent vacuum force switched between 12 kg and 2 kg, coordinated with maternal effort.

the strain of the the pelvic floor muscle at the time of fetal head crowning are constant, depending on the size of fetal head. However, different patterns of vacuum extraction operations lead to different labor durations and muscle stretching modes, therefore the stress leval and strain rates in the pelvic floor muscle vary with different operational factors. Brooks found that the best predictor of injury in live passive muscle was the mechanical work done (*Brooks et al.*, 1995). Therefore, to quantify the risk of maternal muscle injury, we can define a parameter, called *risk of injury* (RI), as following

$$\mathrm{RI} = \frac{\int_0^{T_V} \sigma_{22}(t)\, d\epsilon_{22}(t)}{T_V} \tag{7.1}$$

where $\sigma_{22}(t)$ and $\epsilon_{22}(t)$ are the time histories of the distal circumferential stress and strain, T_V is the duration of the vacuum extraction delivery. The unit of RI is energy per unit volume per unit time. The higher the value of RI, the higher ther risk of

pelvic floor muscle injury.

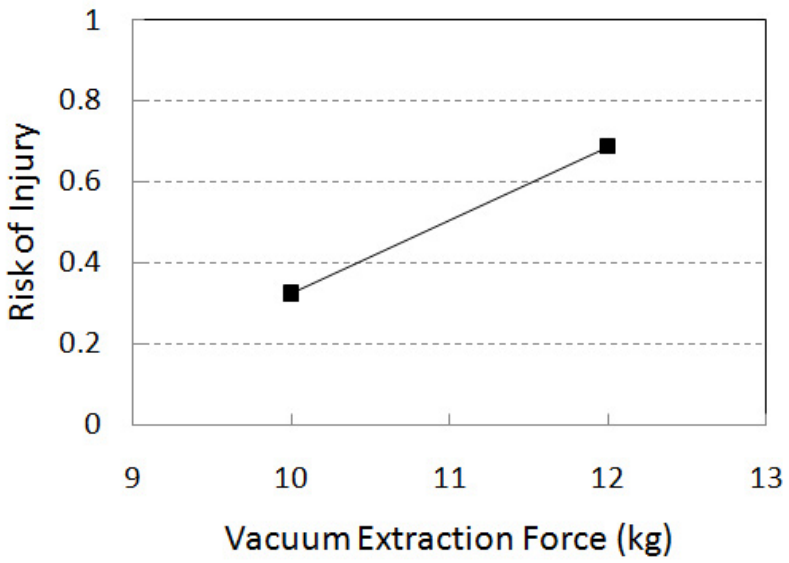

Figure 7.11: Comparison of the risk of pelvic floor muscle injury between the 10 kg and 12 kg vacuum extraction forces.

One important finding from this study is that the vacuum delivery duration, and the stress and strain in the pelvic floor muscle are very sensitive to the level of vacuum extraction force. Accordingly, the calculated risk of injury is also sensitive to vacuum extraction force, as shown in Figure 7.11. Here, since no prediction of vacuum delivery was predicted for the 8 kg force, it is excluded in comparison. As can be seen, when vacuum force increases by 25% (10 kg $\rightarrow$ 12 kg), the vacuum delivery duration decreased by 54% (9.6 min $\rightarrow$ 4.4 min). However, the risk of injury increases by 112% (0.3247 $\rightarrow$ 0.6875). This implies that, in absence of fetal compromise, increasing the vacuum extraction force may not be a good strategy for facilitating vacuum delivery, since the highly increased risk of muscle injury overweights the benefit of reduced delivery duration.

Another important finding from this study is that the risk of injury is also sensitive to the vacuum extraction pattern, as shown in Figure 7.12. Since no vacuum

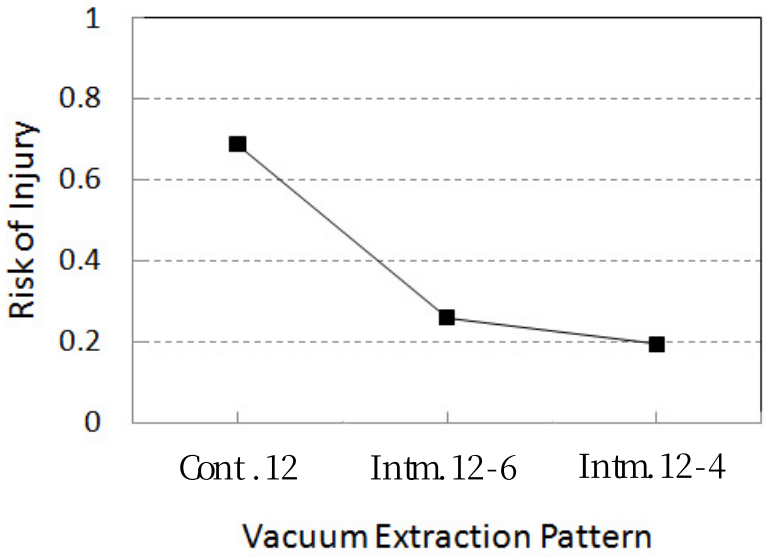

Figure 7.12: Comparison of the risk of pelvic floor muscle injury among different vacuum extraction patterns. Here, 'Cont.12' refers to continuous extraction with 12 kg force, while 'Intm.12-4/Intm.12-6' refer to intermittent extractions with high 12 kg force and low 4/6 kg force.

delivery was predicted for the intermittent extraction with $12 - 2$ kg, it is excluded in comparison. Compared with continuous extraction with RI=0.6875, reducing the vacuum extraction force during the interval between maternal efforts significantly reduced the risk of injury. For example, the risks of injury for the low forces of 6 kg and 4 kg were 0.2590 and 0.1934, corresponding to 62% and 72% reductions of RI with respect to continuous vacuum extraction. This result implies that moderate decrease of vacuum extraction force during the interval between maternal efforts is a nice strategy, since, compared with continuous extraction, it significantly reduces the risk of muscle injury but still helps to facilitate delivery. However, if the extraction force drops too much, it does not serve well for the purpose of completing delivery as soon as possible.

The main limitation in this study is that the effect of vacuum operation on fetus was neglected, and all judgements about the vacuum operational factors are based

solely on the materal outcome. However, fetal outcomes are also important factors to be considered when determining proper vacuum operation strategy. For example, no significant benefit of intermittent vacuum extraction was predicted by our model. However, it may be reasonable to reduce vacuum extraction force during the interval between maternal efforts to avoid fetal injury, which can not be predicted by this model.

The second limitation of this model is the gross simplification of the maternal anatomy. However, we believe that the qualitative results from this model are reasonable and similar to the results that could otherwise be obtained from more anatomically accurate model.

Finally, another limitation in this study is that the direction of vacuum extraction was neglected.

CHAPTER VIII

Effects of Maternal Muscle Fatigue on the Duration of the Second Stage of Human Labor: A Sensitivity Study Using a 3-D Axisymmetric Finite Element Model

8.1 Introduction

During the second stage of labor, the uterus contracts once every three minutes and each contraction lasts about one minute. To deliver her baby, a woman has to supplement the intrauterine expulsion pressure, under the guidance from obstetrical professionals, by strenuously contracting her diaphragm and abdominal wall muscles.

During laboring process, it is common for a woman to experience considerable psychological and physiological fatigue. The phychological fatigue is related with the emotional response of being in labor that typically lasts 90 minutes for a nullipara. Fear, anxiety, and the pelvic floor pain may cause the woman to be reluctant to 'exactly' follow instructions from obstetrical practitioners, thereby decreasing the effectiveness of volitional pushing. The psychological fatigue is beyond the scope of this study.

The physiological fatigue in the second stage of labor mainly comes from the

process of repetitively and strongly contracting the diaphragm and abdominal wall muscles. In a typical 'bearing down' effort, the woman inspires deeply and holds her breath, usually closing the glottis, thereby maintaining the diaphragm at a lower position; she then maximally contracts her abdominal wall muscles, and at the same time she tries to relax her pelvic floor muscle. This action increases the intra-abdominal pressure, helping to increase the expulsive force on the fetus. Muscle fatigue results from repetitive sustained contractions of the striated muscle fibers. A recently published explanation of local muscle fatigue is that, after extended high-intensity muscle contraction, small channels in the muscle cells begin to leak calcium, leading to weakened muscle contractions; this leaked calcium stimulates an enzyme that attacks muscle fibers and leads to fatigue (*Bellinger et al.*, 2008). This chapter focuses on modeling maternal muscle fatigue, integrating it into the finite element model of the second stage of labor that was developed in Chapter V, and then exercising that model in a sensitivity analysis.

There are many empirical studies on how maternal muscle fatigue develops during the second stage of stage, and how to optimize second stage nursing care to reduce maternal fatigue. For example, when compared with delayed pushing (allowing a rest before begining active pushing), immediate pushing (beginning active pushes at full cervix dilation) led to more frequent spontaneous deliveries(57.5% vs 52.7%) (*Fraser et al.*, 2000), decreased total active pushing time (58.16 min vs 75.77 min) (*Hansen et al.*, 2002), and a 31% reduction in midpelvic instrumented deliveries (*Roberts et al.*, 2004). The explanation for these observations was that delayed pushing reduces overall maternal fatigue. In addition to onset of active pushing, pushing duration (*Petersen and Besuner*, 1997), and pushing intensity (*Mayberry et al.*, 1999), also affect how much muscle fatigue develops during the second stage of labor.

Due to the empirical observations of the important influence of maternal muscle fatigue, it seems advisable to incorporate muscle fatigure in modeling the second stage

of labor. In this study, a dynamic fatigue model based on three muscle-activation states was combined with the energetics model of the second stage of labor (Chapter V). The combined model was then used to study how maternal muscle fatigue can affect the duration of the second stage of labor. The primary hypothesis that was tested is that maternal fatigue could significantly increase the duration of the second stage of labor.

8.2 Methods

8.2.1 Three-chamber fatigue model

The fatigue dynamics model used in this study is based on a motor unit (MU)-based model, originally proposed by *Liu et al.* (2002) and later extended by *Xia and Law* (2008). Some modifications were adopted so that the modeling approach fits the simulation of volitional pushing for our birth model.

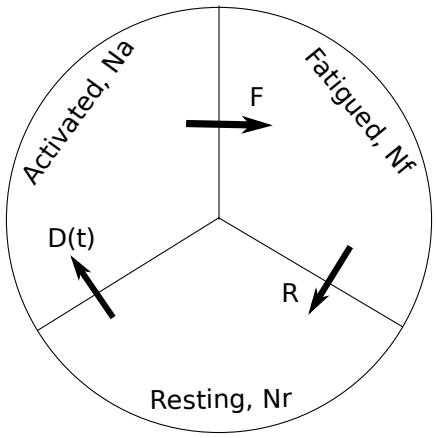

Figure 8.1: A three-chamber model for representing the dynamics of MU transition inside a MU pool, where N_a, N_f, and N_r are the percentages of activated, fatigued, and resting MUs with respect to the total MUs. Arrows between two chambers denote the transition directions, $D(t)$ is the muscle activation drive, and F and R are the fatigue and recovery rates, respectively.

The basic assumptions underlying this model include:

1. The MUs in a muscle are categorized according to their activation status: activated, fatigued, and resting. The incremental variation of activation level of each MU is neglected, so that each MU can generate either full tension (fully activated) or zero tension (resting/ideally fatigued).

2. The fatigue behaviour at the whole muscle level is controlled by the relative weights of these MUs. Specifically, the muscle force that can be generated by a group of MUs is proportional to the percentage of activated MUs.

3. Once an activated MU becomes fatigued, it has to undergo a recovery process to reach resting state, then it can be reactivated again. The transition among the three activation states is shown in Figure 8.1.

The three-chamber model was used to study the dynamics of transitions among the three activation states of MUs, as shown in Figure 8.1, where the arrows denote the permissible transition directions. The dynamics of MU transition can be expressed in following balance equation

$$\boxed{\text{Rate change of MU}} = \boxed{\text{Influx}} - \boxed{\text{Outflux}}$$

Denoting N_a, N_f, and N_r the percentages of activated, fatigued, and resting MUs in a MU pool, then the dynamics of these quantities are governed by differential equations

$$\frac{dN_a}{dt} = D(t) - F \cdot N_a \tag{8.1a}$$

$$\frac{dN_f}{dt} = F \cdot N_a - R \cdot N_f \tag{8.1b}$$

$$N_a + N_f + N_r = 1 \tag{8.1c}$$

where F and R are coefficients for controlling the rates of fatigue and recovery. The

time-varying function $D(t)$ represents the muscle activation drive, which depends on whether the target load (T_L) is reached and/or how many resting MUs (N_R) are available. Specifically

$$D(t) = \begin{cases} k_D \cdot \min\{T_L(t) - N_a(t), N_r(t)\} & \text{if } N_a < T_L \\ k_R \cdot (T_L - N_a) & \text{if } N_a \geq T_L \end{cases} \tag{8.2}$$

where the constants k_D and k_R are the muscle force development factor and relaxation factor, respectively. Note, a unit-less measure of target load T_L is introduced here to simulate the volitional pushing force exerted by the woman during labor, coached by obstetrical practitioners. $T_L(t)$ is a continuous function over time t and ranges between 0 and 1, with $T_L = 1$ representing maximum volitional push and $T_L = 0$ representing complete rest. Therefore, different pushing styles can be readily simulated using time function $T_L(t)$, making it feasible to study how pushing styles affect the fatigue development and therefore the duration of labor.

The values of model parameters used in this study, listed in Table 8.1, are from *Xia and Law* (2008). The fatigue model is relatively insensitive to values of k_D and k_R, because the muscle force development and relaxation is considerably faster than muscle fatigue. Therefore, the values of k_D and k_R can be chosen relatively arbitrarily, as long as they are sufficiently large than F and R, but not too large so as to cause numerical instability when solving the differential equations.

Table 8.1: Parameters used in the muscle fatigue model

L_D	L_R	F	R
10	10	0.01	0.002

8.2.2 3-D axisymmetric finite element model

The details of the 3-D axisymmetric finite element model of the second stage of labor are described in Chapter V (Section 5.2 on page 64). When maternal muscle fatigue is ignored, as done in Chapter V, each volitional pushing profile was modeled with a logistic step function of constant magnitude (formula 5.6 on page 67). In this study, the finite element model and the maternal fatigue model were integrated together by prescribing the target loading function T_L, the fraction of the maximum volitional pushing pressure that the woman can exert, where

$$P(t) = T_L(t) \cdot P_{max} \tag{8.3}$$

So, T_L can be viewed as the descending motor command from the cortex, with $T_L = 1.0$ meaning the woman is trying her best to push, while $T_L = 0$ meaning she is resting between pushes.

Therefore, various volitional pushing styles can easily be simulated through T_L, such as changing the pushing magnitude, frequency, and phase. The output from the fatigue model, when multiplied by P_{max}, is the 'fatigued' pushing force that the woman can generate, and was applied as the boundary condition to the finite element model after superimposed on the uterine contraction and tone pressures.

8.3 Results

8.3.1 Fatigue behaviors of diffferent volitional pushing styles

As an example to demonstrate the capability of the model to predict muscle fatigue behavior, the predicted time course of muscle activation states for different levels of isometric loadings are plotted in Figure 8.2. When the muscle is fully contracted ($T_L = 1.0$), the generated muscle force begins to decay immediately (zero endurance

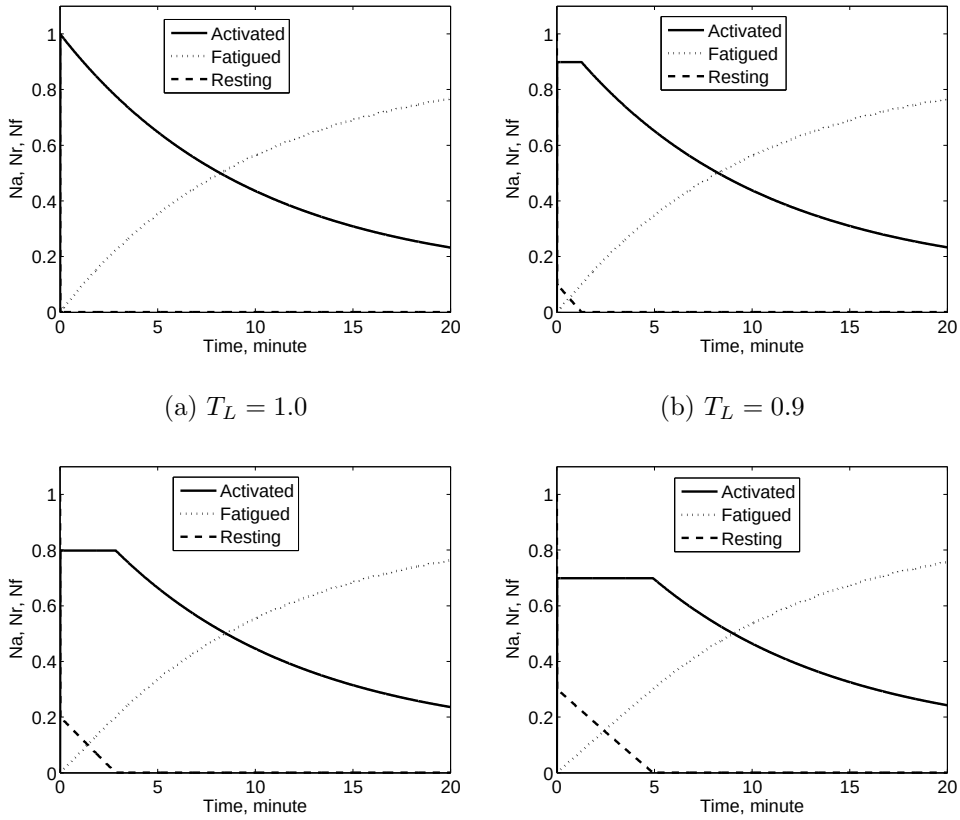

(a) $T_L = 1.0$ (b) $T_L = 0.9$

(c) $T_L = 0.8$ (d) $T_L = 0.7$

Figure 8.2: The predicted muscle activation states for four levels of isometric loadings: $T_L = 1.0$, 0.9, 0.8 and 0.7. For the activated state (solid line), the transition point from plateau to decay is the endurance time, where the muscle cannot maintain the targeted constant load.

time). However, when the muscle is partially contracted ($T_L < 1.0$), the generated force can be maintained at constant level for a while, and the endurance time increases with decreasing T_L.

Three pushing styles, *Triple*, *Pre-Peak*, and *Peak*, were chosen in this study for simulations with muscle fatigue being taken into consideration. The *Pre* and *Post* styles were neglected due to their low pushing efficiency. The *Peak-post* style was also neglected due to its similarity with the *Pre-Peak* style. In the fatigue model, the time-varying pressure pattern in each pushing style were simulated with the target loading

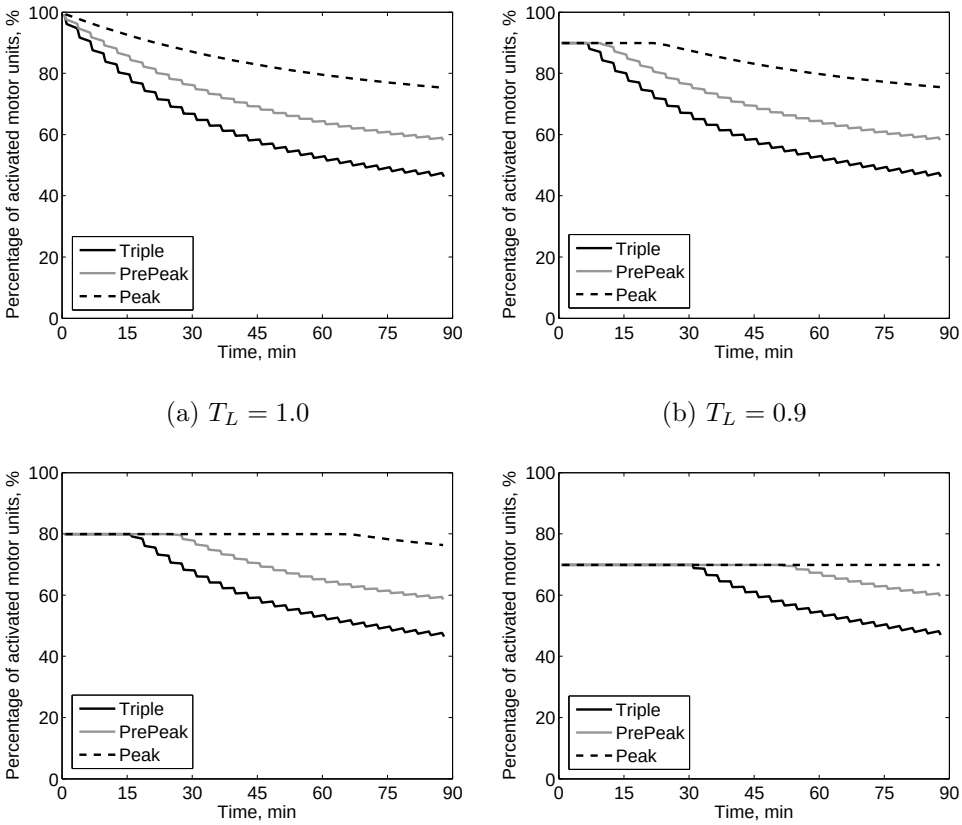

(a) $T_L = 1.0$ (b) $T_L = 0.9$

(c) $T_L = 0.8$ (d) $T_L = 0.7$

Figure 8.3: Predictions of the fatigue behaviors for the three volitional pushing styles with different levels of T_L. Here, the *Triple*, *PrePeak*, and *Peak* profiles refer to three, two, and one volitional push(es) in each 3-minute period of uterine contraction. The width of each push is 10 seconds, and the interval between two consecutive pushes is 5 seconds.

function $T_L(t)$. The predicted fatigue behaviors over 90-minute labor period of the three pushing styles are compared in Figure 8.3. It can be seen that the Triple pushing involved most fatigue while peak pushing has least fatigue. This result agrees with our intuition, since the more volitional pushes per uterine contraction, the more likely that the diaphragm and abdominal wall muscles become fatigued. The simulation result also showed that, no matter what pushing style, fatigue occurs immediately from the first push if the woman exerts full volitional pushes ($T_L = 1.0$). However, if the woman only pushes to a sub-maximal level ($T_L < 1.0$), the onset of fatigue

is delayed. The lower T_L, the later the fatigue begins. Also, the more pushes per uterine contraction, the earlier the fatigue begins. For example, when $T_L = 0.7$, fatigue does not occur for 90-minute Peak pushes, meaning the woman can maintain the pushing strength for the entire duration of a 90-minute labor. However, fatigue began at the time of 55 minutes for Pre-Peak pushes, and 35 minutes for triple pushes. This result agrees with an ergonomic study showing that the endurance of striated muscle performing repetitive contractions is inversely proportional to the duty cycle (*Iridiastadi and Nussbaum*, 2006).

Another interesting finding from Figure 8.3 is that even though the pushing magnitudes starts with different values of T_L, the final fatigued pushing magnitudes at the time of 90 minute are almost the same. For example, no matter what level the T_L is, the fatigued pushing magnitude of the Triple push is about 50% of the maximum push that the woman can exert at the time point of 90 minutes.

Mathematically, the maternal effort (ME) can be represented by the integration of the $P(t)$ curve over time. When fatigue is neglected, the calculated maternal effort is proportional to the number of pushes, since the pushing magnitude keeps constant for all pushes. However, when fatigue is taken into consideration, the calculated pushing magnitude decays with time. In this case, the maternal effort can be estimated by the integration of the $N_a(t)$ curve over time. Here, the maternal effort is unit free since N_a is unit-less, but it suffices for the purpose of comparison. The calculated total ME and ME per push, during 90-minute period, for Triple, PrePeak, and Peak profiles with $T_L = 1.0$ are listed in Table 8.2. Obviously, the value of ME per push can serve as a measure of pushing efficacy in an average perspective. Therefore, model prediction showed that the pushing efficacy of the Peak push is the highest, and the Triple push is the lowest. Intuitively this is reasonable, since the more pushes per uterine contraction, the more fatigue, and therefore the less the pushing efficacy.

In order to examine how the interval between two consecutive pushes affect the

Table 8.2: Comparison of maternal efforts (ME) over 90 minutes among the Triple, Pre-Peak, and Peak pushing styles, with fatigue being taken into consideration and $T_L = 1.0$. ME is unit free.

	Triple	Pre-Peak	Peak
Total ME	622.9	477.5	278.5
Number of pushes	90	60	30
ME per push	6.92	7.96	9.28

development of fatigue, simulations were run for the Pre-Peak pushing style with varying pushing intervals. The calculated fatigue curves coincided for all interval values, implying that the pushing interval has negligible effect on maternal muscle fatigue. At first, this result seems counterintuitive. However, for a 3-minute cycle of uterine contraction, the duty cycle (i.e., the fraction of pushing time) of the Pre-Peak pushing style is $\frac{2 \times 10}{3 \times 60} = \frac{1}{9}$; also, the two pushes are localized in the first 50 seconds within the 3-minute period, and changing the pushing phase does not affect the duty cycle. Therefore, it seems reasonable that changing the interval between the pre- and peak pushes has negligible effect on the overall fatigue behavior.

Since the pushing interval has almost no effect on maternal fatigue, it is natural to arrange pushes as close to the peak of uterine contraction as possible, so one viable pushing pattern is using one centered peak pushing with wider span of time. The predicted fatigue behavior of Peak pushing patterns having varying temporal width are shown in Figure 8.4. The results showed that the larger the pushing width, the more the muscle fatigue. Comparing with Figure 8.3, it can be seen that a 20-second-wide Peak push has the same fatigue curve as that of a 10-10-second Pre-Peak push with a 5-second pushing interval. Similarly, the fatigue of a 30-second Peak pushing is the same as that of a 10-10-10-second Triple pushing style with 5-second resting intervals. So, this is more evidence that the maternal fatigue is relatively insensitive to pushing interval.

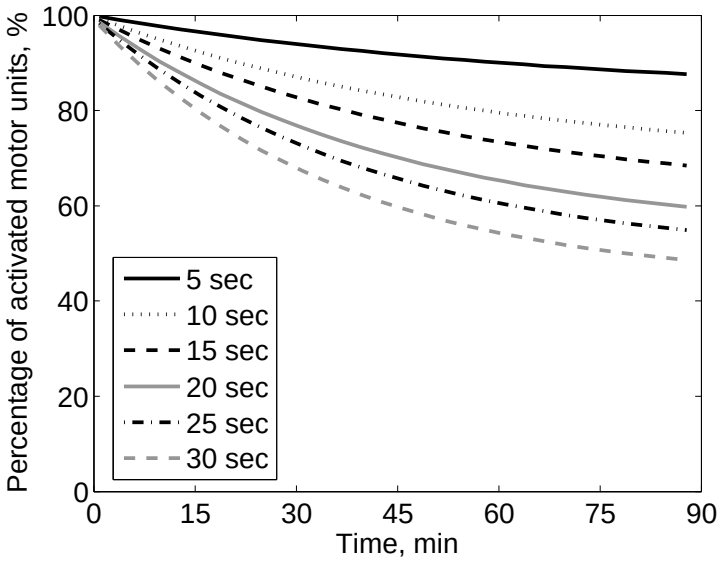

Figure 8.4: Predicted muscle fatigue for Peak pushing profile with varying pushing temporal width: 5, 10, 15, 20, 25, and 30 seconds. The pushing level was $T_L = 1.0$.

8.3.2 Sensitivity analyses of the effect of muscle fatigue on labor duration

The output from the fatigue dynamics model, N_a, was used to multiply the maximum volitional pushing pressure, and which was then superimposed on the uterine contraction pressure and muscle tone to form the boundary condition for the 3-D axisymmetric finite element model. Using the same approach as that used in Chapter V, a reference simulation case was established by choosing a damping coefficient by trial-and-error, so that predicted fetal head crowns at the time of 90 minutes under the triple pushing style with $T_L = 1.0$ (see Section 5.2.4 on page 68 for details).

Simulations for the Pre-Peak and Peak pushing styles of $T_L = 1.0$ were run, and the predicted labor duration and the number of volitional pushes were compared with those of the reference Triple case, as shown in Figure 8.5. The Pre-Peak style increased labor duration by 7% and reduced maternal effort by 29%, while the Peak style increased labor duration by 27% and reduced maternal effort by 58%. In Chapter V, simulations without considering muscle fatigue predicted that the Pre-Peak

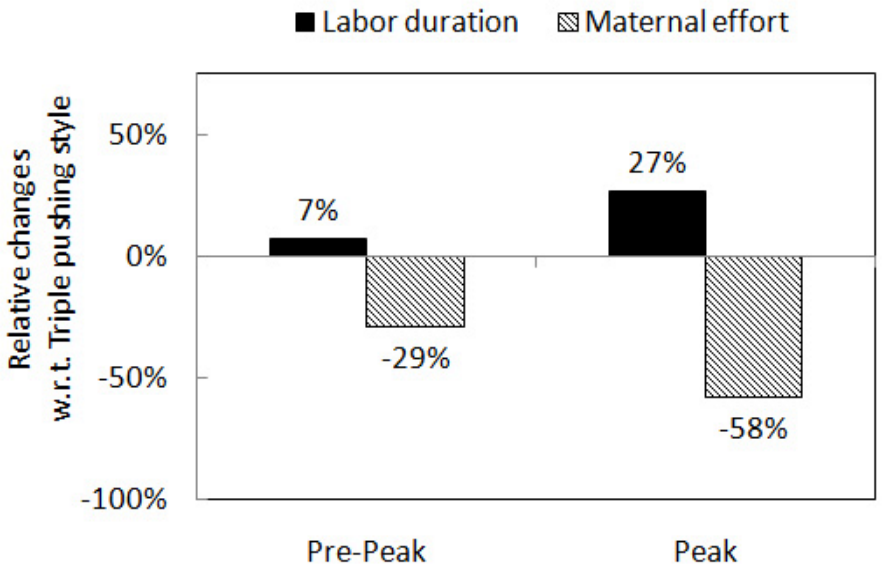

Figure 8.5: Relative change of labor duration and maternal effort of the *Pre-Peak* and *Peak* pushing styles, compared with *Triple* pushing style. The pushing magnitude was set to $T_L = 1.0$. The term 'w.r.t' denotes 'with respect to'.

style increased labor duration by 20% and decreased maternal effort by 20%, while the Peak style increased labor duration by 53% and reduced maternal effort by 49% (Figure 5.12 on page 78). Therefore, it can be concluded that without taking into consideration muscle fatigue, the lengthening of labor due to reducing the number of volitional pushing number per uterine contraction is overestimated. Indeed, reducing the pushing number, on one hand, tends to increase labor duration due to a smaller number of volitional pushes; on the other hand, fewer pushes means less muscle fatigue and therefore higher pushing magnitude, which tends to shorten labor duration. When muslce fatigue is ignored, the model disregards the second effect and therefore overestimates the effect of reducing the pushing number per uterine contraction on labor duration.

Simulations corresponding to different levels of T_L were run to see how sensitive the labor duration was to the volitional pushing magnitude, and the results are shown in

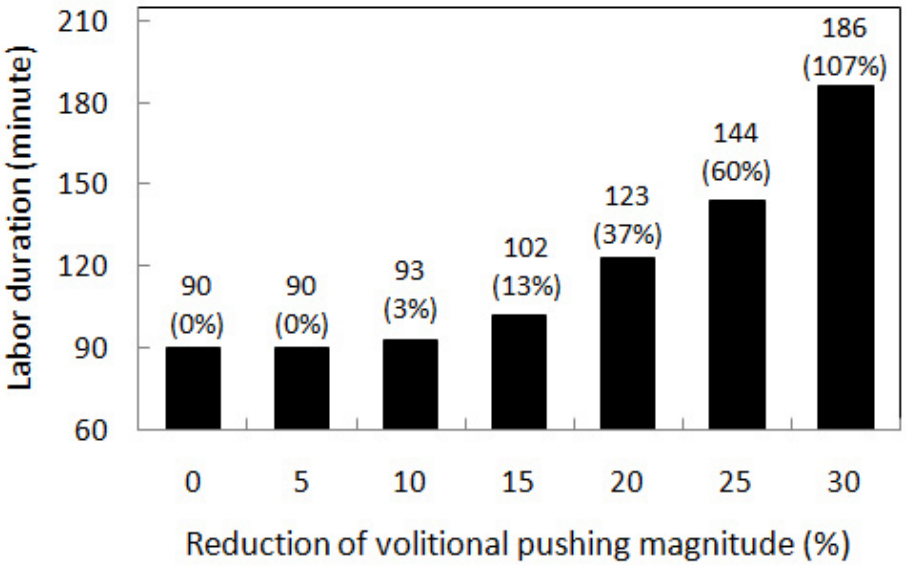

Figure 8.6: Predicted sensitivity of labor duration to volitional pushing magnitude. The simulations was run for the Triple pushing style. The percentages in parentheses are the relative change of labor duration compared with the reference $T_L = 1.0$.

Figure 8.6. It can be seen that for small changes in pushing magnitude, the increase in labor duration was not significant. For example, 5% reduction of pushing magnitude did not increase labor duration, and there was only a 3% increase in labor duration when the pushing magnitude was reduced by 10%. However, with a further decrease in pushing magnitude, the labor duration increased rapidly, doubling the labor duration for a 30% reduction of pushing magnitude.

As described in Chapter V, when maternal fatigue was excluded from the simulation, the predicted labor duration is very sensitive to changes in pushing intensity (see Figure 5.10 on page 76). For example, it was predicted that a 10% reduction in pushing magnitude led to a 27% increase of labor duration. Importantly, a 25% reduction in pushing magnitude led to failure to complete the second stage of labor: the fetal head never crowned. Therefore, when maternal fatigue is ignored, the model overestimates the sensitivity of labor duration to changes in pushing magnitude. This

is because it disregards the fact that lower pushing magnitude means less maternal fatigue, which has the effect of counteracting increase in labor duration.

8.4 Discussion

Ergonomic studies have shown that the fatigue behavior of striated muscles performing repetitive contractions depends on the muscle contraction level, the duty cycle, and the number of cycles (*Iridiastadi and Nussbaum*, 2006). During the second stage of labor, the woman is coached by obstetrical professionals to repetitively contract her diaphragm and abdominal wall muscles every three minutes for about $1 \sim 2$ hours. Different pushing patterns involve different muscle contraction levels and duty cycles. When the woman pushes repetitively, muscle fatigue and recovery interact and change dynamically with time. Due to this complexity we cannot,when modeling maternal muscle fatigue during the second stage of labor, manually (and arbitrarily) prescribe, *a priori*, the decay of pushing magnitude with model time.

To our knowledge, the model developed in this chapter is the first study incorporating the dynamics of muscle fatigue with the energetics of the second stage of labor. Instead of directly prescribing, *a priori*, a time-decaying pushing magnitude as the boundary condition to the finite element model, we introduced the target pushing function $T_L(t)$ as the model input, which physically represent the 'cognitive effort' of the woman, or perhaps the pushing instruction from obstetrical professionals. In this way, we are able to freely simulate various pushing styles that the woman is coached to follow, and the model 'internally' generates corresponding 'fatigued' pushing pressure as the boundary condition to the finite element model.

As described in previous section, the model ignoring maternal fatigue gave a biased prediction on how labor duration changes with respect to various pushing magnitude and the number of volitional pushes per uterine contraction. Incorporating the dynamics of maternal fatigue can effectively correct this bias and provide useful insights

for obstetrical professionals. For example, an important finding in this study is that a mild decrease in pushing magnitude did not lead to a significant increase in labor duration. Therefore, when the woman seems to be becoming fatigued, it is wise to coach her to exert a submaximal pushing intensity in order to save energy. We can consider the effect of pushing magnitude in another perspective. As shown in Figure 8.6, no matter what level of T_L, the 'fatigued' pushing pressure are almost at the same level near the end of the second stage of labor. This means that the contribution of high pushing pressures mainly go to advancing the early stage of fetal descent, but does not necessarily benefit the late second stage or final fetal crowning.

Another important insight from our sensitivity analyses is that when the number of volitional pushes per uterine contraction is reduced (Triple $\rightarrow$ Pre-Peak $\rightarrow$ Peak), the decrease of maternal effort outweighed the increase in labor duration (Figure 8.5). Therefore, the Peak pushing style is the most efficient pushing style in the sense that it not only makes best use of peak uterine contraction, but also incurs least maternal fatigue due to having the lowest duty cycle.

One interesting finding from the fatigue model is that maternal fatigue is insensitive to the interval between the pre- and peak- pushes in the Pre-Peak style. The direct implication from this finding is that all volitional pushes within one uterine contraction cycle should be timed as close to the peak uterine contraction as possible. Since pushing phase does not change the duty cycle, crowded pushes surrounding the peak of uterine contraction do not necessarily lead to more maternal fatigue. Considering that the Peak style is the most efficient pushing pattern, we could even use a 20 second- and a 30 second- wide Peak push to replace a 10-10-second Pre-Peak and a 10-10-10-second Triple push, respectively. Theoretically this is promising, but in practice this strategy may not be feasible. During each volitional push, the woman takes a deep inspiration and holds her breath in order to keep her diaphragm at a lower position. So, too long a single push may cause anoxia, which is harmful to the

fetus. Therefore, the best pushing style is to employ a single push timed at the peak of uterine contraction with optimal duration. If we need to increase the pushing duty cycle to facilitate the labor progress, we should not increase the number of volitional pushes per uterine contraction. Instead, we should use a single Peak pushing style with a longer duration, but not so long as to cause anoxia.

One limitation of this model is that the incremental variation of activation level of an individual motor unit is neglected, and only two discrete tension states, full or zero, were considered. So, the generated muscle force is proportional only to the relative weight of the activated motor units in full tension. The fatigue dynamics of individual MUs is beyond the scope of this model, but could be investigated in future work.

Another limitation of this study is that the parameters used in the fatigue model come from the literature (*Xia and Law*, 2008), in which the values were assigned arbitrarily for conceptual purposes. For this reason, the change in the absolute values of labor duration predicted in this fatigue study may not be reliable. However, the qualitative results from the model should still hold. In other words, a more accurate model using realistic model parameters will likely show similar trends to those we have shown in this study. In future work, these model parameters can be obtained from appropriate ergonomic tests on women.

CHAPTER IX

A Subject-Specific 3-D Anisotropic Visco-hyperelastic Finite Element Model of the Second Stage of Labor: Female Pelvic Floor Stress And Strain

9.1 Introduction

The common female pelvic floor dysfunctions include urinary incontinence, fecal incontinence and pelvic organ prolapse. In United states of America, approximately 11% of women eventually require surgery for pelvic floor dysfuncion (*Olsen et al.*, 1997). The need for treating pelvic floor dysfunction increases inexorably with advancing age (*Gainey* 1943, *Foldspang et al.* 1992, *Ryhammer et al.* 1995, *Mant et al.* 1997). With the burgeoning elderly population, this means more and more women are being affected by the sequelae from birth-induced injuries, and this common health problem is adversely affecting women's opportunities in employment, enjoyment and health-promoting exercises.

It is believed that female pelvic floor dysfunctions are highly associated with having given vaginal birth. For example, parity is the single most important risk factor for developing stress urinary incontinence (*Foldspang et al.*, 1992) and pelvic floor

prolapse (*Mant et al.*, 1997). Recent imaging investigations have demonstrated that levator ani muscle damage can occur during vaginal birth (*Tunn et al.* 1999, *Hoyte et al.* 2001, *DeLancey et al.* 2003, *Dietz and Lanzarone* 2005, and *Ashton-Miller and Delancey* 2009), with sequelae including stress urinary incontinence (*Kearney et al.*, 2006) and pelvic organ prolapse (*Hoyte et al.*, 2004).

Since some birth-induced injuries are not recoverable, the functional restoration of pelvic floor from later surgery or rehabilitation is far from satisfactory (*Kahn and Stanton*, 1997). Therefore, the most natural and effective way to avoid or decrease pelvic floor dysfunction is to prevent the problem occuring during parturition. Being a physiologically intricate and structurally complex region, the pelvic floor is subjected to remarkable biomechanical changes during the second stage of labor. When the fetal head moves progressively through the pelvic canal, it inevitably induces substantial stretch in the pelvic floor muscles. Up to now, the mechanisms of levator ani muscle injury associated with vaginal delivery have not been fully understood. To elucidate which childbirth factors may influence the risks of pelvic floor dysfunctions, it is necessary to better understand the biomechanics of pelvic floor muscles during the second stage of labor. Computer modeling based on various numerical computing techniques has emerged as an important tool for studying biological tissues and processes. The advantage of computer modeling is that, with great convenience, high flexibility, and very low cost, it can perform some sensitivity analyses that are otherwise impossible to implement using experimental approach.

In the past five years, several computer models of the female pelvic floor function have been published; most have used finite element methods. A pioneering model was by *Lien et al.* (2004) which, although a pure 3-D geometric model, was the first one to show how much the levator ani muscles are stretched during vaginal birth. Since then, a series of finite element models based on the continuum approach have been published. These include models for pelvic floor muscles (*d'Aulignac et al.* 2005, *Lee*

et al. 2005 & 2009, *Martins et al.* 2007, *Li et al.* 2008, and *Parente et al.* 2008, 2009a & 2009b), both pelvic floor and the anal canal (*Noakes et al.* 2006, 2008a & 2008b), pubic symphysis (*Li et al.* 2006 & 2007) and the vagina (*Chen et al.* 2009 and *Calvo et al.* 2009). The main limitation of these studies is that they 'borrowed' material properties from other soft tissues, such as cardiac tissue (*d'Aulignac et al.* 2005, *Martins et al.* 2007, *Parente et al.* 2008, 2009a & 2009b, and *Calvo et al.* 2009), tongue and facial muscles (*Lee et al.*, 2005), and skeletal muscles (*Li et al.*, 2008).

The aim of this study was to develop an anatomically accurate finite element model to predict where the stress and strain are greatest when the fetal head is driven through the pelvic floor. The accuracy of our model comes from three aspects: (1) reconstructing of the geometry of female pelvic floor using accurate MRI scanning data; (2) employing accurate material constitutive relations derived from robust biaxial tests on human pelvic floor muscles; (3) employing accurate data on the effect of pregnancy on pelvic floor tissues; and(4) using the general-purpose ABAQUS connector elements to specify muscle boundary attachments as close to the physiological process as possible.

9.2 Methods

9.2.1 Geometric model

The subject-specific geometry in this 3-D finite element model came from MR scans of a selected, healthy nulliparous woman at 40-week gestation (KCL PhD thesis 2006). A 1.5T superconducting magnet (Sigma Horizon LX, General Electric) was used to take multiplanar 2-D proton density MR images. The fields of view of images are 20×20 cm for the sagittal scans and 16×16 cm for the axial and coronal scans. All slices were 4-mm thick with a 1-mm gap between slices. The outline of pelvic

floor structures and the fetal head were traced on each MR scan and lofted to form 3-D volume rendering geometric model using a 3D slicer, an open source software for visualization and image computing. The obtained volume-rendered model was then imported into I-DEAS (version 9.0, EDS, Plano, TX) and converted to a surface-rendered model for finite element simulation. The resulting 3-D surface of the levator ani muscle includes the pubovisceral muscle, puboperineal muscle, puboanal muscle, and iliococcygeal muscle, as shown in Figure 9.1.

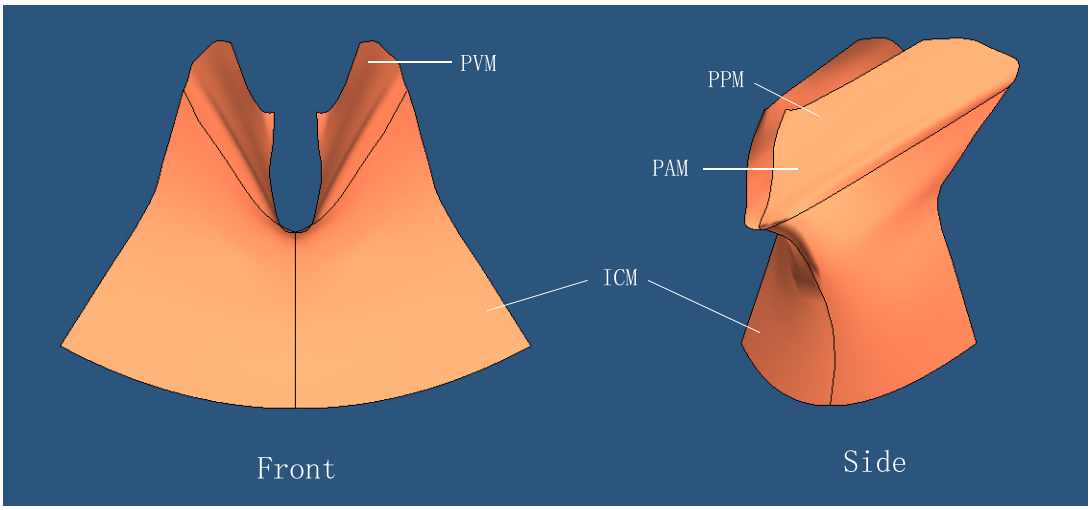

Figure 9.1: 3-D surface of levator ani muscle generated from slices of MR scans, including pubovisceral muscle (PVM), puboperineal muscle (PPM), puboanal muscle (PAM), and iliococcygeal muscle (ICM).

The fetal head geometry was modified to represent the molding effect during vaginal delivery, based on literature (*Carlan et al.*, 1991), and the resulting 3-D surface is shown in Figure 9.2. The effect of two fetal positions, occipito-anterior and occipito-posterior, were compared in terms of their effect on the deformation of pelvic floor tissues during the second stage of labor.

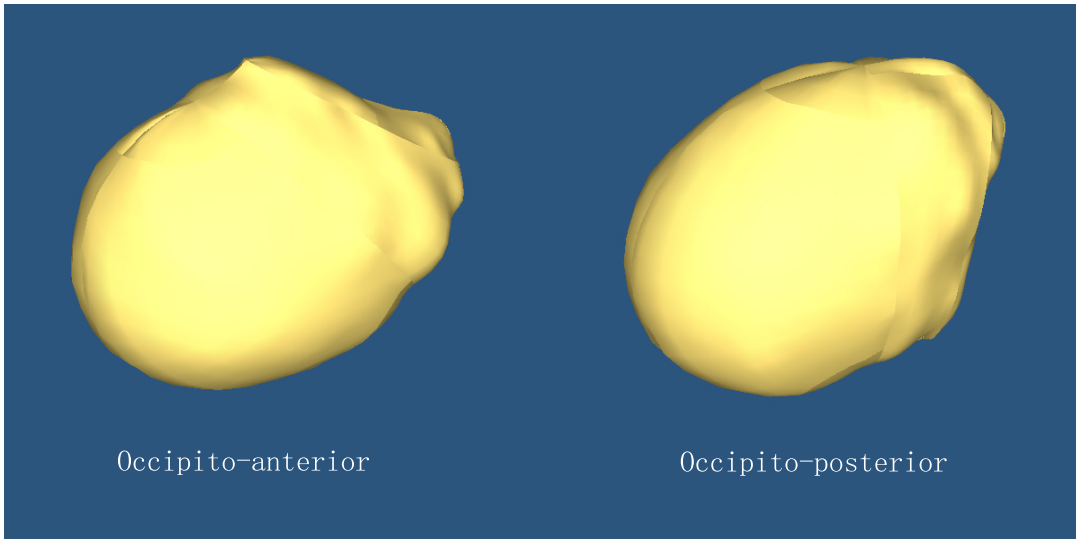

Figure 9.2: 3-D surface of fetal head generated from slices of MR scans. The two fetal positions included are occipito-anterior (facing downward) and occipito-posterior (facing upward).

9.2.2 Finite element model

Hypermesh V9.0 (Altair, Irvin, CA) was used for pre-processing of the model, including generating finite elements from 3-D surface, defining material properties, prescribing boundary conditions, and exporting input file for FEM solver. The ABAQUS explicit solver V6.8(SIMULIA, Providence, RI) was used to solve the model. The 3-D finite element model is shown in Figure 9.3, which includes a total of 7608 nodes and 9153 elements. The type and number of the ABAQUS elements for each anatomical components are listed in Table 9.1.

Generally, the out-of-plane bending stiffness of a planar soft tissue is negligible compared with its in-plane stiffness. Therefore, the levator ani and perineal body were represented by membrane elements, instead of shell elements, in this study. In Figure 9.3, connecting tissues (ATLA, coccyx, and sacrospinous ligaments) were represented by a series of lines (CONN3D2 elements). Here, the line just represents an associating pair between the nodes at the two ends; it does not represent the direction of force

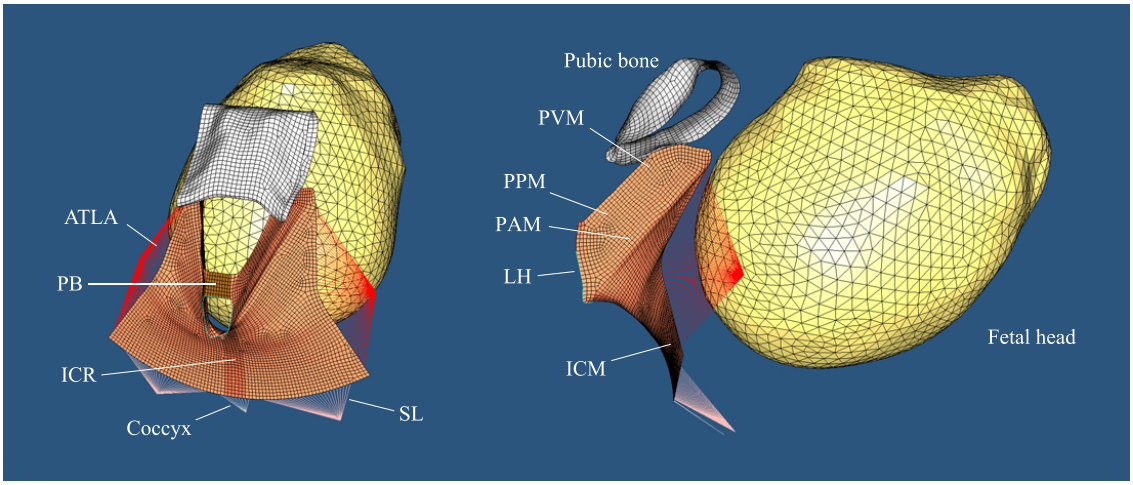

Figure 9.3: The 3-D finite element model, including perineal body (PB), levator ani muscle (subdivided into pubovisceral muscle (PVM), puboperineal muscle (PPM), puboanal muscle (PAM), iliococcygeal muscle (ICM), iliococcygeal Raphe (ICR)), fetal head, pubic bone, coccyx, and some connecting tissues, including arcus tedineus levator ani (ATLA) and sacrospinous ligaments (SL). LH refers to levator hiatus.

between them. Indeed there are up to 6 degree of freedoms (DOF) activatible in the CONN3D2 element and different constitutive behaviors, such as spring, dashpot, stop and lock, can be used for each DOF. This provides great convenience in simulating surrounding connecting tissues without introducing more complicated geometries. 3-D rod-like truss elements (T3D2) were used to simulate the reinforcing effect of the external anal sphincter muscle on the anal hiatus.

Since the perineal body was not included in the MRI scanned surface, a patch of plane tissue was manually added between the levator hiatus and the anal hiatus to represent the perineal body. Both the fetal head and the pubic bone were simulated with rigid surfaces. The pubic bone did not participate in the computation and only served as a reference for defining the locus of the fetal head center during the second stage of labor (*Curve of Carus*). A contact pairing relation was defined between the fetal head and the pelvic floor tissues, so that non-penetration constraints were internally reinforced when the deformable muscles were stretched by the rigid fetal

Table 9.1: ABAQUS elements used in the model

	Type	Number
Levator ani	Deformable membrane elements (M3D4R & M3D3)	4300
Pereal body	Deformable membrane elements (S4R)	63
Fetal head	Rigid shell elements (R3D3)	3110
Pubic bone	Rigid shell elements (R3D4)	1450
Coccyx	Connector elements with LINK-CARDAN behavior (CNN3D2)	9
Sacrospinous ligaments	Connector elements with CARDAN-CARTESIAN behavior (CNN3D2)	70
ATLA	Connector elements with CARDAN-CARTESIAN behavior (CNN3D2)	108
Anus hiatus	Truss elements (T3D2)	41
Sacral-coccygeal junction	Both MASS and ROTARY elements for the same point	2

head. The simulation period was 10 minutes.

9.2.3 Boundary conditions

All 6 degrees-of-freedom of the pubic bone were set to zero so that it stayed fixed in space, serving as the reference point for defining the curve of Carus. Based on descriptions in classic obstetrics textbooks and communications with experienced obstetrical professionals, a sequence of fetal head positions and orientations that may occur during birth were determined, and a Matlab code was used to interpolate the trajectory and rotation of the fetal head by spline interpolation, and constraints were applied on the fetal head so that its displacement and rotation exactly followed the interpolated displace and rotation curves. The sequences of fetal head positions and orientations for occipito-anterior and occipito-posterior presentations are shown in

Figure 9.4, and the corresponding smoothly interpolated curves of trajectory and rotation is shown in Figure 9.5. Simulation started from a location such that the fetal head moved 23 mm before it first contacted the levator ani muscle. and ended such that the fetal head finished a whole distance of 166 mm and a total rotation of 90 degree.

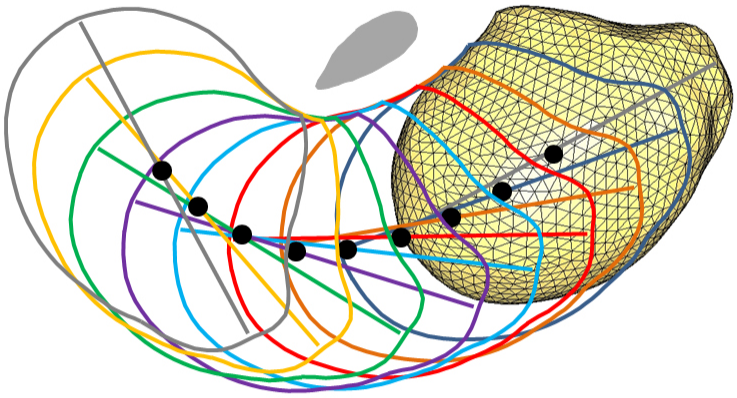

(a) Occipito-anterior

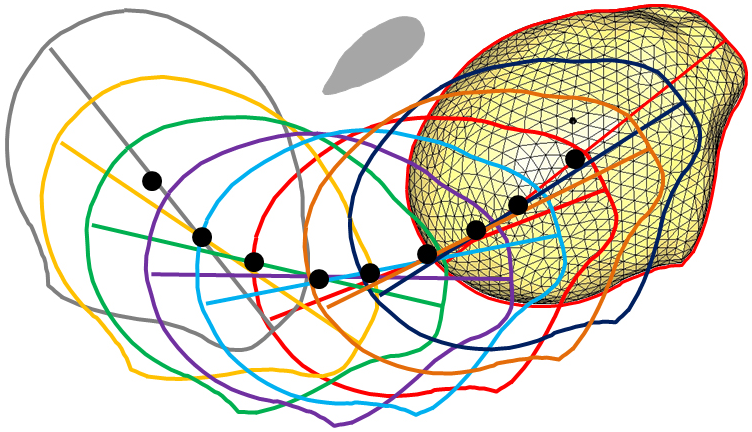

(b) Occipito-posterior

Figure 9.4: Curve of Carus (black dots) for prescribing displacement and rotation (shown by orientation lines) of the fetal head. The elliptical gray region is the cross-section of the pubic bone in the mid-sagittal plane.

The coccyx was represented by CONN3D2 elements with LINK-CARDAN be-

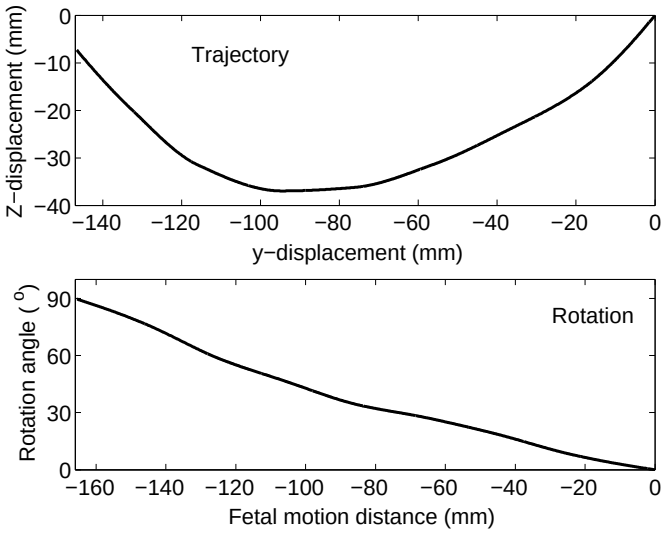

(a) Occipito-anterior

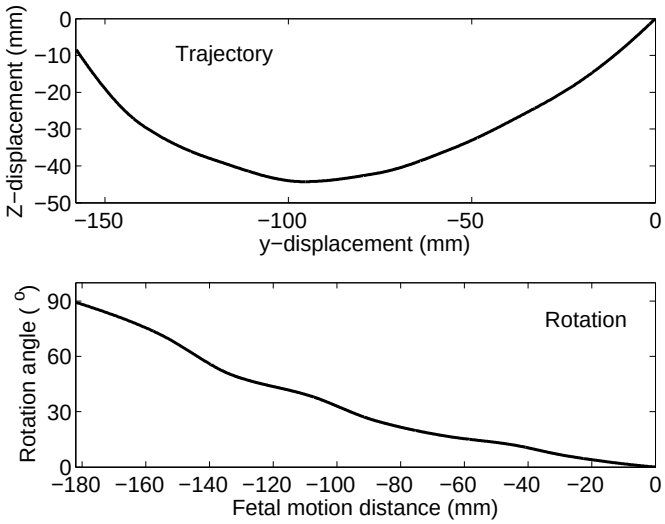

(b) Occipito-posterior

Figure 9.5: The interpolated trajectory and rotation of fetal head.

havior, so that it can rotate about a transversely-oriented hinge joint at the sacral-coccygeal junction. The pubovisceral muscle inserted into the pubic bone, the pubic origin, and the ischial spine insertion of the arcus tedineus, so they were set to be translationally fixed but rotationally free. The region connecting the iliococcygeal muscle and the sacrospinous ligaments were constrained with CONN3D2 elements

embeded with 3 orthogonal springs. A similar method was used to constrain the region connecting the iliococcygeal muscle and the arcus tedinous levator ani. Specifically, this boundary was fixed in the fetal descending direction to avoid excessive downward motion of the levator ani muscle, but lateral motion is allowed. The three orthogonal spring stiffnesses of CONN3D2 elements were tuned such that unrealistic motions of the margins of iliococcygeal muscle were avoided.

To avoid unnecessary simulation noise, a symmetry condition was applied on the iliococcygeal raphe so that it could not move transversely. For all other boundaries, including perineal body, urogenoital hiatus, and anal hiatus, no constraint was applied to allow for free boundaries.

9.2.4 Material properties

The anisotropic visco-hyperelastic constitutive law proposed by Holzapfel was used to model the levator ani muscle and the perineal body (*Holzapfel et al.* 2000 and *Gasser et al.* 2006). The details of the constitutive equation and the corresponding material properties are described in Chapter IV. The material constants were scaled, based on the results of Chapter II and chapter III, to reflect the effect of term-pregnancy.

To define anisotropy of material property induced by fiber reinforcement, local material coordinate systems needs to be defined at element level. When the underlying element deforms, the attached local material coordinate system rotates with it so that one of its axis always keeps aligned with the fiber direction.

The fiber directions of the levator ani muscle and the perineal body used in this model were based on data from *Shobeiri et al.* (2008). Theoretically, each element has its own local material coordinate system. However, practically, the elements with similar material orientations are often grouped together and assigned the same material coordinate system. As a first-order approximation, the muscle elements in

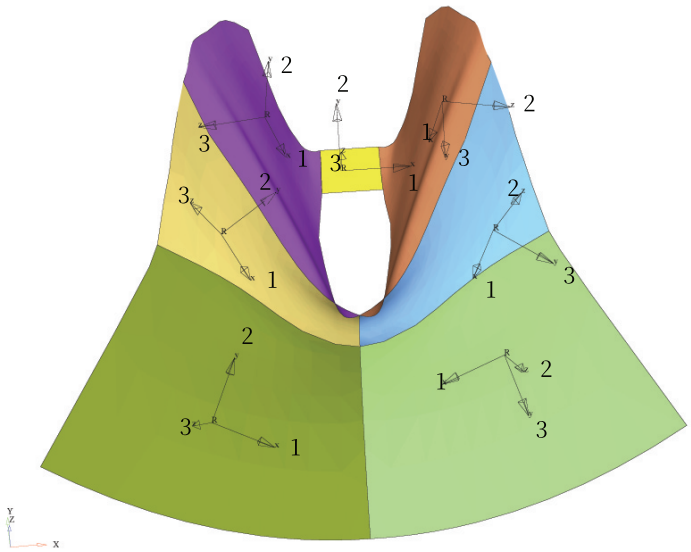

Figure 9.6: The distribution of the fiber orientations in the levator ani and the perineal body. The muscles were divided into totally 7 sub-regions; each region was assigned a local coordinate system, with the "1" axis representing the fiber direction.

this study were sub-divided into 7 regions and the elements in each sub-region were assigned the same fiber direction, as shown in Figure 9.6.

9.3 Results

9.3.1 Deformation, stress and strain of pelvic floor tissues

The simulated progress of the second stage of labor is shown in Figure 9.7. As can be seen, when the fetal head passed through the birth canal, it induced marked stretch to the pelvic floor tissues. As the perineal body slid through the point farthest away from the origin of the pubovisceral muscle, called fetal crowning, the stretch of the levator hiatus reached its peak value. It was predicted that fetal crowning occurred when the fetal head moved 122 mm along the curve of Carus. The deformation and stress distributions of the levator ani muscles at different fetal displacements are shown in Figure 9.8. The region of the levator hiatus has much higher stress levels

than other regions, with the peak stress ($\sim$ 9 MPa) concentrated at enthesis region of the pubovisceral muscle beneath the pubic bone.

Since the levator hiatus region has a high risk of muscle injury, we examined how the stress and strain developed in this region during the second stage of labor. At each point the tensorial stress state (normal plus shearing stresses) can be equivalently represented by three normal principal stresses, two in-plane stresses and one out-of-plane stress. The distribution of the three principal stresses in the pelvic floor tissues at the time of fetal crowning (122 mm displacement) is shown in Figure 9.9, from which it can be seen that only the in-plane principal stress component along the hiatal edge was significant, and the two other principal stress components were negligible. The maximal in-plane stresses in the levator hiatus region were aligned along the hiatal edge, and had much higher values than in other regions. This stress pattern implies a high risk of muscle injury in this region, and the tearing direction would be perpendicular to the edge.

Despite being the last tissue part to be engaged, the levator hiatus undertakes the largest distension at fetal crowning to allow vaginal childbirth. The time history of the perimetric length of the levator hiatus, and the stretch ratio over the whole length during the second stage of labor are plotted in Figure 9.10. At the beginning of the second stage of labor, the perimeter of the levator hiatus was 85 mm. At the time of fetal crowning, it was stretched to 302 mm, corresponding to a stretch ratio of 3.55. This result is close to the value of 3.26 suggested by a geometric model (*Lien et al.*, 2004), and within the range $1.62 \sim 3.76$ suggested by a statistical study on 227 women (*Svabík et al.*, 2009).

To see which regions are most vulnerable to tearing injury, the distributions of stress and strain along the levator hiatus were computed. A path for plotting these distributions was chosen, starting from the middle of the perineal body until the enthesis of the pubovisceral muscle beneath the pubic bone. The distribution of

the maximal in-plane principal stress along the hiatus is shown in Figure 9.11. For example, at fetal crowning, the highest stress level (9.0 MPa) occurred in the enthesial region where the pubovisceral muscle arises to beneath the pubic bone, and the second highest stress level (7.2 MPa) occurred near the region of perineal body. These two stress concentration regions coincide with the clinically observed locations of high risk of tissue injury.

The local tensorial strain status at a point (normal stretch plus shearing) can be equivalently represented by three principal stretch ratios. Coinciding with the distributions of the maximal principal stresses (Figure 9.9), the maximal principal stretch ratios in the hiatus region were aligned with the hiatal edge and had much higher values than in other regions. The distributions of the maximal principal stretch ratio along the hiatus at different fetal displacement levels are shown in Figure 9.12. Note, the jumps in the stretch ratio curves were due to the discontinuity in tissue stiffness between perineal body and levator ani muscle. At fetal crowning (122 mm displacement), the highest stretch ratio (4.64) occurred near the enthesis of the pubovisceral muscle, and the second highest stretch level (4.15 MPa) was located near the perineal body region. These two large stretch areas coincide with the clinically observed locations of high risk of tissue injury. Since it has been observed from Figure 9.10 that the average stretch ratio of the levator hiatus at the time of fetal crowning is 3.55, we can conclude that the tissue stretch along the levator hiatus is inhomogeneous, with highest stretch at the enthesis of the pubovisceral muscle, followed by the next highest stretch in the perineal body region.

9.3.2 Effect of fetal head rotation on levator ani stretch

In the curve of Carus depicted in Figure 9.4, the (shortest) fetal-pubic distance was kept nearly constant due to separation from the pelvic floor tissues. When the fetal head moves and rotates around the pubic bone, we denoted the location as

'flexing point' when the occipital bone arrives beneath the lowest point of the pubic bone. Based on classic textbooks on obstetrics and communication with experienced obstetrical professionals, we hypothesized that optimum curve of Carus leading to minimum stretch of the levator ani muscles has to meet two requirements: (1) when the fetal head moves around the pubic bone, its occipital surface should keep parallel to the outline of the pubic bone; (2) When the fetal head reaches the flexing point, it begins to rotate upward so that, at the end of the curve of Carus, its final orientation is parallel to the initial orientation. We denoted this case as *normal rotation* (NR) in this study.

We are also interested in how early or late sagittal rotation of the fetal head might affect the stretch of the levator ani muscle. One possible scenario, denoted by *early rotation* (ER) is that the fetal head begins to rotate upward before reaching the flexing point. In this case, the fetal head trajectory has to be adjusted downward to make space to accommodate upward rotation. The opposite scenario, denoted by *late rotation* (LR), is that the fetal head begins to rotate upward after it moves beyond the flexing point. In this case, the downward trend of the trajectory has to be extended beyond the flexing point and then goes upward. The comparison among NR, ER and LR is shown in Figure 9.13. Here, the three fetal rotation histories were set to have same initial and final location and orientation for meaningful comparison.

Simulation results showed that fetal crowning for NR, ER, and LR happened at 122 mm, 130 mm, and 132 mm of fetal displacements along the curve of Carus, respectively. The distributions of the maximal principal stretch ratio along the levator hiatus at fetal crowning for the three fetal rotation scenarios are shown in Figure 9.14. It can be seen that the stretch of the levator hiatus was slightly increased by early rotation, but was significantly increased by late rotation, with the peak local stretch ratio reaching 5.35 at the enthesis of the pubovisceral muscle. This can be explained by the fact that, in the case of late fetal rotation, the contact between the perineal

body and the forefront of the fetal head was longer, therefore the levator ani muscle undertook larger stretch.

9.3.3 Sensitivity analyses involving the stiffness of perineal body

The perineal body is the last part of the pelvic floor tissues to pass the crowning plane of the fetal head, thus it is reasonable to believe that its stretchability, determined by its stiffness, plays an important role in accommodating the passage of the fetal head. As concluded in previous section, the local principal stretch ratio along the levator hiatus was inhomogeneous, with peak stretching occurring at the enthesis of the pubovisceral muscle, and the second highest stretch happening in the perineal body region. Therefore, we hypothesized that decreasing the stiffness of the perineal body should re-distribute stretch ratio along the levator hiatus. Specifically, we hypothesized that decreasing the stiffness of the perineal body will decrease the stretch ratio at the enthesis of the pubovisceral muscle. To test this "fusible link" hypothesis, a sensitivity analysis with different perineal body stiffness values was performed.

Comparison of the maximal principal stretch ratio distribution at fetal crowning along the levator hiatus between normal and 40% reduced stiffness of perineal body is shown in Figure 9.15. As can be seen, when the stiffness of the perineal body decreased by 40%, the maximal principal stretch ratio at perineal body region, at the time of fetal crowning, increased by 14.5% from 4.15 to 4.75, while the maximal principal stretch ratio at the enthesis of the pubovisceral muscle decreased by 8% from 4.64 to 4.27. The sensitivity analysis showed that perineal body softening helped to mitigate the required local stretch ratio at the enthesis of the pubovisceral muscle, as indicated in Figure 9.16, thereby reducing the risk of tissue avulsion injury there. For example, when the perineal body stiffness decreased by 40%, 50%, and 60%, the maximal principal stretch ratio at the enthesis of the pubovisceral muscle decreased by 8.2%, 12.8%, and 17.8%, respectlvely. However, if the change of perineal stiffness

is too small, such as less than 20%, the effect on reducing pubovisceral muscle injury is negligible.

9.3.4 Occipito-anterior vs. occipito-posterior fetal positions

Both the occipito-anterior (OA) and occipito-posterior (OP) fetal head presentations were simulated in this study and the corresponding stretch statuses of the pelvic floor tissues were compared. The predicted time history of the stretch ratio at the enthesis of the pubovisceral muscle for the two fetal positions is compared in Figure 9.17. For the OA presentation, the fetal crowning occurred at the 122 mm fetal head displacement along the curve of Carus, while for OP presentation it happened at the 148 mm displacement. At OP crowning, the stretch ratio at the enthesis of the pubovisceral muscle reached 5.04, 8.6% higher than the the value 4.64 of OA crowning. Thereby, we can conclude that occipito-posterior delivery posed a higher risk of injury to the pubovisceral muscle compared with occipito-anterior delivery.

The comparison between the simulated fetal crowning for the occipito-anterior and occipito-posterior presentations is shown in Figure 9.18. It is the shape of the fetal head that causes the difference in the stretching of pelvic floor muscle at fetal crowning. When the fetus is in the occipito-anterior position, the levator hiatus slid over the relatively flatter and smoother forehead of the fetal head until the crowning point. For the occipito-posterior presentation, the more steeply inclined and variable occiput make it harder for the levator hiatus to pass over, therefore the levator ani muscle is stretched more before it reaches the crowning point.

9.4 Discussion

Since the second stage of labor is a physiologically intricate and structurally complicated process, it bring some specific challenges to computer modeling. In the last 5 years, despite several finite element models about the second stage of labor having

been published, the significant computational challenges still remain. For example, some studies constructed their pelvic floor geometry from MRI scans of a cadaver, so they can never capture the geometry of the *in vivo* levator ani with its muscle tone and characteristic shapes. The common problem shared by all the existing pelvic floor models is that material properties from other soft tissues were used to model the pelvic floor tissues due to the lack of such data. In an effort to improve modeling technique of the second stage of labor, this study incorporated both anatomically realistic geometry and experimentally-derived constitutive equations of the pelvic floor tissues.

In the published birth models, somewhat arbitrary displacement constraints were applied on the boundary of the levator ani structure; a common example is applying the constraint of zero-displacement. In this study, those boundaries were modeled with connector elements, which allows for flexible constitutive relations in three degree-of-freedoms. Currently, even though only tentative constitutive relations, such as linear spring or dashpot, were used, this study suggested a general-purposed and feasible methodology for modeling boundaries without further introducing unnecessary surrounding geometries. More importantly, if the constitutive data of connecting tissues, such as sacrospinous ligaments and arcus tedinous levator ani, were available (from experiments), these data can be incorporated to greatly improve the physiological fidelity of the model.

One important finding from this study is the quantification of the deformation inhomogeneity of the levator hiatus. Simulation results predicted that the maximum value of the average stretch ratio of the levator hiatus is 3.5. However, the (local) principal stretch ratio is not uniformly distributed along the hiatus, with peak stretch ratio (4.64) at the enthesis of the pubovisceral muscle beneath the pubic bone, and the second highest value (4.15) located at the perineal body region. The two predicted high stretch concentration regions coincide with the clinically observed regions of high

risk of muscle injury (*Kearney et al.*, 2006).

The effect of the fetal head rotation on the stretch of levator ani muscles was first quantitatively investigated in this study. The important finding is that to bring minimal stretch to the levator ani muscles, the fetal head in occipito-anterior presentation should begin to rotate upward when its occipital bone of the fetal head reaches beneath the lowest point of the pubic bone. If the fetal head rotates before or after this optimal 'flexing point', more stretch would be brought to levator ani muscles. Specifically, late rotation brings significantly more stretch, thereby higher risk of muscle injury, than early rotation.

To our knowledge, this study is the first finite element model to investigate the sensitivity of the stretch of pubovisceral muscle to the stiffness of the perineal body in a test of 'fusible link' hypothesis (*Ashton-Miller and Delancey*, 2009). Studying the decrease of perineal stiffness is clinically meaningful. During the second stage of labor, hyaluronidase (HAase) is often injected into the perineal region to prevent maternal trauma (*Digonnet et al.* 1952, *Oleary and Erez* 1965, and *Scarabotto and Riesco* 2008). It was reported that after 3 to 4 minutes following injection of HAase in the perineal region, the perineal tissues exhibited softening, flexibility, and relaxation, facilitating the passage of the fetus through the vaginal canal(*Oleary and Erez*, 1965). Our simulation showd that decreasing the stiffness of perineal body mitigates the strain at the origin of pubovisceral muscle, thereby reducing the risk of levator ani injury. The result from our computer model provides a support for using HAase, or equivalent agent, from the perspective of biomechanics.

It is believed that the occipito-anterior position is ideal for birth, since the baby is oriented up so as to fit through the mother's pelvis as easily as possible. Our simulation showed that the occipito-anterior fetal presentation is the optimal position, since the smaller part of the head stretches the levator ani muscle first, leading to smaller stretch in the muscle, and therefore less pelvic resistance to the fetal head

descent. Indeed, mothers of babies in the posterior position are more likely to have long and painful labors as the baby usually has to turn all the way round to facing down in order to be born.

The main limitation of this model is that the fetal head was driven by an assumed velocity instead of realistic intrauterine pressure (used in Chapter V) (the reason was explained in Section 1.2.2.3 on page 16). With this simulation period being 10 minutes, the long-term relaxation behavior of the tissues did not come into play (see Chapter IV). In addition, the calculated stress level are likely overestimated. However, the results of sensitivity analyses should still be valid. The resulting strain values are quantitatively correct. A simulation of using intrauterine pressure in this anatomically realistic 3-D model was tried in this dissertation, but the simulation took so long that it was discontinued. However, this challenge may be solved by running the simulation on parallel clusters. Another possible simulation approach would be to apply the velocity time history calculated in the axisymmetrical model in Chapter V to the realistic geometry model of this chapter; this would yield improved predictions of tissue stress.

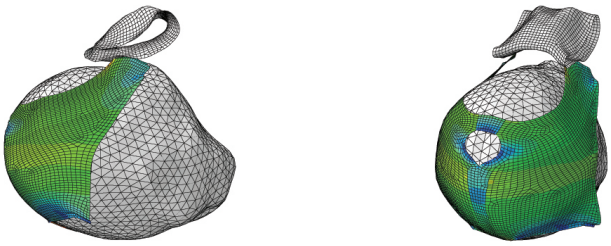

(a) $D = 70$ mm, $\theta = 30^o$

(b) $D = 122$ mm, $\theta = 56^o$

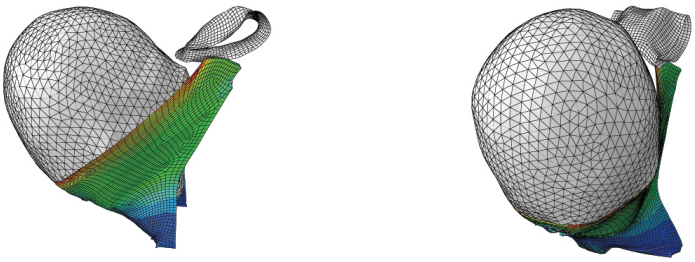

(c) $D = 140$ mm, $\theta = 74^o$

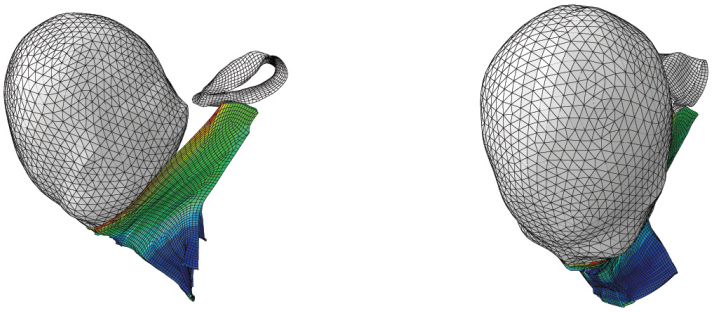

(d) $D = 166$ mm, $\theta = 90^o$

Figure 9.7: Simulated second stage of labor at different values of D. The fetal head moved 23 mm before it first contacted the levator ani muscle. At left is a left lateral view; at right is a three quarter view. D is the displacement along the curve of Carus, and θ is the rotation angle.

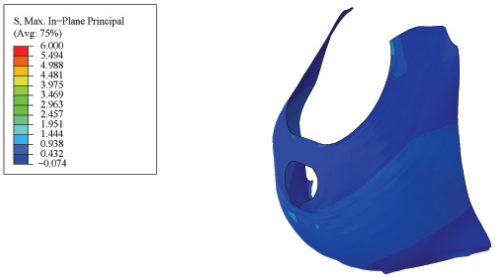

(a) $D = 60$ mm

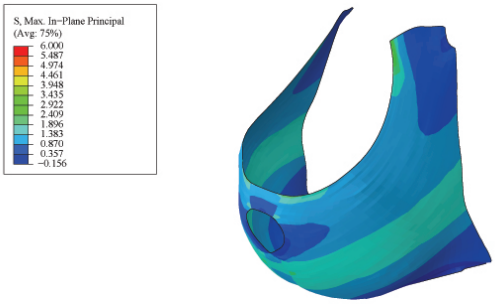

(b) $D = 80$ mm

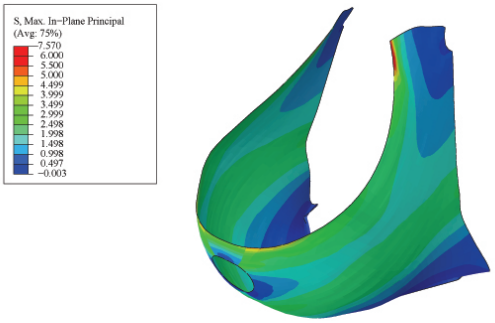

(e) $D = 100$ mm

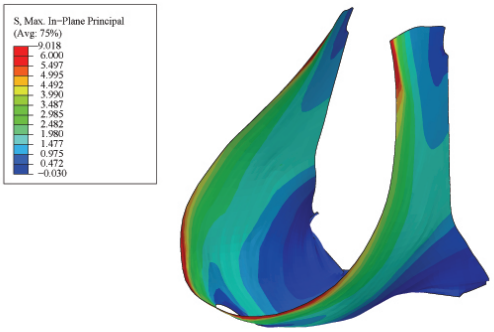

(f) $D = 122$ mm

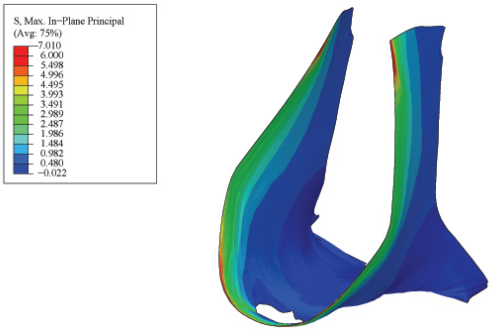

(i) $D = 140$ mm

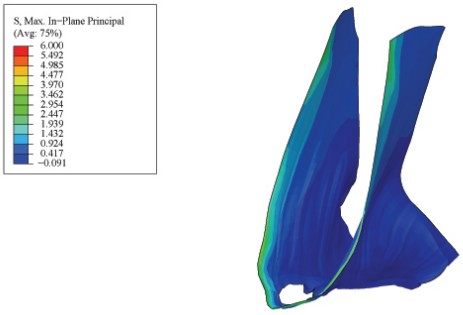

(j) $D = 166$ mm

Figure 9.8: The deformation and stress level of the pelvic floor tissues at different fetal head displacement levels (D) along the curve of Carus.

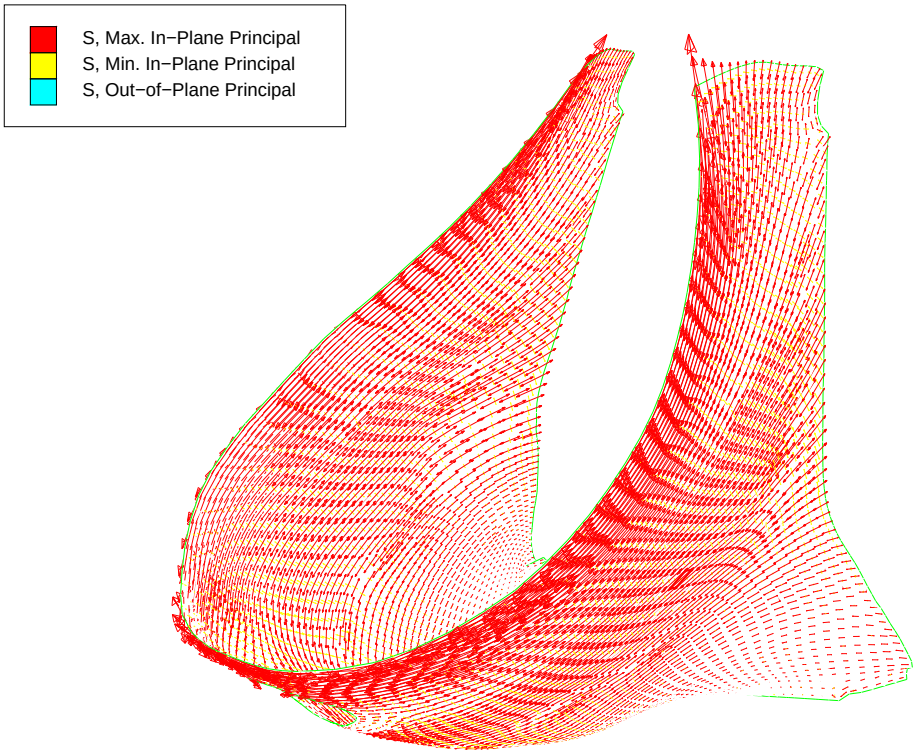

Figure 9.9: Principal stresses in the levator ani muscles at the time of fetal crowning (122 displacement along the curve of Carus).

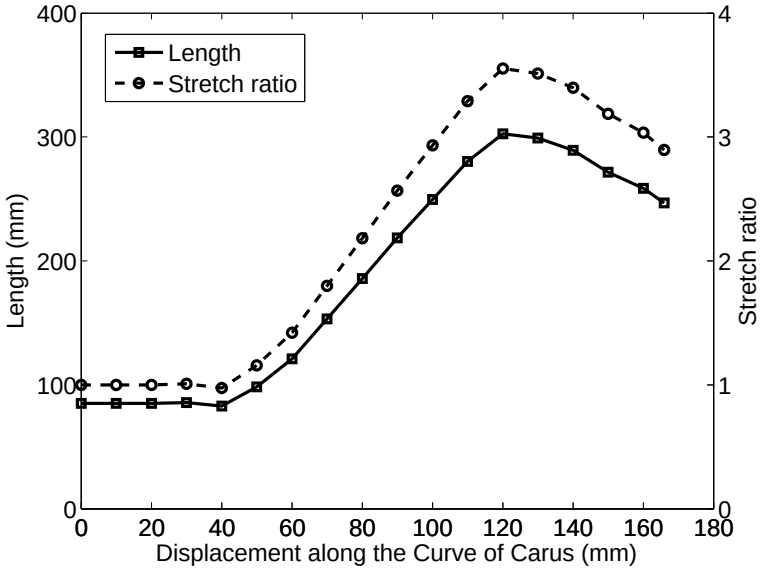

Figure 9.10: The changes in perimetric length and overall stretch ratio of the levator hiatus during the second stage of labor.

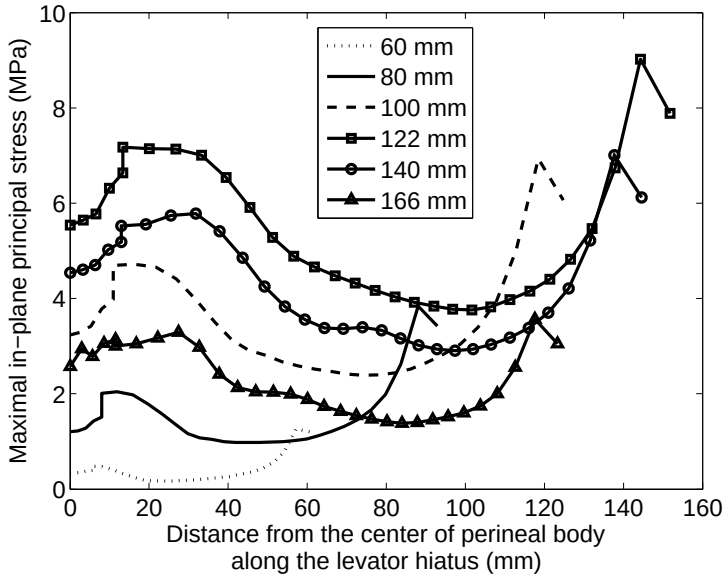

Figure 9.11: The distribution of the maximal in-plane principal stress along the levator hiatus, at different fetal displacements. The abscissa is the distance to the center of perineal body along the hiatus, so the left and right ends of each curve correspond to the perineal body region and the enthesis of pubovisceral muscle, respectively.

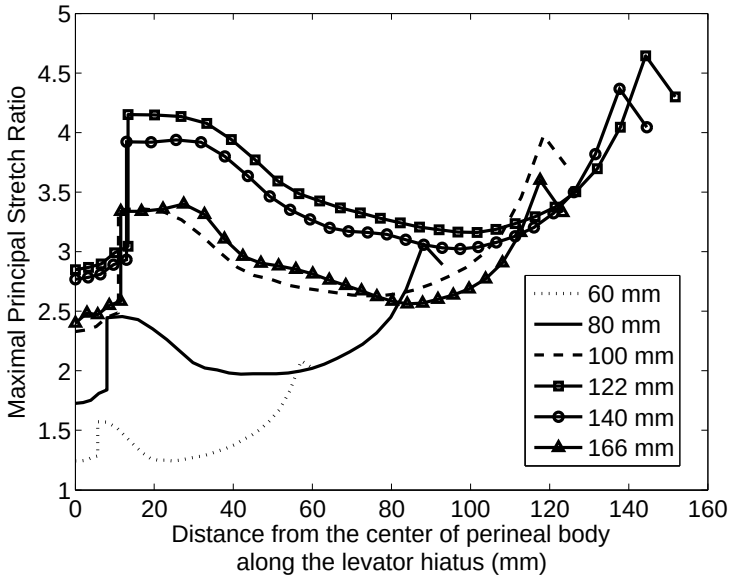

Figure 9.12: The distribution of the maximal in-plane principal stretch ratio along the levator hiatus, at different fetal displacement levels. The abscissa is the distance to the center of perineal body along the hiatus, so the left and right ends of each curve correspond to the perineal body region and the enthesis of the pubic bone.

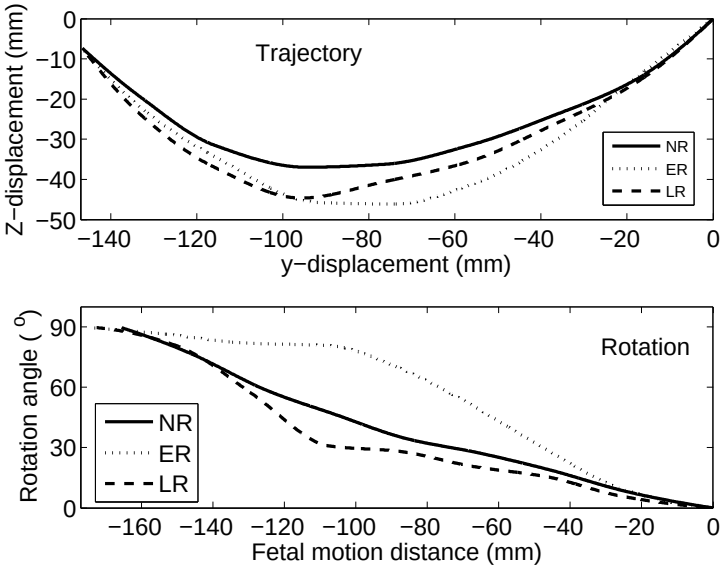

Figure 9.13: The fetal head trajectories and rotations for the three rotation scenarios: normal rotation (NR), early rotation (ER), and late rotation (LR).

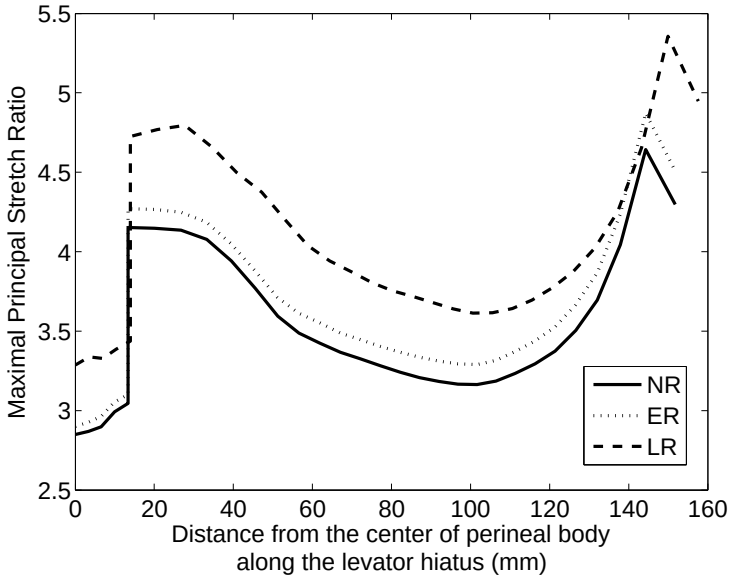

Figure 9.14: The maximal principal stretch ratio distributions along the levator hiatus, at fetal crowning, for the three rotation scenarios: normal rotation (NR), early rotation (ER), and late rotation (LR).

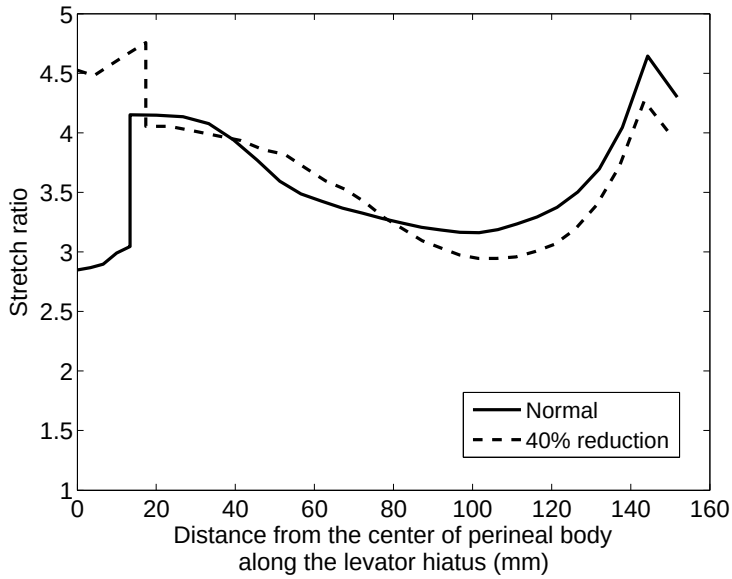

Figure 9.15: Distribution of maximal principal stretch ratio along levator hiatus at fetal crowning, compared between normal and 40% reduced stiffness of perineal body.

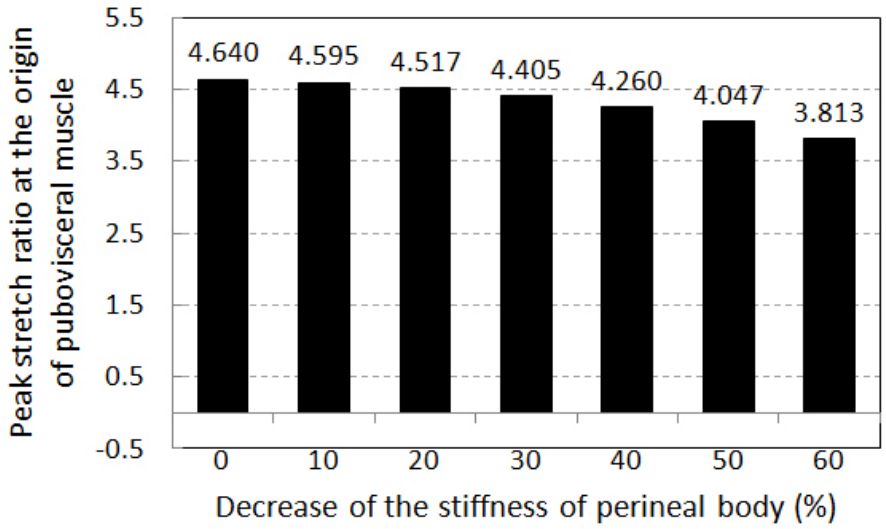

Figure 9.16: Simulated effect of decreasing perineal stiffness on the peak stretch ratio of the pubovisceral muscle

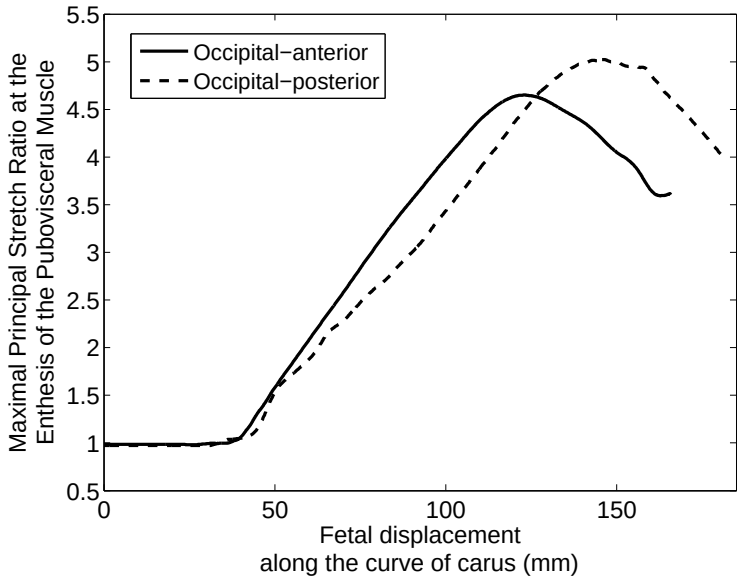

Figure 9.17: Predicted time history of the stretch ratio at the origin of pubovisceral muscle for the two fetal head presentations.

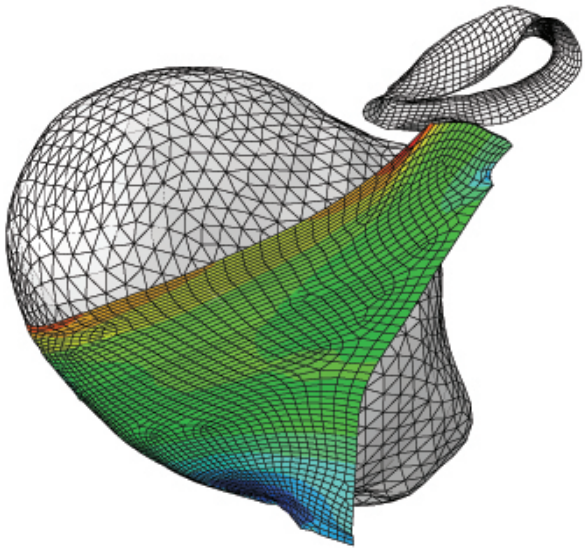

(a) Occipito-anterior fetal head crowning at the 87 mm fetal descent

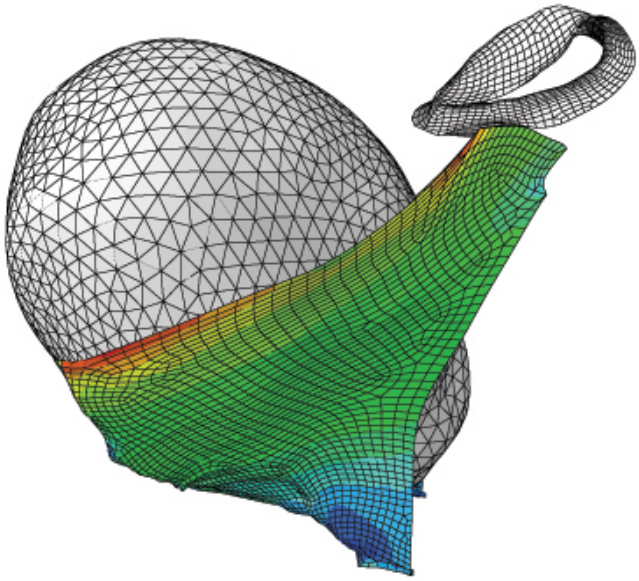

(b) Occipito-posterior fetal head crowning at the 83 mm fetal descent

Figure 9.18: Simulated fetal crowning for the occipio-anterior and posterial fetal positions.

CHAPTER X

General Discussion

Pelvic floor dysfunction (PFD) is a common women's health problem and it is believed to be strongly associated with having given vaginal birth (see Chapter I). However, the pathomechanics of this problem still remain poorly understood. This dissertation was an attempt to improve our current understanding of the mechanisms underlying the pelvic floor dysfunction, and to provide insights for more efficient delivery from a biomechanics perspective.

During pregnancy, the pelvic floor tissues undergo a remodeling process to become more distensible in order to accommodate passage of the fetal head. The existing literature reporting the effects of pregnancy have focused on isotropic linear time-independent elasticity, i.e., Young's modulus of the tissues. A novel aspect of this thesis is that it is the first experimental study to investigate the effects of term pregnancy on the anisotropic, time-dependent, and nonlinear material properties of the birth-related soft tissues, and then implement them in a finite element model. As a first step, a custom-made biaxial tension test system was developed which is capable of performing both biaxial and uniaxial tension tests on soft tissues. In Chapters 2 and 3, a series of tests were performed on rat vagina and squirrel monkey pelvic floor tissues, and the null hypothesis that term pregnancy does not affect the viscoelastic properties of these tissues was tested. It was found that the characteristic

mechanical behaviors of those pelvic floor tissues include fiber-induced anisotropy, viscosity, and nonlinear elasticity. The null hypotheses tested on rat were rejected in that pregnancy makes the tissues not only more compliant but also more 'fluid-like' to aid stress relaxation. The null hypotheses tested on squirrel monkey were partially rejected, due to limited availability of specimens, in that pregnancy affects significantly the viscosity, but not the elasticity, of the tissues. This suggests that tissue relaxation, which is often neglected in the literature, also plays an important role in accommodating the passage of the fetal head during the second stage of labor, not just the tissue stiffness. It was found that tissue relaxation is almost independent of the fiber orientation.

Computer simulation has emerged as an important technique for studying the mechanisms underlying pelvic floor dysfunction. The dilemma is that there is a paucity of published data about material models required by these simulations, so existing published models have 'borrowed' material properties from other soft tissues. An innovation in this dissertation is that it begins to fill this literature gap. In Chapter 4, specimens of female human pelvic floor muscle and perineal body were tested, and material parameters of a robust and feasible anisotropic viso-hyperelastic constitutive model were extracted from the experimental data. The constitutive model obtained is easy to implement since it has been embedded in ABAQUS, a widely-used commercial finite element code. We believe this effort will increase the accuracy of current numerical simulations on human pelvic floor structure.

A prolonged second stage of labor is strongly associated with increased risk of pelvic floor dysfunction. Therefore, in Chapter 5, a 3-D axisymmetric finite element model was developed to theoretically investigate how various and maternal and obstetrical factors affect the duration of the second stage of labor. This work serves as an improvement over a recent paper published in our group (*Lien et al.*, 2009) by using a more general finite element approach, a more accurate constitutive equation

derived from experimental tests, more clinically realistic intrauterine pressure profile, and a wider range of factors being considered. Important findings include: (1) among the six studied pushing profiles, the *peak* pushing profile is most efficient; (2) labor duration is very sensitive to the volitional pushing magnitude; decreasing magnitude has greater effect than increasing magnitude; (3) volitional pushing should be timed to be as close to the center of uterine contraction as possible to obtain maximal pushing efficacy. In Chapter 6, sensitivity analysis of the effect of pelvic floor muscle on the labor duration was conducted. It was found that labor duration is most sensitive to tissue stiffness, followed by long-term relaxation behavior. It is interesting to note that labor duration is relatively insensitive to short-term relaxation.

Vacuum extraction is commonly used in the USA when immediate delivery is required, but this operation is associated with an increased risk for perineal lacerations. Therefore, in Chapter 7, the 3-D axisymmetric energetics finite element model was used to perform sensitivity analyses of vacuum extraction. It was found that increasing the magnitude of continuous vacuum extraction is not a good strategy for facilitating vacuum delivery since the resulting elevated risk of muscle injury outweighs the benefit of reduced delivery duration. However, when a high vacuum extraction force is combined with intermittent pulling pattern, the delivery duration can be reduced with an acceptable risk of injury. This work is the first attempt to quantitatively study various vacuum extraction operational factors from a biomechanical perspective.

Maternal exhaustion due to muscle fatigue is an important factor leading to prolonged labor duration. Aiming at finding an optimal obstetrical coaching strategy to delay maternal fatigue during the second stage of labor, Chapter 8 incorporated a motor unit-based fatigue model into our axisymmetric energetics model (Chapter V) to study how maternal fatigue develops during the second stage of labor. It was found that increasing pushing magnitude does not necessarily reduce labor duration

as imagined due to early occurrence of fatigue. With maternal fatigue being considered, the 'peak' pushing style has the highest pushing efficacy while the 'Triple' style has the lowest. It is interesting to note that the interval between two volitional pushes within one uterine contraction has no effect on maternal fatigue. These results may be helpful in guiding midwives and obstetricians in the selection of appropriate coaching strategies.

The physiological and structural complexity of processes involved in the second stage of labor pose a variety of challenges to computer modeling, therefore some assumptions, realistic or not, have had to be made in order to make building and running models feasible. In Chapter 9, aiming at improving the accuracy of the modeling techniques for vaginal birth, a subject-specific 3-D finite element model of the second stage of labor was developed. The accuracy of our model comes from (1) anatomically realistic pelvic and fetal geometries; (2) correct material constitutive equations derived from testing on human pelvic floor tissues; (3) more accurate estimates of the effect of pregnancy on pelvic floor tissues; and (4) more general and flexible, but accurate, treatment of the boundary conditions of the muscle structure. Important findings from this study include: (1) At fetal crowning, the stretch of levator hiatus is inhomogeneous. The average stretch ratio was 3.55, while the peak stretch occurred at the enthesis of the pubovisceral muscle (5.04), and the second highest stretch was at the perineal region (4.15); (2) There is an optimal 'flexing point' for bringing minimal stretch to levator ani muscles. If the fetal head in occipito-anterior presentation begins to deflect before or after its occipital bone reaches beneath the lowest point of the pubic bone, the stretch to levator ani muscles would be higher, thereby increasing the risk of tissue injury. Late deflection brings higher risk of injury than early rotation; (3) Decreasing the stiffness of perineal body helps mitigate the peak stress level at the origin of pubovisceral muscle, thereby decreasing the risk of muscle injury there; (4) An occipito-posterior presentation induces higher stretch in levator ani muscles

compared with an occipito-anterior presentation. With the improved accuracy, our model can provide wider and more detailed information about the biomechanics of the second stage of labor, thereby helping to elucidate the mechanisms underlying the initiation of pelvic floor dysfunction (*Mant et al.*, 1997).

There are several limitations to the approaches used in this dissertation study. The first is the way to 'expel' the fetal head in our computer models. Naturally, the fetal head is driven by intrauterine pressure and pressure boundary condition corresponding to the uterine contraction and volitional pushing effort should be used. However, it is difficult to combine realistic pressure boundary conditions and anatomically realistic geometry in one birth model, and we had to make a compromise between them, depending on what was needed. In this dissertation, when the volitional pushing efficacy and labor duration were the focus of our concern, realistic pressure-mode boundary conditions were used, but simplified 3-D geometries were used to represent the maternal and fetal structures. This approach was used in Chapters V, VI, VII, and VIII. The simulation results obtained in this approach provide accurate information about stress evolution during the second stage of labor, but the strain information is less accurate due to simplified geometry used in the simulation. On the other hand, when the priority is to understand how much the pelvic floor tissues are stretched, anatomically realistic geometries were used but pre-assumed displacement or velocity boundary conditions were prescribed on the fetal head. In this approach (used in Chapter IX), the obtained strain information is correct, but the stress level might be overestimated since the long-term tissue relaxation does not come into play. Two levels of improvements can be implemented. At first level, we can apply the time history of fetal displacement or velocity obtained from the simplified geometry model into the realistic geometry model. In this way, the model prediction on the stess time history would be improved. At the second level, we can directly apply realistic intraabdominal pressure as the load to the realistic model so that accurate

predictions can be obtained for both strain and stress. The prerequisite of this approach is that we need to carefully add more surrounding pelvic floor structures into the model to form a birth canal as close to the realistic curve of Carus as possible, serving to constrain the fetal head to be on the correct trajectory and orientation. Theoretically, the feasibility of this approach is mainly restricted by the available computing resources. With parallel computing clusters becoming available, it will be possible to combine both accurate geometries and realistic intrauterine pressure conditions in one birth model.

The second main limitation is that we were not able to measure directly the mechanical properties of pregnant human tissues. We tested both pregnant and non-pregnant tissues collected from rat and squirral monkey to study the effect of the term-pregnancy on the viscohyperelastic properties of the tissues. We assumed that the measured scaling effect of pregnancy on the tissue properties from two different mammals applies to human tissues, therefore the obtained scaling factors were used in our computer models of the second stage of labor. Unfortunately to date there is no experimental evidence to support this assumption yet.

The third main limitation in this dissertation is that the effect of fetal head deformation was neglected in our models of the second stage of labor. In the axisymmetry model, the fetal head was assumed to be a rigid ball. In the realistic geometry model, even though anatomically accurate geometry of fetal head was used, the deformation of fetal head was still neglected. In the real process of the second stage of labor, the fetal head undergoes an adaptive process, changing both its shape and size when passing through the birth canal. These changes inevitably affect the maternal-fetal-interaction from the viewpoint of contact mechanics. On the other hand, in our study of vacuum delivery, we only focused on how different vacuum extraction factors are related to maternal morbidities. However, when clinical professionals make decisions on operations of vacuum delivery, neonatal outcome is another important factor to be

considered, and this was not considered in this thesis. Clinical data have shown that the success of vacuum delivery sometimes heavily depends on neonatal morbidity. Additionally, the time dependent properties of the fetal head, such as creep, might also plays a role in the biomechanics of the second stage of labor. To overcome these limitations, the fetal head can be treated as deformable body in the birth model. The cost of improved accuracies is increased computation time.

The fourth main limitation in this dissertation study is that active pelvic floor muscle contraction is ignored. During the second stage of labor, the fetal head is driven by intrauterine pressure which comes from active contractions of the diaphragm and abdominal wall muscles, but an active contraction of the pelvic floor muscle will tend to hinder the fetal head progress. Therefore, the woman is often coached by the obstetrical professionals to relax her pelvic floor muscle. However, it is possible that the woman contracts her pelvic floor muscle inadvertently or because of pain. In that case, the stress level of the muscle will increase. According to *Brooks* (2004), the most accurate muscle injury criterion for actively contracting muscle is the product of the stress and strain. Therefore, an active contraction of the levator muscle may increase the risk of muscle injury. On the other hand, active contraction also increases the muscle stiffness, thereby decreasing the muscle stretchability and risk of injury. These are two opposing effects of active contraction of levator muscle. Studies of the effect of such phenomena require incorporation of muscle active contraction into the material constitutive equation. However, this was beyond the scope of this dissertation.

Additionally, other limitations in this dissertation include is some conclusions being drawn from experimental tests on relatively few squirrel monkey specimens. The issue of specimen availability came from budget constraints and availability.

In summary, this dissertation fill several gaps in the existing literature: (1) The effect of term pregnancy on the viscosity and nonlinear elasticity of the pelvic floor tissues; and (2) Accurate constitutive equations of the pelvic floor tissues required

by computer modeling. The dissertation also extends and improves existing studies on: (1) Energetics of the second stage of labor under realistic intrauterine pressures; and (2) Providing a more accurate anatomically realistic finite element model of the second stage of labor. Despite the limitations, we believe this dissertation captures many of the important features of the second stage of labor and the mechanisms underlying pelvic floor dysfunction, and the results support the working hypothesis proposed in Chapter 1.

CHAPTER XI

Conclusions

The major findings in this dissertation are as follows:

- Pregnancy makes the rat vaginal tissue not only more compliant but also more viscous to aid stress relaxation. Pregnancy increases both the ultimate tensile strain and the Cauchy stress at failure. Fiber orientation affects the nonlinear elasticity, but not the viscosity, of the tissue (Chapter II).

- Pregnancy significantly changes the relaxation behavior of the levator ani muscle of squirrel monkey, but the effect on the tissue stiffness was not significant. This conclusion is based on a limited number of specimens (Chapter III).

- The mechanical properties of the female human levator ani muscle and perineal body are anisotropic, nonlinearly elastic, and time-dependent. Using a nonlinear optimization approach, it was possible to use a unified constitutive equation to fit the experimental data without separately regressing on the ramp and relaxation data. The constitutive equation obtained is easy to implement in commercial finite element codes (Chapter IV).

- The *Peak* volitional pushing style is most efficient in keeping the second stage of labor as short as possible and at the same time requiring as little maternal effort as possible. The *Triple* style is the least efficient. Labor duration is

very sensitive to the volitional pushing magnitude; decreasing magnitude has a greater effect than increasing magnitude. The volitional pushes should be timed to be as close to the peak of uterine contraction as possible in order to obtain maximal pushing efficacy (Chapter V).

- Considering the effect of material properties, the duration of the second stage of labor is most sensitive to the pelvic floor tissue stiffness, followed by the long-term relaxation behavior. It is relatively insensitive to the short-term relaxation behavior (Chapter VI).

- In the absence of concern for fetal well being, continuous vacuum extraction with a high traction force is a non-optimal strategy for facilitating delivery, since the increase in the risk for maternal muscle injury outweighs the benefit of reduced labor duration. However, high vacuum traction force combined with an intermittent pulling pattern coordinated with maternal effort helps to facilitate delivery with an acceptable risk of maternal muscle injury (Chapter VII).

- Increasing volitional pushing magnitude does not necessarily reduce the duration of the second stage of labor as might be imagined. This is due to the early occurrence of maternal muscle fatigue associated with high contraction intensity. With maternal fatigue being taken into consideration, the *Peak* style is the most efficient, and the *Triple* style is the least efficient strategy for volitional pushing. Maternal muscle fatigue is predicted to be relatively insensitive to the interval between two consecutive volitional pushes within one uterine contraction (Chapter VIII).

- The stretch of the levator hiatus during the second stage of labor is inhomogeneous. For the fetal head size and shape examined, the average stretch ratio of the hiatus is 3.55, with the highest principal stretch (5.04) being at the enthesis of the pubovisceral muscle, and the second highest stretch (4.15) being in the

perineal body region. When fetal head deflection is delayed beyond an optimal 'flexing point' where the occipital bone reaches the most inferior point of the pubic bone, there is a marked increase in the risk of pubovisceral muscle injury. Decreasing the perineal body stiffness helps mitigate the peak principal stretch and stress at the enthesis of the pubovisceral muscle, thereby reducing the risk of injury there. An occipito-posterior presentation of the fetal head induces higher stretch in the levator ani muscle than an occipito-anterior presentation (Chapter IX).

CHAPTER XII

Suggestions for Future Works

This dissertation provides several insights into the biomechanics of the processes involved in the second stage of labor, and the mechanisms underlying pelvic floor dysfunction. It also provides some suggestions to obstetrical professionals in optimizing volitional pushing strategy and vacuum extraction operation, in order to facilitate delivery while at the same time keeping maternal muscle injuries better prevented. However, several limitations of current study and some related factors remaining to be investigated warrant further studies as follows:

- *Combining anatomically accurate geometries with clinically recorded realistic intrauterine pressure profile in finite element model*: The second stage of labor is a dynamic process, and the pelvic floor tissues exhibit time-dependent mechanical behavior. Therefore, static loadings, such as prescribing pre-assumed displacement or velocity that widely used in existing models, fails to predict the dynamic stretch of the pelvic floor tissues, therefore weakening the usefulness of the model in unveiling the mechanisms underlying pelvic floor dysfunction.

- *Incorporate the deformation of the fetal head in the birth model*: During the second stage of birth, the fetal head undergoes a molding process when passing through the birth canal, and that process affect the stretch of the pelvic floor tissues. Also, vacuum extraction, acting directly on fetal head, may induce not

only maternal perineal lacerations but also fetal morbidity. All these factors warrant incluiding a deformable fetal head in the finite element model.

- *Taking into consideration active muscle contraction into the constitutive equation*: Since inadvertent volitional contraction of levator ani muscle by the woman can increase the stress level in the muscle, it may increase the risk potential of muscle injury. Therefore, to better understand the mechanisms underlying pelvic floor dysfunction, it is necessary to incorporate active contraction to the material model.

- *Acquiring more tissue specimens in order to reach more statistically definitive conclusions*: For the reason of expense, the number of squirrel monkey specimens used in this dissertation is limited. To draw statistically definitive conclusions, more tests on monkey specimens are necessary. The same situation applies to testing on the human pelvic floor tissues. Testing more human specimen helps increase the accuracy, and therefore the usefulness for computer modeling, of the constitutive equations developed in this dissertation. Also, it is helpful to collect some surrounding connective tissues that the levator ani muscle attaches to, such as sacrospinous ligaments and ATLA. Knowledge of the mechanical properties of these connective tissues helps improve the boundary conditions in the finite element model.

APPENDICES

APPENDIX A

Design of a Biaxial Tension Test System for Biological Soft Tissues

1. Overview of the test system

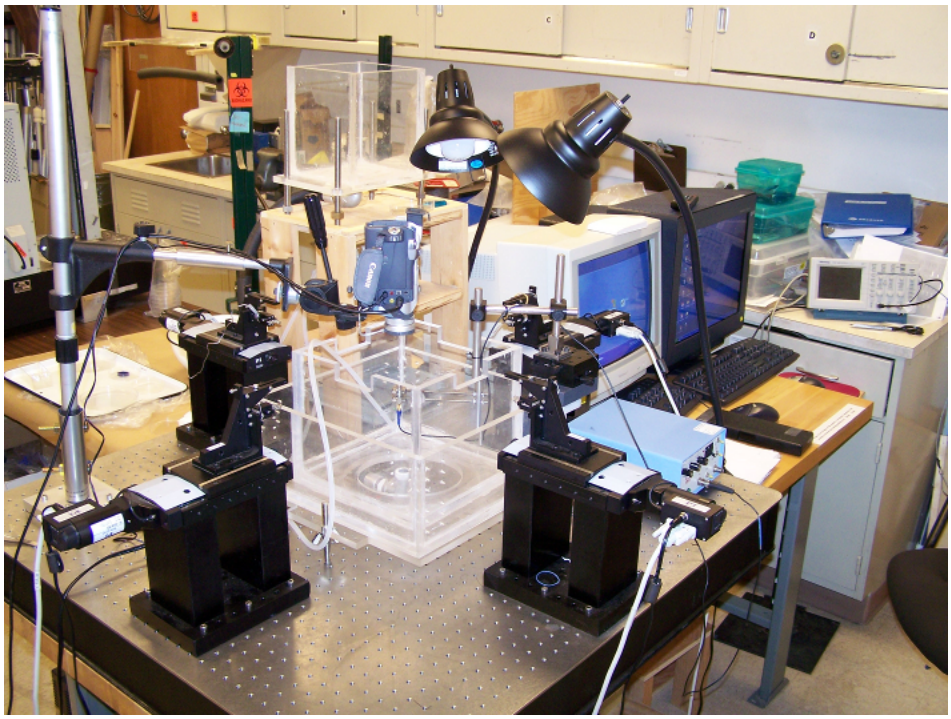

Figure A.1: Biaxial tension test system

In order to measure anisotropic mechanical properties of soft tissues, a biaxial tension test system was designed and assembled (Figure A.1). With this device, various 2-D stretching modes can be implemented on thin tissue specimens, therefore anisotropic material properties of soft tissues can be fully characterized and sound constitutive laws suitable for computer modeling can be derived.

Based functions, the test system can be divided into five modules: specimen fixation, force acquisition, motion control, image capture, and ultrasound measuring. Two P4 3.2GHz computers are used to synchronize data acquisition, motion contol and image capturing with triggering TTL signals. Using National Instrument LabVIEW V8.0, a user-friendly interface software was developed for implementing various test protocols.

2. Specimen fixation

To avoid mechanical interference with the deformation of specimen incurred by using gripping clamps, the thin specimen is mounted to test device in a trampoline-like fashion using three or four sutures on each edge of the specimen so that the specimen can freely expand along the four lateral directions (Figure A.2). Compared with the size of specimens, the sutures are long enough to ensure that the sutures of same specimen edge are almost parallel to each other and therefore

their tension forces are applied perpendicular to the edge.

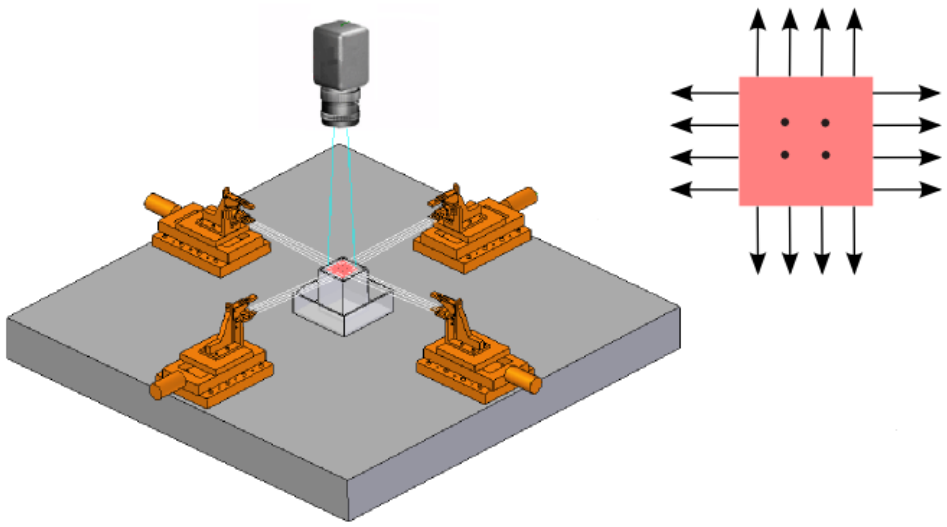

Figure A.2: Fixation of thin tissue specimen in a biaxial tension test

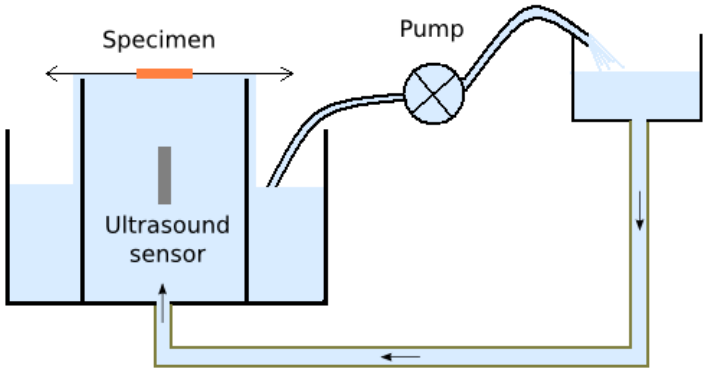

Figure A.3: Saline solution circulation system

The specimen floats on the surface of isotonic saline solution circulated in a acryl tank, which is a part of a closed liquid circulation system (Figure A.3). Driven by a variable-speed peristalic pump (Model 3389, Control Company Inc.), saline solution flows continuously inside the circulation system so that a layer of liquid film forms at the edge of

the tank to remove frictional interference to sutures. Saline solution serves three purposes: (1) culturing the tissue specimen to prevent dehydration; (2) providing buoyant support to specimen; (3) Providing transmitting media for ultrasound signal emitted from a transducer submersed in the solution for measuring specimen thickness.

3. Motion control

Synchronized and smooth stretching of specimen along two perpendicular directions are realized by four orthogonally oriented motion control axes, each of which consists of a PI M405PD precision translational stage driven by a servo motor, and a PI ActiveDriveTM PWM servo-amplifier. All axes are controled together by a PI PCI-C843.41 multi-axis motion controller installed in a PC computer. Along each stretching direction, the stretching range is 100 mm with resolution of 0.15 μm, and the stretching rate can reach up to 30 mm/second.

4. Force acquisition

Along each of the two orthogonal stretching directions, there is a precision miniature loadcell (model 31, Honeywell Inc.) to record stretching force, which is then acquired into computer through one 12-bit NI PCI-6023E DAQ board. The load limit is 10 pounds with resolution of $10/2^{12} = 0.0024$ pound.

5. Non-contact measurement of 2-D strain

To avoid mechanical interference with the tissue deformation, non-contact method is used to measure 2-D strain at the center of the specimen. On the surface of the specimen four dark dots are marked in the central area (Figure A.2). A camcorder (Canon Optura 20) is used to track the spatial excursions of these markers, and an image capturing card (NI PCI-1411) is used to acquire video frames and save them to a sequence of image files in a computer for offline image analyses. On each frame of the saved image, the boundaries of the contrast markers are thresheld so that the coordinates of their centroids are tracked over time. Using the basic theory of deformation kinematics in continuum mechanics, the 2-D strain tensor at the point of interest (the center point) can be calculated from the tracked displacement history of markers. A code developed with NI Vision V8.2 is used to automatically implement the image capture and analysis.

The image acquisition is synchronized with force acquisition at a capturing frequency of up to 30 fps, and the captured image can be either grayscale or 32-bit RGB/HSL with resolution of 640×480 pixels.

6. Ultrasound measurement of specimen thickness

An ultrasound transducer (Panametrics-NDT, model V316-SM) submersed in saline solution right beneath the specimen is used to dynam-

ically measure the tissue thickness.

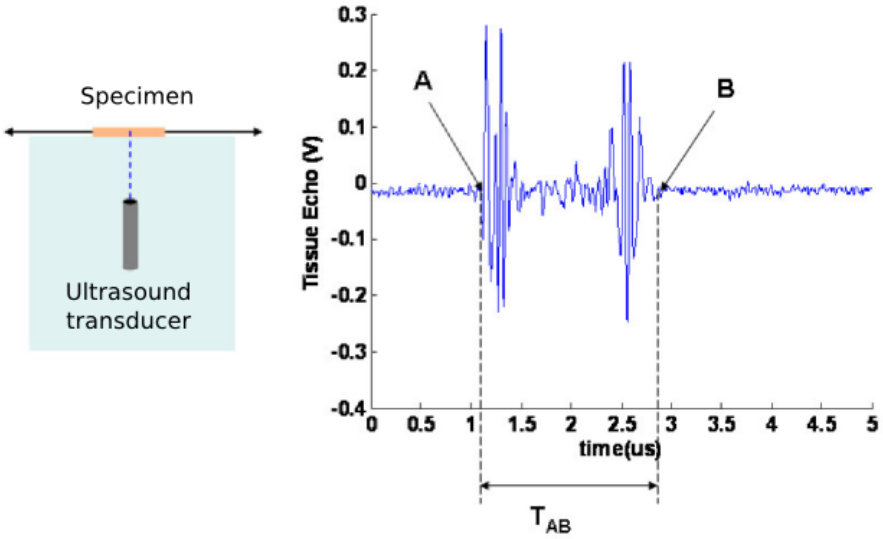

Figure A.4: Ultrasonic measurement of specimen thickness

The basic principle is that the transducer continuously send out ultrasound signals which transmit upward and hit the front and back surfaces of the tissue specimen successively, and the echoes generate two pulses on the signal display (as shown in Figure A.4). The thickness of the specimen can be calculated as following

$$\text{Specimen thickness} = \frac{T_{AB} \times C}{2} \tag{A.1}$$

where T_{AB} is the time difference between the two pulses, and C is the the ultrasound speed in the tissue, which is approximately equal to 1.5×10^3 mm/second.

Two kinds of thickness information can be measured using ultrasound. On the one hand, before the start of test, the ultrasound trans-

ducer, mounted on a manually adjusted linear stage, is moved along the two symmetric center lines of the specimen and records a series of points on the moving paths. In this way, the initial cross-sectional area normal to the two stretching directions can be evaluated, which are necessary for computing nominal stresses. On the other hand, during the test, the transducer stays still right beneath the center of the specimen to dynamically monitor the change of tissue thickness.

A pulser-receiver (Panametrics-NDT 5072PR) generates pulses to excite the transducer, and also receives echoing pulses from the transducer. The output signals from pulser-receiver are converted to signals suitable for computer acquisition using a high-speed digitizer (NI PCI-5112). The frequency of the ultrasound signal is 20 MHz and the resolution of measured thickness is 0.1 mm.

APPENDIX B

Derivations of Strain and Stress from a Biaxial Tension Test

1. Kinematics of a biaxial test

In biaxial tension test, a thin slab of specimen is stretched symmetrically by four forces applied on and normal to the four edges. The common mathematical method used for extracting strain and stress information follows the approaches outlined by *Humphrey, Vawter, and Vito* (1987), *Sacks* (2000), and *Sacks and Sun* (2003). If the central target region of the specimen is small compared with the specimen size and located away from the outer edges, then the strain and stress fields in the central target region can be considered as homogeneous (i.e., independent of position). In this case, the deformation field of the target

region can be expressed as

$$\begin{bmatrix} x_1 \\ x_2 \\ x_3 \end{bmatrix} = \begin{bmatrix} \lambda_1 & \kappa_1 & 0 \\ \kappa_2 & \lambda_2 & 0 \\ 0 & 0 & \lambda_3 \end{bmatrix} \begin{bmatrix} X_1 \\ X_2 \\ X_3 \end{bmatrix} \tag{B.1}$$

where the indices 1 and 2 denote in-plane directions whereas 3 denotes out-of-plane. $\mathbf{X} = [X_1, X_2, X_3]^T$ and $\mathbf{x} = [x_1, x_2, x_3]^T$ are locations of material particles in the reference (undeformed) and deformed configurations respectively, λ_i's are stretch ratios and κ_i's are in-plane shears. The deformation gradient tensor $\mathbf{F}$ is

$$\mathbf{F} = \frac{\partial \mathbf{x}}{\partial \mathbf{X}} = \begin{bmatrix} \lambda_1 & \kappa_1 & 0 \\ \kappa_2 & \lambda_2 & 0 \\ 0 & 0 & \lambda_3 \end{bmatrix} \tag{B.2}$$

$\mathbf{F}$ is a fundamental quantity in continuum mechanics, from which various strain measures required for constitutive law can be calculated. For example, the Green-Lagrange strain tensor $\mathbf{E}$ is widely used as the finite strain measure for forming constitutive laws of soft tissues due to

simplicity, which can be calculated as following

$$\mathbf{C} = \mathbf{F}^T \cdot \mathbf{F} \quad \text{(Right Cauchy-Green deformation tensor)} \tag{B.3}$$

$$\mathbf{E} = (\mathbf{C} - \mathbf{I})/2 \tag{B.4}$$

where $\mathbf{I}$ is identity tensor.

Generally soft tissues, with high fraction of water in their constituents, are assumed to be incompressible, then we have

$$\det F = 1 \quad \Longrightarrow \quad \lambda_3 = \frac{1}{\lambda_1 \lambda_2 - \kappa_1 \kappa_2} \tag{B.5}$$

So, as long as λ_1, λ_2, κ_1 and $\kappa 2$ are known, all components of $\mathbf{F}$ are determined, then the components of strain $\mathbf{E}$ can be computed directly

$$\begin{aligned} E_{11} &= \frac{1}{2}(\lambda_1^2 + \kappa_2^2 - 1) \\ E_{22} &= \frac{1}{2}(\lambda_2^2 + \kappa_1^2 - 1) \\ E_{12} &= \frac{1}{2}(\lambda_1 \kappa_1 + \lambda_2 \kappa_2) \end{aligned} \tag{B.6}$$

For thin slab of specimens, our interest focuses on in-plane strain and stress quantities, therefore out-of-plane components of all vectors (position, displacement) and tensors (deformation gradient, strains, and stresses) are ignored.

2. Measuring strains

To avoid mechanical interference with the deformation of specimen, the in-plane strain is measured optically with a video camera which tracks the positions over time of the four dots marked on the upper specimen surface. A matlab code was developed to extract the in-plane displacement vectors $\mathbf{u}^{(m)}(t) = \mathbf{x}^{(m)}(t) - \mathbf{X}^{(m)}$, $m = 1, 2, 3, 4$, of these dots by analyzing a series of recorded images. Then, the displacement field in the central target region (demarcated by the four markers) can be determined using bilinear interpolation

$$\begin{aligned} \mathbf{u}(\xi, \eta) &= \sum_{m=1}^{4} N_m(\xi, \eta)\mathbf{u}^{(m)} \\ \text{or} \qquad u_i &= \sum_{m=1}^{4} N_m(\xi, \eta)u_i^{(m)}, \qquad i = 1, 2 \end{aligned} \tag{B.7}$$

where $u_i^{(m)}$ is the ith-component of the displacement vector of the m-th marker, recorded by the video camera. N_m's are standard finite element shape functions

$$N_m(\xi, \eta) = \frac{1}{4}\left(1 + \xi_m\xi\right)\left(1 + \eta_m\eta\right), \qquad m = 1, 2, 3, 4 \tag{B.8}$$

with $\boldsymbol{\xi} = (\xi, \eta)$ being the mapping coordinates ($-1 \leq \xi, \eta \leq 1$). The mapping coordinates of the four markers are list in Table B.1

Table B.1: Mapping coordinates of four markers in $\boldsymbol{\xi}$-space

m	1	2	3	4
ξ_m	-1	-1	1	1
η_m	-1	1	1	-1

The shape function maps the quadrilateral region demarcated by instantaneous marker positions into a unit square region (Figure B.1)

$$\begin{aligned} \mathbf{X}(\xi,\eta) &= \sum_{m=1}^{4} N_m(\xi,\eta)\mathbf{X}^{(m)} \\ \text{or} \qquad X_i &= \sum_{m=1}^{4} N_m(\xi,\eta)X_i^{(m)}, \qquad i=1,2 \end{aligned} \tag{B.9}$$

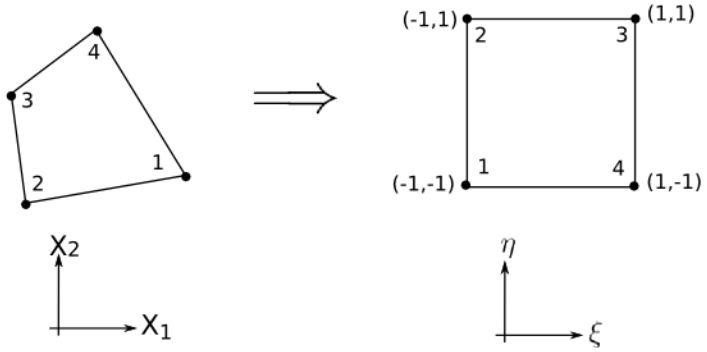

Figure B.1: Mapping of the positions of the four markers from the real coordinates (x_1, x_2) to the mapping coordinates (ξ, η).

Then, the deformation gradient tensor $\mathbf{F}$ can be computed by

$$\mathbf{F} = \begin{bmatrix} \lambda_1 & \kappa_1 \\ \kappa_2 & \lambda_2 \end{bmatrix} = \frac{\partial \mathbf{x}}{\partial \mathbf{X}} = \mathbf{I} + \frac{\partial \mathbf{u}}{\partial \mathbf{X}} = \begin{bmatrix} 1 & 0 \\ 0 & 1 \end{bmatrix} + \begin{bmatrix} \frac{\partial u_1}{\partial X_1} & \frac{\partial u_1}{\partial X_2} \\ \frac{\partial u_2}{\partial X_1} & \frac{\partial u_2}{\partial X_2} \end{bmatrix} \tag{B.10}$$

Defining Jacob matrix $\mathbf{J}$ by

$$\begin{Bmatrix} \frac{\partial}{\partial \xi} \\ \frac{\partial}{\partial \eta} \end{Bmatrix} = \begin{bmatrix} \frac{\partial X_1}{\partial \xi} & \frac{\partial X_2}{\partial \xi} \\ \frac{\partial X_1}{\partial \eta} & \frac{\partial X_2}{\partial \eta} \end{bmatrix} \begin{Bmatrix} \frac{\partial}{\partial X_1} \\ \frac{\partial}{\partial X_2} \end{Bmatrix} = \mathbf{J} \begin{Bmatrix} \frac{\partial}{\partial X_1} \\ \frac{\partial}{\partial X_2} \end{Bmatrix} \tag{B.11}$$

then we have

$$\mathbf{F} = \mathbf{I} + \frac{\partial \mathbf{u}}{\partial \mathbf{X}} = \mathbf{I} + \frac{\partial \mathbf{u}}{\partial \boldsymbol{\xi}} \left[\mathbf{J}^{-1}\right]^T \tag{B.12}$$

The components of matrix $\partial \mathbf{u}/\partial \boldsymbol{\xi}$ can be calculated by differentiating equation (B.7)

$$\begin{aligned} \frac{\partial u_i}{\partial \xi} &= \frac{1}{4}(1-\eta)(u_i^{(4)} + u_i^{(3)} - u_i^{2)} - u_i^{(1)}), \qquad i = 1, 2 \\ \frac{\partial u_i}{\partial \eta} &= \frac{1}{4}(1-\xi)(u_i^{(3)} + u_i^{(2)} - u_i^{(4)} - u_i^{(1)}), \qquad i = 1, 2 \end{aligned} \tag{B.13}$$

Similarly, the components of Jacob matrix $\mathbf{J} = [\partial \mathbf{X}/\partial \boldsymbol{\xi}]^T$ can be calculated by differentiating equation (B.9)

$$\begin{aligned} \frac{\partial X_i}{\partial \xi} &= \frac{1}{4}(1-\eta)(X_i^{(4)} + X_i^{(3)} - X_i^{2)} - X_i^{(1)}), \qquad i = 1, 2 \\ \frac{\partial X_i}{\partial \eta} &= \frac{1}{4}(1-\xi)(X_i^{(3)} + X_i^{(2)} - X_i^{(4)} - X_i^{(1)}), \qquad i = 1, 2 \end{aligned} \tag{B.14}$$

where $X_i^{(m)}$ is the ith-coordinate of the initial (undeformed) position of the m-th marker.

Using equation (B.12), the deformation gradient $\mathbf{F}$ at the center of the specimen, where $\xi = \eta = 0$, can be expressed in terms of the initial position of the four markers $\mathbf{X}_i$, and their current displacements $\mathbf{u}_i$, where $i = 1, 2, 3, 4$. In other words, the components of $\mathbf{F}$, λ_1, λ_2, κ_1, and κ_2, can be expressed in terms of initial position coordinates and current displacement values of the four markers.

For simplicity, Humphrey used a real-time average approach to approximately calculate the stretch ratios at the center of the specimen (*Humphrey et al.*, 1987)

$$\begin{aligned}
\lambda_1(t) &= \frac{1}{2}\frac{\left[x_1^{(4)}(t) - x_1^{(1)}(t)\right] + \left[x_1^{(3)}(t) - x_1^{(2)}(t)\right]}{\left[X_1^{(4)} - X_1^{(1)}\right] + \left[X_1^{(3)} - X_1^{(2)}\right]} \\
\lambda_2(t) &= \frac{1}{2}\frac{\left[x_1^{(3)}(t) - x_1^{(4)}(t)\right] + \left[x_1^{(2)}(t) - x_1^{(1)}(t)\right]}{\left[X_1^{(3)} - X_1^{(4)}\right] + \left[X_1^{(2)} - X_1^{(1)}\right]}
\end{aligned} \tag{B.15}$$

where $X_i^{(m)}$ and $x_i^{(m)}(t)$ are the i-th component of the initial and current position vectors of the m-th marker. Here, the shearing components were ignored for symmetric biaxial test. Humphrey also showed that strains from the simplified real-time average agreed well the bilinearly-interpolated strains.

3. Measuring stresses

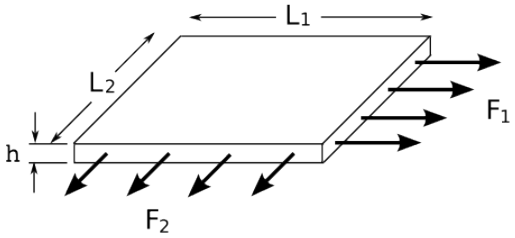

Figure B.2: Biaxial stretch of thin tissue specimen

Consider a rectangular thin slab of specimen and suppose the suture forces along the two orthogonal directions are F_1 and F_2 respectively (Figure B.2), then the straightforward stress measure is the 1st Piola-Kirchoff stress tensor, which is computed as

$$\mathbf{P} = \begin{bmatrix} P_{11} & 0 & 0 \\ 0 & P_{22} & 0 \\ 0 & 0 & 0 \end{bmatrix} \qquad \text{where} \begin{cases} P_{11} = \dfrac{F_1}{hL_2} \\ P_{22} = \dfrac{F_2}{hL_1} \end{cases} \tag{B.16}$$

Combining with the deformation gradient $\mathbf{F}$, the two most widely used stress measures for constitutive laws can be determined

$$\text{Cauchy stress tensor:} \quad \boldsymbol{\sigma} = J^{-1}\mathbf{P}\mathbf{F}^T = \frac{1}{J}\begin{bmatrix} \lambda_1 P_{11} & \kappa_2 P_{11} & 0 \\ \kappa_1 P_{22} & \lambda_2 P_{22} & 0 \\ 0 & 0 & 0 \end{bmatrix} \tag{B.17}$$

2nd Piola-Kirchoff stress tensor: $$\mathbf{S} = F^{-1}\mathbf{P} = \frac{1}{J}\begin{bmatrix} P_{11}\lambda_2\lambda_3 & -P_{22}\kappa_1\lambda_3 & 0 \\ -P_{11}\kappa_2\lambda_3 & P_{22}\lambda_1\lambda_3 & 0 \\ 0 & 0 & 0 \end{bmatrix} \tag{B.18}$$

BIBLIOGRAPHY

BIBLIOGRAPHY

ABAQUS (2008), *Abaqus theory manual, version 6.8*, SIMULIA Inc.

Abramowitch, S. D., and S. L. Woo (2004), An improved method to analyze the stress relaxation of ligaments following a finite ramp time based on the quasi-linear viscoelastic theory., *Journal of Biomechanical Engineering*, *126*(1), 92–7.

ACOG (2000), Operative vaginal delivery, *American College of Obstetricians and Gynecologists Practice Bulletin, Clinical Management Guidelines for Obstetrician-Gynecologists*, (17).

Altman, M. R., and M. T. Lydon-Rochelle (2006), Prolonged second stage of labor and risk of adverse maternal and perinatal outcomes: a systematic review., *Birth (Berkeley, Calif.)*, *33*(4), 315–22, doi: 10.1111/j.1523-536X.2006.00129.x.

Angioli, R., O. Gómez-Marín, G. Cantuaria, and M. J. O'sullivan (2000), Severe perineal lacerations during vaginal delivery: the university of miami experience., *Am. J. Obstet. Gynecol.*, *182*(5), 1083–5.

Ashton-Miller, J. A., and J. O. L. Delancey (2009), On the biomechanics of vaginal birth and common sequelae., *Annual Review of Biomedical Engineering*, *11*, 163–76, doi:10.1146/annurev-bioeng-061008-124823.

Ashton-Miller, J. A., D. Howard, and J. O. DeLancey (2001), The functional anatomy of the female pelvic floor and stress continence control system., *Scandinavian Journal of Urology And Nephrology. Supplementum*, (207), 1–7; discussion 106–25.

Bailey, A. J., R. G. Paul, and L. Knott (1998), Mechanisms of maturation and ageing of collagen., *Mech. Ageing Dev.*, *106*(1-2), 1–56.

Bauer, M., E. Mazza, M. Jabareen, L. Sultan, M. Bajka, U. Lang, R. Zimmermann, and G. A. Holzapfel (2009), Assessment of the in vivo biomechanical properties of the human uterine cervix in pregnancy using the aspiration test: a feasibility study., *Eur. J. Obstet. Gynecol. Reprod. Biol.*, *144 Suppl 1*, S77–81, doi: 10.1016/j.ejogrb.2009.02.025.

Bellinger, A. M., et al. (2008), Remodeling of ryanodine receptor complex causes "leaky" channels: a molecular mechanism for decreased exercise capacity., *Proc. Natl. Acad. Sci. U.S.A.*, *105*(6), 2198–202, doi:10.1073/pnas.0711074105.

Bofill, J. A., O. A. Rust, S. J. Schorr, R. C. Brown, R. W. Martin, J. N. Martin, and J. C. Morrison (1996), A randomized prospective trial of the obstetric forceps versus the m-cup vacuum extractor., *Am. J. Obstet. Gynecol.*, *175*(5), 1325–30.

Bofill, J. A., O. A. Rust, S. J. Schorr, R. C. Brown, W. E. Roberts, and J. C. Morrison (1997), A randomized trial of two vacuum extraction techniques., *Obstet Gynecol*, *89*(5 Pt 1), 758–62.

Brooks, S. V., and J. A. Faulkner (2001), Severity of contraction-induced injury is affected by velocity only during stretches of large strain., *J. Appl. Physiol.*, *91*(2), 661–6.

Brooks, S. V., E. Zerba, and J. A. Faulkner (1995), Injury to muscle fibres after single stretches of passive and maximally stimulated muscles in mice., *J. Physiol. (Lond.)*, *488 (Pt 2)*, 459–69.

Buhimschi, C. S., I. A. Buhimschi, A. M. Malinow, and C. P. Weiner (2004a), Intrauterine pressure during the second stage of labor in obese women., *Obstetrics and Gynecology*, *103*(2), 225–30, doi: 10.1097/01.AOG.0000102706.84063.C7.

Buhimschi, I. A., L. Dussably, C. S. Buhimschi, A. Ahmed, and C. P. Weiner (2004b), Physical and biomechanical characteristics of rat cervical ripening are not consistent with increased collagenase activity., *Am. J. Obstet. Gynecol.*, *191*(5), 1695–704, doi: 10.1016/j.ajog.2004.03.080.

Calvo, B., E. Peña, P. Martins, T. Mascarenhas, M. Doblaré, R. M. Natal Jorge, and A. Ferreira (2009), On modelling damage process in vaginal tissue., *Journal of Biomechanics*, *42*(5), 642–51, doi: 10.1016/j.jbiomech.2008.12.002.

Carlan, S. J., L. Wyble, J. Lense, D. S. Mastrogiannis, and M. T. Parsons (1991), Fetal head molding. diagnosis by ultrasound and a review of the literature., *Journal of Perinatology : Official Journal of the California Perinatal Association*, *11*(2), 105–11.

Caughey, A. B., P. L. Sandberg, M. G. Zlatnik, M.-P. Thiet, J. T. Parer, and R. K. Laros (2005), Forceps compared with vacuum: rates of neonatal and maternal morbidity., *Obstet Gynecol*, *106*(5 Pt 1), 908–12, doi:10.1097/01.AOG.0000182616.39503.b2.

Chen, L., J. A. Ashton-Miller, and J. O. L. DeLancey (2009), A 3d finite element model of anterior vaginal wall support to evaluate mechanisms underlying cystocele formation., *Journal of Biomechanics*, *42*(10), 1371–7, doi:10.1016/j.jbiomech.2009.04.043.

Cheng, Y. W., L. M. Hopkins, and A. B. Caughey (2004), How long is too long: Does a prolonged second stage of labor in nulliparous women affect maternal and neonatal outcomes?, *Am. J. Obstet. Gynecol.*, *191*(3), 933–8, doi:10.1016/j.ajog.2004.05.044.

Chitty, L. S., D. G. Altman, A. Henderson, and S. Campbell (1994), Charts of fetal size: 2. head measurements., *British Journal of Obstetrics and Gynaecology*, *101*(1), 35–43.

Christianson, L. M., V. E. Bovbjerg, E. C. McDavitt, and K. L. Hullfish (2003), Risk factors for perineal injury during delivery., *Am. J. Obstet. Gynecol.*, *189*(1), 255–60.

Conrad, J. T., and K. Ueland (1976), Reduction of the stretch modulus of human cervical tissue by prostaglandin e2., *Am. J. Obstet. Gynecol.*, *126*(2), 218–23.

Conrad, J. T., and K. Ueland (1979), The stretch modulus of human cervical tissue in spontaneous, oxytocin-induced, and prostaglandin e2-induced labor., *Am. J. Obstet. Gynecol.*, *133*(1), 11–4.

Cunningham, F., K. Leveno, S. Bloom, J. Hauth, L. Gilstrap, and K. Wenstrom (2005), *Williams Obstetrics*, 22 ed., McGraw-Hill Professional.

d'Aulignac, D., J. A. C. Martins, E. B. Pires, T. Mascarenhas, and R. M. N. Jorge (2005), A shell finite element model of the pelvic floor muscles., *Computer Methods in Biomechanics and Biomedical Engineering*, *8*(5), 339–47, doi:10.1080/10255840500405378.

DeLancey, J. O. (1986), Correlative study of paraurethral anatomy., *Obstetrics and Gynecology*, *68*(1), 91–7.

DeLancey, J. O. (1988), Structural aspects of the extrinsic continence mechanism., *Obstetrics and gynecology*, *72*(3 Pt 1), 296–301.

DeLancey, J. O. (1994), Structural support of the urethra as it relates to stress urinary incontinence: the hammock hypothesis., *Am. J. Obstet. Gynecol.*, *170*(6), 1713–20; discussion 1720–3.

DeLancey, J. O. L. (1989), Pubovesical ligament - a separate structure from the urethral supports (pubo-urethral ligaments), *Neurourology and Urodynamics*, *8*(1), 53–61.

DeLancey, J. O. L., R. Kearney, Q. Chou, S. Speights, and S. Binno (2003), The appearance of levator ani muscle abnormalities in magnetic resonance images after vaginal delivery., *Obstetrics and Gynecology*, *101*(1), 46–53.

Demissie, K., G. G. Rhoads, J. C. Smulian, B. A. Balasubramanian, K. Gandhi, K. S. Joseph, and M. Kramer (2004), Operative vaginal delivery and neonatal and infant adverse outcomes: population based retrospective analysis., *BMJ*, *329*(7456), 24–9, doi:10.1136/bmj.329.7456.24.

Dietz, H. P., and V. Lanzarone (2005), Levator trauma after vaginal delivery., *Obstetrics and Gynecology*, *106*(4), 707–12, doi:10.1097/01.AOG.0000178779.62181.01.

Digonnet, L., J. Cahn, J. Roy, and J. Boucet (1952), Effect of local injection of hyaluronidase on perineal distention in labor in primiparas., *Therapie*, *7*(5), 388–91.

Downing, S. J., and O. D. Sherwood (1986), The physiological role of relaxin in the pregnant rat. iv. the influence of relaxin on cervical collagen and glycosaminoglycans., *Endocrinology*, *118*(2), 471–9.

Foldspang, A., S. Mommsen, G. W. Lam, and L. Elving (1992), Parity as a correlate of adult female urinary incontinence prevalence., *Journal of Epidemiology and Community Health*, *46*(6), 595–600.

Fraser, W. D., S. Marcoux, I. Krauss, J. Douglas, C. Goulet, and M. Boulvain (2000), Multicenter, randomized, controlled trial of delayed pushing for nulliparous women in the second stage of labor with continuous epidural analgesia. the people (pushing early or pushing late with epidural) study group., *Am. J. Obstet. Gynecol.*, *182*(5), 1165–72.

Fung, Y. C. (1967), Elasticity of soft tissues in simple elongation, *American Journal of Physiology*, *28*, 1532–1544.

Fung, Y. C. (1972), Stress-strain history relations of soft tissues in simple elongation, in *Biomechanics: Its foundations and objectives*, edited by Y. C. Fung, pp. 181–207, Prentice Hall, Englewood Cliffs, NJ.

Fung, Y. C. (1973), Biorheology of soft tissues, *Biorheology*, *10*, 139–155.

Fung, Y. C. (1983), On the foundations of biomechanics, *Journal of Applied Mechanics*, *50*, 1003–1009.

Fung, Y. C. (1990), *Biomechanics: motion, flow, stress, and growth*, Springer.

Fung, Y. C. (1993), *Biomechanics: Mechanical Properties of Living Tissues*, 2 ed., Springer.

Gainey, H. L. (1943), Postpartum observation of pelvic tissue damage, *Am. J. Obstet. Gynecol.*, *45*, 457–466.

Garrett, W. E. (1996), Muscle strain injuries., *The American Journal of Sports Medicine*, *24*(6 Suppl), S2–8.

Gasser, T. C., R. W. Ogden, and G. A. Holzapfel (2006), Hyperelastic modelling of arterial layers with distributed collagen fibre orientations., *Journal of the Royal Society, Interface / the Royal Society*, *3*(6), 15–35, doi:10.1098/rsif.2005.0073.

Gent, A. (1996), A new constitutive relation for rubber, *Rubber Chemistry And Technology*, *69*, 59–61.

Hansen, S. L., S. L. Clark, and J. C. Foster (2002), Active pushing versus passive fetal descent in the second stage of labor: a randomized controlled trial., *Obstet Gynecol*, *99*(1), 29–34.

Holzapfel, G. A. (2000), *Nonlinear solid mechanics: A continuum approach for engineering*, John Wiley & Sons.

Holzapfel, G. A., T. C. Gasser, and R. W. Ogden (2000), A new constitutive framework for arterial wall mechanics and a comparative study of material models, *Journal of Elasticity*, *61*(Numbers 1-3), 1–48, doi:10.1023/A:1010835316564.

Hoyte, L., L. Schierlitz, K. Zou, G. Flesh, and J. R. Fielding (2001), Two- and 3-dimensional mri comparison of levator ani structure, volume, and integrity in women with stress incontinence and prolapse., *Am. J. Obstet. Gynecol.*, *185*(1), 11–9, doi:10.1067/mob.2001.116365.

Hoyte, L., M. Jakab, S. K. Warfield, S. Shott, G. Flesh, and J. R. Fielding (2004), Levator ani thickness variations in symptomatic and asymptomatic women using magnetic resonance-based 3-dimensional color mapping., *Am. J. Obstet. Gynecol.*, *191*(3), 856–61, doi:10.1016/j.ajog.2004.06.067.

Humphrey, J. D. (2003), Continuum biomechanics of soft biological tissues, *Royal Society of London Proceedings Series A*, *459*(2029), 3–46, doi:10.1098/rspa.2002.1060.

Humphrey, J. D., D. L. Vawter, and R. P. Vito (1987), Quantification of strains in biaxially tested soft tissues., *Journal of Biomechanics*, *20*(1), 59–65.

Iridiastadi, H., and M. Nussbaum (2006), Muscle fatigue and endurance during repetitive intermittent static efforts: development of prediction models, *Ergonomics*, *49*(4), 344–360, doi: 10.1080/00140130500475666.

Janda, S., F. C. T. van der Helm, and S. B. de Blok (2003), Measuring morphological parameters of the pelvic floor for finite element modelling purposes., *Journal of Biomechanics*, *36*(6), 749–57.

Johanson, R. B., and B. K. Menon (2000), Vacuum extraction versus forceps for assisted vaginal delivery., *Cochrane Database of Systematic Reviews (Online)*, (2), CD000,224, doi:10.1002/14651858.CD000224.

Johanson, R. B., C. Rice, M. Doyle, J. Arthur, L. Anyanwu, J. Ibrahim, A. Warwick, C. W. Redman, and P. M. O'Brien (1993), A randomised prospective study comparing the new vacuum extractor policy with forceps delivery., *British journal of obstetrics and gynaecology*, *100*(6), 524–30.

Kahn, M. A., and S. L. Stanton (1997), Posterior colporrhaphy: its effects on bowel and sexual function., *British Journal of Obstetrics and Gynaecology*, *104*(1), 82–6.

Kearney, R., J. M. Miller, J. A. Ashton-Miller, and J. O. L. DeLancey (2006), Obstetric factors associated with levator ani muscle injury after vaginal birth., *Obstetrics and Gynecology*, *107*(1), 144–9, doi: 10.1097/01.AOG.0000194063.63206.1c.

Klein, M. C. (2006), In the literature: pushing in the wrong direction., *Birth (Berkeley, Calif.)*, *33*(3), 251–3, doi:10.1111/j.1523-536X.2006.00111.x.

Knowles, J. (1977), The finite anti-plane shear field near the tip of a crack for a class of incompressible elastic solids, *Int. J. Fract.*, *13*, 611–639.

Kudish, B., S. Blackwell, S. G. Mcneeley, E. Bujold, M. Kruger, S. L. Hendrix, and R. Sokol (2006), Operative vaginal delivery and midline episiotomy: a bad combination for the perineum., *Am. J. Obstet. Gynecol.*, *195*(3), 749–54, doi:10.1016/j.ajog.2006.06.078.

Lawson, J. O. (1974), Pelvic anatomy. i. pelvic floor muscles., *Annals of the Royal College of Surgeons of England*, *54*(5), 244–52.

Lee, S.-L., A. Darzi, and G.-Z. Yang (2005), Subject specific finite element modelling of the levator ani., *Medical image computing and computer-assisted intervention : MICCAI ... International Conference on Medical Image Computing and Computer-Assisted Intervention*, *8*(Pt 1), 360–7.

Lee, S.-L., E. Tan, V. Khullar, W. Gedroyc, A. Darzi, and G.-Z. Yang (2009), Physical-based statistical shape modeling of the levator ani., *IEEE transactions on medical imaging*, *28*(6), 926–36, doi: 10.1109/TMI.2009.2012894.

Li, X., J. A. Kruger, J.-H. Chung, M. P. Nash, and P. M. F. Nielsen (2008), Modelling childbirth: comparing athlete and non-athlete pelvic floor mechanics., *Medical Image Computing And Computer-assisted Intervention : MICCAI ... International Conference on Medical Image Computing and Computer-Assisted Intervention*, *11*(Pt 2), 750–7.

Li, Z., J. E. Alonso, J.-E. Kim, J. S. Davidson, B. S. Etheridge, and A. W. Eberhardt (2006), Three-dimensional finite element models of the human pubic symphysis with viscohyperelastic soft tissues., *Annals of Biomedical Engineering*, *34*(9), 1452–62, doi:10.1007/s10439-006-9145-1.

Li, Z., J.-E. Kim, J. S. Davidson, B. S. Etheridge, J. E. Alonso, and A. W. Eberhardt (2007), Biomechanical response of the pubic symphysis in lateral pelvic impacts: a finite element study., *Journal of Biomechanics*, *40*(12), 2758–66, doi:10.1016/j.jbiomech.2007.01.023.

Lieber, R. L., and J. Fridén (1993), Muscle damage is not a function of muscle force but active muscle strain., *Journal of Applied Physiology*, *74*(2), 520–6.

Lien, K.-C., B. Mooney, J. O. L. DeLancey, and J. A. Ashton-Miller (2004), Levator ani muscle stretch induced by simulated vaginal birth., *Obstetrics and Gynecology*, *103*(1), 31–40, doi: 10.1097/01.AOG.0000109207.22354.65.

Lien, K.-C., J. O. L. DeLancey, and J. A. Ashton-Miller (2009), Biomechanical analyses of the efficacy of patterns of maternal effort on second-stage progress., *Obstetrics and Gynecology*, *113*(4), 873–80, doi:10.1097/AOG.0b013e31819c82e1.

Liu, J., R. Brown, and G. Yue (2002), A dynamical model of muscle activation, fatigue, and recovery, *Biophysical Journal*, *82*(5), 2344–2359, doi:10.1016/S0006-3495(02)75580-X.

Lucas, M. J. (1994), The role of vacuum extraction in modern obstetrics., *Clinical Obstetrics and Gynecology*, *37*(4), 794–805.

Mant, J., R. Painter, and M. Vessey (1997), Epidemiology of genital prolapse: observations from the oxford family planning association study., *British Journal of Obstetrics and Gynaecology*, *104*(5), 579–85.

Margulies, R. U., Y. Hsu, R. Kearney, T. Stein, W. H. Umek, and J. O. L. DeLancey (2006), Appearance of the levator ani muscle subdivisions in magnetic resonance images., *Obstetrics and Gynecology*, *107*(5), 1064–9, doi:10.1097/01.AOG.0000214952.28605.e8.

Martin, J. A., B. E. Hamilton, P. D. Sutton, S. J. Ventura, F. Menacker, S. Kirmeyer, M. L. Munson, and (2007), Births: final data for 2005., *National Vital Statistics Reports : From the Centers for Disease Control and Prevention, National Center for Health Statistics, National Vital Statistics System*, *56*(6), 1–103.

Martins, J. A. C., M. P. M. Pato, E. B. Pires, R. M. N. Jorge, M. Parente, and T. Mascarenhas (2007), Finite element studies of the deformation of the pelvic floor., *Ann. N. Y. Acad. Sci.*, *1101*, 316–34, doi:10.1196/annals.1389.019.

Mayberry, L. J., R. Hammer, C. Kelly, B. True-Driver, and A. De (1999), Use of delayed pushing with epidural anesthesia: findings from a randomized, controlled trial., *Journal of Perinatology : Official Journal of the California Perinatal Association*, *19*(1), 26–30.

Menticoglou, S. M., F. Manning, C. Harman, and I. Morrison (1995),

Perinatal outcome in relation to second-stage duration., *Am. J. Obstet. Gynecol.*, *173*(3 Pt 1), 906–12.

Moalli, P. A., N. S. Howden, J. L. Lowder, J. Navarro, K. M. Debes, S. D. Abramowitch, and S. L.-Y. Woo (2005), A rat model to study the structural properties of the vagina and its supportive tissues., *Am. J. Obstet. Gynecol.*, *192*(1), 80–8, doi:10.1016/j.ajog.2004.07.008.

Moon, J. M., C. V. Smith, and W. F. Rayburn (1990), Perinatal outcome after a prolonged second stage of labor., *The Journal of Reproductive Medicine*, *35*(3), 229–31.

Myles, T. D., and J. Santolaya (2003), Maternal and neonatal outcomes in patients with a prolonged second stage of labor., *Obstetrics and Gynecology*, *102*(1), 52–8.

Noakes, K. F., I. P. Bissett, A. J. Pullan, and L. K. Cheng (2006), Anatomically based computational models of the male and female pelvic floor and anal canal., *Conference Proceedings : ... Annual International Conference of the IEEE Engineering in Medicine and Biology Society. IEEE Engineering in Medicine and Biology Society. Conference*, *1*, 3815–8, doi:10.1109/IEMBS.2006.259886.

Noakes, K. F., I. P. Bissett, A. J. Pullan, and L. K. Cheng (2008a), Anatomically realistic three-dimensional meshes of the pelvic floor & anal canal for finite element analysis., *Annals of Biomedical Engineering*, *36*(6), 1060–71, doi:10.1007/s10439-008-9471-6.

Noakes, K. F., A. J. Pullan, I. P. Bissett, and L. K. Cheng (2008b), Subject specific finite elasticity simulations of the pelvic floor., *Journal of Biomechanics*, *41*(14), 3060–5, doi:10.1016/j.jbiomech.2008.06.037.

O'Day-Bowman, M. B., R. J. Winn, P. J. Dziuk, E. R. Lindley, and O. D. Sherwood (1991), Hormonal control of the cervix in pregnant gilts. iii. relaxin's influence on cervical biochemical properties in ovariectomized hormone-treated pregnant gilts., *Endocrinology*, *129*(4), 1967–76.

Oleary, J. A., and S. Erez (1965), Hyaluronidase as an adjuvant to episiotomy, *Obstetrics & Gynecology*, *26*(1), 66–69.

Olsen, A. L., V. J. Smith, J. O. Bergstrom, J. C. Colling, and A. L. Clark (1997), Epidemiology of surgically managed pelvic organ prolapse and urinary incontinence, *Obstetrics and Gynecology*, *89*(4), 501–6, doi:10.1016/S0029-7844(97)00058-6.

Orchard, J. (2002), Biomechanics of muscle strain injury.

Owiny, J. R., R. J. Fitzpatrick, D. G. Spiller, and H. Dobson (1991), Mechanical properties of the ovine cervix during pregnancy, labour and immediately after parturition, *Br. Vet. J.*, *147*(5), 432–6.

Parente, M. P. L., R. M. N. Jorge, T. Mascarenhas, A. A. Fernandes, and J. A. C. Martins (2008), Deformation of the pelvic floor muscles during a vaginal delivery, *International Urogynecology Journal and Pelvic Floor Dysfunction*, *19*(1), 65–71, doi:10.1007/s00192-007-0388-7.

Parente, M. P. L., R. M. N. Jorge, T. Mascarenhas, A. A. Fernandes, and J. A. C. Martins (2009a), The influence of an occipitoposterior malposition on the biomechanical behavior of the pelvic floor, *Eur. J. Obstet. Gynecol. Reprod. Biol.*, *144 Suppl 1*, S166–9, doi:10.1016/j.ejogrb.2009.02.033.

Parente, M. P. L., R. M. Natal Jorge, T. Mascarenhas, A. A. Fernandes, and J. A. C. Martins (2009b), The influence of the material properties on the biomechanical behavior of the pelvic floor muscles during vaginal delivery, *Journal of Biomechanics*, *42*(9), 1301–6, doi:10.1016/j.jbiomech.2009.03.011.

Petersen, L., and P. Besuner (1997), Pushing techniques during labor: issues and controversies, *Journal of Obstetric, Gynecologic, and Neonatal Nursing : JOGNN / NAACOG*, *26*(6), 719–26.

Read, C. P., R. A. Word, M. A. Ruscheinsky, B. C. Timmons, and M. S. Mahendroo (2007), Cervical remodeling during pregnancy and parturition: molecular characterization of the softening phase in mice., *Reproduction*, *134*(2), 327–40, doi:10.1530/REP-07-0032.

Rivlin, R. S., and D. W. Saunders (1952), Large elastic deformations of isotropic materials. vii. experiments on the deformation of rubber,

Philosophical Transactions of the Royal Society of London. Series A, Mathematical and Physical Sciences, *243*(865), 251–288.

Roberts, C. L., S. Torvaldsen, C. A. Cameron, and E. Olive (2004), Delayed versus early pushing in women with epidural analgesia: a systematic review and meta-analysis., *BJOG : an International Journal of Obstetrics And Gynaecology*, *111*(12), 1333–40.

Ryhammer, A. M., K. M. Bek, and S. Laurberg (1995), Multiple vaginal deliveries increase the risk of permanent incontinence of flatus urine in normal premenopausal women., *Dis. Colon Rectum*, *38*(11), 1206–9.

Sacks, M. (2000), Biaxial mechanical evaluation of planar biological materials, *Journal Of Elasticity*, *61*, 199–246.

Sacks, M., and W. Sun (2003), Multiaxial mechanical behavior of biological materials, *Annual Review Of Biomedical Engineering*, *5*, 251–284, doi:10.1146/annurev.bioeng.5.011303.120714.

Sauren, A. A., and E. P. Rousseau (1983), A concise sensitivity analysis of the quasi-linear viscoelastic model proposed by fung., *Journal of Biomechanical Engineering*, *105*(1), 92–5.

Sauren, A. A., M. C. van Hout, A. A. van Steenhoven, F. E. Veldpaus, and J. D. Janssen (1983), The mechanical properties of porcine aortic valve tissues., *Journal of Biomechanics*, *16*(5), 327–37.

Scarabotto, L. B., and M. L. G. Riesco (2008), Use of hyaluronidase to prevent perineal trauma during spontaneous delivery: a pilot study., *Journal of Midwifery & Women's Health*, *53*(4), 353–61, doi:10.1016/j.jmwh.2008.02.015.

Schiessl, B., W. Janni, K. Jundt, G. Rammel, U. Peschers, and F. Kainer (2005), Obstetrical parameters influencing the duration of the second stage of labor., *Eur. J. Obstet. Gynecol. Reprod. Biol.*, *118*(1), 17–20, doi:10.1016/j.ejogrb.2004.01.045.

Shobeiri, S. A., R. R. Chesson, and R. F. Gasser (2008), The internal innervation and morphology of the human female levator ani muscle., *Am. J. Obstet. Gynecol.*, *199*(6), 686.e1–6, doi:10.1016/j.ajog.2008.07.057.

Spencer, A. J. M. (1984), Constitutive theory for strongly anisotropic solids, in *Continuum theory of the mechanics of fiber-reinforced composites*, edited by A. Spencer, pp. 1–32, Springer-Verlag, cISM Courses and Lectures No.282.

Strohbehn, K., L. E. Quint, M. R. Prince, K. J. Wojno, and J. O. Delancey (1996), Magnetic resonance imaging anatomy of the female urethra: a direct histologic comparison., *Obstetrics and Gynecology*, *88*(5), 750–6, doi:10.1016/0029-7844(96)00323-7.

Svabík, K., K. L. Shek, and H. P. Dietz (2009), How much does the levator hiatus have to stretch during childbirth?, *BJOG : an International Journal of Obstetrics And Gynaecology*, *116*(12), 1657–62, doi:10.1111/j.1471-0528.2009.02321.x.

Tinelli, A., A. Malvasi, S. Rahimi, R. Negro, D. Vergara, R. Martignago, M. Pellegrino, and C. Cavallotti (2009), Age-related pelvic floor modifications and prolapse risk factors in postmenopausal women., *Menopause (New York, N.Y.)*, doi:10.1097/gme.0b013e3181b0c2ae.

Tschoegl, N. (1989), *The phenomenological theory of linear viscoelastic behavior*, Springer-Verlag, New York.

Tunn, R., J. O. DeLancey, D. Howard, J. M. Thorp, J. A. Ashton-Miller, and L. E. Quint (1999), Mr imaging of levator ani muscle recovery following vaginal delivery., *International Urogynecology Journal And Pelvic Floor Dysfunction*, *10*(5), 300–7.

Vacca, A. (2006), Vacuum-assisted delivery: An analysis of traction force and maternal and neonatal outcomes, *Australian & New Zealand Journal Of Obstetrics & Gynaecology*, *46*(2), 124–127, doi: 10.1111/j.1479-828X.2006.00540.x.

Vacca, A., A. Grant, G. Wyatt, and I. Chalmers (1983), Portsmouth operative delivery trial: a comparison vacuum extraction and forceps delivery., *British journal of Obstetrics and Gynaecology*, *90*(12), 1107–12.

Vasilenko, P., and J. P. Mead (1987), Growth-promoting effects of relaxin and related compositional changes in the uterus, cervix, and vagina of the rat., *Endocrinology*, *120*(4), 1370–6.

Watanabe, T. (1988), A basic study on cervical ripening–with special reference to the stretch modulus in the rat uterine cervix, *Nippon Sanka Fujinka Gakkai Zasshi*, *40*(1), 1–8.

Weiss, J., B. Maker, and S. Govindjee (1996), Finite element implementation of incompressible, transversely isotropic hyperelasticity, *Computer Methods In Applied Mechanics And Engineering*, *135*(1-2), 107–128.

Weiss, J. A. (1994), A constitutive model and finite element representation for transversely isotropic soft tissues, Ph.D. thesis, The University of Utah.

Weiss, J. A., and J. C. Gardiner (2001), Computational modeling of ligament mechanics., *Critical Reviews in Biomedical Engineering*, *29*(3), 303–71.

Wen, S. W., S. Liu, K. M. S., S. Marcoux, A. Ohlsson, R. Sauve, and R. Liston (2001), Comparison of maternal and infant outcomes between vacuum extraction and forceps deliveries, *American Journal of Epidemiology*, *153*(2), 103–125.

Xia, T., and L. Law (2008), A theoretical approach for modeling peripheral muscle fatigue and recovery, *Journal Of Biomechanics*, *41*(14), 3046–3052, doi:10.1016/j.jbiomech.2008.07.013.